

Asymmetric and Non-monotonic Response of the Climate System to Idealized CO₂ Forcing

Ivan Mitevski

Submitted in partial fulfillment of the
requirements for the degree of
Doctor of Philosophy
under the Executive Committee
of the Graduate School of Arts and Sciences

COLUMBIA UNIVERSITY

2023

© 2023

Ivan Mitevski

All Rights Reserved

Abstract

Asymmetric and Non-monotonic Response of the Climate System to Idealized CO₂ Forcing

Ivan Mitevski

In this thesis, I explore the climate system's response to symmetric abrupt and transient CO₂ forcing across a range of concentrations, from $1/8 \times$ to $8 \times$ CO₂, relative to pre-industrial levels. I use two CMIP6 class models: the CESM Large Ensemble (CESM-LE) model configuration and the NASA Goddard Institute for Space Studies Model E2.1-G (GISS-E2.1-G). I use a hierarchy of (1) fully coupled atmosphere-ocean-sea-ice-land, (2) slab ocean, and (3) prescribed sea surface temperature simulations to analyze and support the findings.

First, I find an asymmetric response in global mean surface air temperature (ΔT_s) and effective climate sensitivity (EffCS) between colder and warmer experiments. The ΔT_s response at $8 \times$ CO₂ is more than a third larger than the corresponding cooling at $1/8 \times$ CO₂. I attribute this asymmetry primarily due to the non-logarithmic CO₂ forcing, not to changes in the radiative feedbacks.

Second, I identify a non-monotonic response of EffCS in the warmer scenarios, with a minimum occurring at $4 \times$ CO₂ ($3 \times$ CO₂) in CESM-LE (GISS-E2.1-G). This minimum in the warming simulations is associated with a non-monotonicity in the radiative feedback. Similar non-monotonic responses in Northern Hemisphere sea-ice, precipitation, the latitude of zero precipitation-minus-evaporation, and the strength of the Hadley cell are also identified. Comparing the climate response over the same CO₂ range between fully coupled and slab-

ocean versions of the same models, I demonstrate that the climate system's non-monotonic response is linked to changes in ocean dynamics, associated with a collapse of the Atlantic Meridional Overturning Circulation (AMOC).

Third, to establish the significance of North Atlantic cooling in driving the non-monotonic changes in the radiative feedback, I conducted additional atmosphere-only (AMIP) simulations using the same models but with prescribed sea surface temperatures (SSTs) restricted to different regions. Through these simulations, I uncovered that the minimum EffCS value, characterized by notably negative radiative feedbacks, primarily originates from relative cooling of the sea surface temperature (SST) in the tropical and subtropical North Atlantic. This cooling of SSTs contributes to an increase in low-level cloud content in the eastern region of the North Atlantic, subsequently leading to a pronounced negative (stabilizing) feedback response.

Furthermore, I investigated the state dependence of the effective radiative forcing (ERF) from $^{1/16}\times$ to $16\times\text{CO}_2$. I found that ERF increases with CO_2 concentration due to the increase in Instantaneous Radiative Forcing (IRF). Specifically, the IRF increases at higher CO_2 values primarily due to stronger stratospheric cooling induced by CO_2 forcing. On the other hand, the radiative adjustments counteract the IRF increase, causing the ERF to rise at a slower pace compared to the corresponding increase in IRF induced by higher CO_2 concentrations.

Lastly, I studied the winter storm tracks in the Southern Hemisphere, focusing on experiments up to $8\times\text{CO}_2$. Through this analysis, I identified a non-linear response in the low latitude storm tracks. It is projected that the storm tracks will experience an intensification by the end of the century. However, my findings reveal that this intensification does not scale linearly with CO_2 forcing. In fact, the storm tracks shift poleward, including a reduction of the storm tracks at low-mid latitudes and intensification at mid-high latitudes.

Table of Contents

Acknowledgments	xii
Chapter 1: Introduction and Background	1
Chapter 2: Asymmetric Warming/Cooling Response to CO ₂ Increase/Decrease Mainly Due to Non-Logarithmic Forcing, not Feedbacks	9
2.1 Introduction	9
2.2 Methods	12
2.2.1 Models Used	12
2.2.2 Abrupt $n \times$ CO ₂ Experiments	12
2.2.3 Transient Experiments	13
2.2.4 Climate Sensitivity & Feedbacks	13
2.3 Results	15
2.3.1 Abrupt CO ₂ Experiments	15
2.3.2 Transient CO ₂ runs	18
2.4 Summary and Discussion	19
Chapter 3: Non-monotonic Response of the Climate System to Abrupt CO ₂ Forcing .	25
3.1 Introduction	25
3.2 Methods	27

3.3 Results	29
3.4 Summary and Discussion	39
 Chapter 4: Non-monotonic feedback dependence under abrupt CO ₂ forcing due to a North Atlantic pattern effect	41
4.1 Introduction	41
4.2 Materials and Methods	43
4.2.1 Models and Experiments	43
4.2.2 Analysis	44
4.3 Results	45
4.3.1 Non-monotonic effective climate sensitivity and radiative feedbacks .	45
4.3.2 Non-monotonic λ traced to changes in surface warming patterns .	46
4.3.3 A local pattern effect from the North Atlantic	48
4.4 Discussion and Conclusion	51
 Chapter 5: State dependence of CO ₂ Effective Radiative Forcing from $^{1/16}\times$ to $16\times$ CO ₂	59
5.1 Introduction	60
5.2 Methods	62
5.3 Results	64
5.4 Discussion and Conclusion	71
 Chapter 6: Southern Hemisphere Winter Storm Tracks Respond Differently to Low and High CO ₂ Forcings	75
6.1 Introduction	76
6.2 Methods	78

6.2.1	Models	78
6.2.2	Experiments	79
6.2.3	EKE Calculation	80
6.2.4	Spectral EKE budget	80
6.3	Results	81
6.3.1	The non-linear behavior of the Southern Hemisphere EKE	81
6.3.2	EKE_k Budget	85
6.4	Discussion and Conclusion	96
	Chapter 7: Conclusion	99
	Appendix A: “Asymmetric Warming/Cooling Response to CO ₂ Increase/Decrease Mainly Due to Non-Logarithmic Forcing, not Feedbacks”	103
	Appendix B: “Non-monotonic Response of the Climate System to Abrupt CO ₂ Forc- ing”	108
	Appendix C: “Non-monotonic feedback dependence under abrupt CO ₂ forcing due to a North Atlantic pattern effect”	114
	Appendix D: “Southern Hemisphere Winter Storm Tracks Respond Differently to Low and High CO ₂ Forcings”	122
	References	128

List of Figures

1.1	CO ₂ concentration compared to pre-industrial (PI) value in various socioeconomic pathways. Data was taken from Meinshausen et al. 2020.	4
2.1	Timeseries of surface temperature response ($ \Delta T_s $) for abrupt CO ₂ runs with CESM-LE model. a) $2\times\text{CO}_2$ and $1/2\times\text{CO}_2$, b) $4\times\text{CO}_2$ and $1/4\times\text{CO}_2$, c) $8\times\text{CO}_2$ and $1/8\times\text{CO}_2$ runs, and d) surface temperature asymmetry ($\Delta_a T_s$) between “warm” and “cold” cases.	21
2.2	Percent change (from $2\times\text{CO}_2$) for abrupt CO ₂ runs with CESM-LE model of: a) climate sensitivity as x-intercept of Gregory Regression (black, S_G), as a function of ERF (blue, S_F), and as a function of $1/\lambda$ (red, S_λ); b) effective radiative forcing (dark blue, ERF), instantaneous radiative forcing (IRF) fit from Byrne and Goldblatt 2014 (light blue), and stratospherically adjusted radiative forcing (RF) fit from Etminan et al. 2016 (cyan). c) Percent change of S_G vs. $1/\lambda$ (red) and d) S_G vs. ERF (black). r is the Pearson correlation coefficient.	22
2.3	Feedbacks for abrupt CO ₂ runs with CESM-LE model are shown as a difference from to $2\times\text{CO}_2$. a) Total feedback calculated with Gregory Regression years 1-150 (black), Pendergrass et al. 2018 kernels for CESM1-CAM5 (blue solid), and Huang et al. 2017 kernels (blue dashed). b) Individual feedbacks calculated with Pendergrass et al. 2018 kernels.	23
2.4	Transient runs annual timeseries with CESM-LE of a) the absolute value of surface temperature response ($ \Delta T_s $), b) effective radiative forcing ($ ERF $), c) net feedback (λ_{tr}), and d) correlation between asymmetries in $\Delta_a T_s$ and $\Delta_a ERF$. Responses from abrupt simulations are shown as dots.	24

3.1	Annual surface temperature response (ΔT_s) as a function of radiative forcing in a,b) fully coupled model (FOM) runs for the global mean (green), NH (red), and SH (blue), and c,d) for the NH with (red) and without the North Atlantic Warming Hole (NAWH, black) and slab-ocean (SOM) runs (purple). Panels a,c) show GISS-E2.1-G data and panels b,d) show CESM-LE data.	32
3.2	Annual mean surface temperature response (ΔT_s) to a,b) $2\times\text{CO}_2$, c,d) $3\times\text{CO}_2$, e,f) $4\times\text{CO}_2$, g,h) $5\times\text{CO}_2$, and i,j) $8\times\text{CO}_2$ shown for both GISS-E2.1-G (left) and CESM-LE (right) model runs. Note: higher warming than 12K is shown with same color as 12K.	34
3.3	Annual Arctic sea-ice response to a,b) $2\times\text{CO}_2$, c,d) $3\times\text{CO}_2$, e,f) $4\times\text{CO}_2$, g,h) $5\times\text{CO}_2$, and i,j) $8\times\text{CO}_2$ shown for both GISS-E2.1-G (left) and CESM-LE (right) model runs.	36
3.4	Annual mean a,b) sea-ice extent (10^6 km^2) defined as grid cell areas with more than 15% ice concentration, c,d) precipitation (mm/day), e,f) dry zone edge (ϕ_{P-E}), and g,h) HC strength (Ψ_{500}) for SH (blue) and NH (red) as a function of radiative forcing. Error bars denote 95% confidence intervals calculated using Student's t -distribution.	37
4.1	a) Global mean surface air temperature response (ΔT_s), b) effective climate sensitivity (EffCS), c) effective radiative forcing (ERF) from 30-year fixed sea-surface temperature runs, and d) net feedback parameter (λ) from the 150-year Gregory regression of abrupt $n\times\text{CO}_2$ runs. The confidence intervals for ΔT_s and ERF represent one standard deviation of the annual global mean values of the last 50 and 20 years of the runs, respectively. The confidence interval for the EffCS and λ are 95% obtained by resampling the linear regressions 10,000 times.	55
4.2	a) Global net feedback parameter λ from coupled runs, AGCM prescribed-SST runs with SSTs from coupled runs, and prescribed-SST runs with $3\times\text{CO}_2$ pattern, where the $3\times\text{CO}_2$ SST patterns are scaled with the actual global-mean SST values of $4\times\text{CO}_2$ and $5\times\text{CO}_2$, respectively. Spatial patterns of the local contribution to the global λ at $4\times\text{CO}_2$ from b) prescribed-SST, c) prescribed-SST with $3\times\text{CO}_2$ pattern and d) the difference.	56
4.3	Maps of SST patterns (calculated as the regression of local temperature changes to global temperature changes for 150 years) in the coupled runs for a) $3\times\text{CO}_2$, b) $4\times\text{CO}_2$, and c) $5\times\text{CO}_2$. The differences between $4\times$ and $3\times\text{CO}_2$, and $5\times$ and $4\times\text{CO}_2$, are shown in d) and e), respectively. Figures f-j) show λ maps for the same CO ₂ experiments.	57

4.4	Maps of individual feedbacks calculated from prescribed-SST runs for: a-c net, d-f) Planck, g-i) lapse rate + water vapor, j-i) net cloud.	58
5.1	a) The radiative imbalance at the top of the atmosphere in the 10-year step experiments, where CO ₂ is doubled (red) or halved (blue) starting from the pre-industrial (PI) condition. b) The Effective Radiative Forcing (ERF), calculated as the difference between two levels shown in panel a and adjusted for land warming (see methods). c) The radiative imbalance at the top of the atmosphere in the $n \times$ CO ₂ prescribed-SST runs, starting from the PI CO ₂ concentration. d) Normalized ERF (divided by log ₂ n) obtained from the abrupt- $n \times$ CO ₂ run with CESM1-LE (left), 1pctCO ₂ runs with CESM1-LE (middle), and abrupt- $n \times$ CO ₂ runs with the GISS-E2.1-G model, with adjustments made for land warming (see methods in (Mitevski et al. 2022)).	65
5.2	a) ERF decomposition into longwave IRF calculated from SOCRATES, IRF calculated as a residual from the adjustments, total adjustments (Adj.), and stratospheric adjustments (A_st). The global mean temperature response profile from the runs in a). All values for the CO ₂ decrease runs are multiplied by -1 for better comparison with the CO ₂ increase values.	66
5.3	Zonal temperature response and asymmetry between 1/2 and 2×CO ₂ (a,b,c), 1/4 and 4×CO ₂ (d,e,f), 1/8 and 8×CO ₂ (g,h,i), and 1/16 and 16×CO ₂ (j,k,l).	68
5.4	Global mean temperature profiles of a) 10-year step and b) abrupt- $n \times$ CO ₂ experiments.	69
5.5	ERF decomposition into IRF, total (A_total), stratospheric (A_st), tropospheric (A_tr), stratospheric temperature (A_Ta_st), tropospheric temperature (A_Ta_tr), surface temperature (A_Ts), longwave tropospheric water vapor (A_Q_tr_lw), longwave stratospheric water vapor (A_Q_st_lw), shortwave tropospheric water vapor (A_Q_tr_sw), shortwave stratospheric water vapor (A_Q_st_sw), shortwave albedo (A_alb_sw), and net cloud (A_c_net) adjustment. The vertical lines show one standard deviation of the ten kernels, and the bars show the mean.	70
6.1	Vertically integrated zonal mean winter EKE response (relative to PI control run) in the Southern Hemisphere from CMIP models with extended SSP5-8.5 and RCP8.5 scenarios (see methods). The solid lines show the CMIP mean, and the shading shows one standard deviation across the models.	82

- 6.2 Vertically integrated zonal mean winter (JJA) Eddy Kinetic Energy (EKE) in the Southern Hemisphere for the (a,c) CESM-LE and (b,d) GISS-E2.1-G models. Panels (a) and (b) display the results from the abrupt-CO₂ runs, while panels (c) and (d) present the findings from the transient 1pctCO2 runs. 83
- 6.3 EKE_k as a function of zonal wavenumber in (a) CESM-LE and (b) GISS-E2.1-G models. The solid lines represent mid-high latitudes, while the dotted lines indicate low-mid latitudes. High and low latitudes are 30 degrees north and south, respectively, of the EKE maximum in the pre-industrial run (53°S for CESM-LE and 51°S for GISS-E2.1-G). The EKE changes are multiplied by the zonal wavenumber to preserve the logarithmic *x*-axis integral and are smoothed with a 3-point running mean for plotting purposes. 84
- 6.4 Components of the EKE_k budget from Equation 6.3: (a) and (b) depict the conversion of eddy available potential energy to EKE (PK), (c) and (d) illustrate the transfer of kinetic energy between the waves and the zonal mean flow (EM), (e) and (f) represent the energy transfer between different waves (EE), and (g) and (h) show the dissipation processes (F). The left column presents the data from the CESM-LE model, while the right column presents the data from the GISS-E2.1-G model. The response is multiplied by the zonal wavenumber to ensure the preservation of the integral on the logarithmic *x*-axis, and a 3-point running mean is applied for smoothing purposes. 86
- 6.5 (a-c) Correlation between PK and lower & upper baroclinicity from 2× to 8×CO₂ in the abrupt experiments. We approximate the baroclinicity with the Eady Growth Rate as $\sigma = \frac{dT/dy}{N}$. (d-e) Correlation between PK and the mechanisms governing σ : the meridional temperature gradient dT/dy and the inverse of static stability $1/N$. Panels (a) and (d) represent mid-high latitudes, and panels (b), (c), (e), and (f) the low-mid latitudes. The large scale waves (wavenumber 2) at low latitudes are shown in panels (b) and (e), and small scale waves (wavenumber 7) in panels (c) and (f). The upper tropospheric σ (black) is integrated from 250 to 500hPa, while the lower tropospheric σ from 500hPa to the surface. The correlation coefficient is the r-value. 89
- 6.6 Southern Hemisphere winter air temperature response in (a,b) the upper troposphere and (c,d) near surface for mid-high (black) and low-mid (gray) latitudes. The left column presents the data from the CESM-LE model, while the right column presents the data from the GISS-E2.1-G model. The upper troposphere is 250 to 500hPa, and the “near surface” is 500hPa to the surface. 92

6.7	Southern Hemisphere winter (JJA) air temperature response in (a,b) $2\times\text{CO}_2$, (c,d) $4\times\text{CO}_2$, and (e,f) $8\times\text{CO}_2$ for the last 50 years of the abrupt- CO_2 runs. The left column presents the data from the CESM-LE model, while the right column presents the data from the GISS-E2.1-G model.	93
6.8	Multi model mean Southern Hemisphere winter air temperature response in extended RCP8.5 and SSP5-8.5 scenarios up to (a) year 2000, (b) year 2100 with approximate $4\times\text{CO}_2$, (c) year 2200 with $7.4\times\text{CO}_2$, and (d) year 2300 with $7.6\times\text{CO}_2$	95
A.1	Gregory regression plots for a) CESM-LENS, and b) GISS-E2.1-G model. The solid lines show regression for years 1-150, and the dashed lines for years 1-20. The stars on the y -axis show the effective radiative forcing (ERF) calculated from the fixed SST and SIC runs.	103
A.2	Same as Figure 2.2 in the main text except using the GISS-E2.1-G model.	104
A.3	Same as Figure 2.2a and A.2a in the manuscript, except here we show S_F^* , which contains a correction to the surface temperature change in fixed SST and SIC runs as per Equation 1 in Hansen et al. 2005. Panel a) shows CESM-LE, and panel b) shows GISS-E2.1-G data.	105
A.4	Feedbacks with CESM-LE (left) and GISS-E2.1-G model (right). (a and b) total feedbacks calculated with Gregory Regression years 1-150 (black), Pendergrass 2018 kernels for CESM1-CAM5 (blue solid), and Huang 2017 kernels (blue dashed). (c and d) individual feedbacks for Pendergrass 2018 kernels. (e and f) individual feedbacks for Huang 2017 kernels.	106
A.5	Same as Figure 2.3 in main text except using the GISS-E2.1-G model.	107
B.1	Radiative forcing calculation comparison of the y -intercept from the Gregory regressions (black), the logarithmic approximation (green), and 30 year fixed SST experiments (red) for a) GISS-E2.1-G and b) CESM-LE.	109
B.2	Gregory regression plots for a,b) fully coupled (FOM) and c,d) slab-ocean (SOM) runs using annual averages for both GISS-E2.1-G (left) and CESM-LE (right). Intercepts are shown with larger black dots.	110
B.3	Time evolution of the Atlantic Meridional Overturning Circulation (AMOC) in a,b) abrupt CO_2 forcings in fully coupled (FOM) GISS-E2.1-G and CESM-LE; c,d) abrupt $4\times\text{CO}_2$ runs in CMIP5 and CMIP6 models. Time series are smoothed with a 5 year running mean.	111

B.4 As in Fig. 3.4 except shown here using output from the slab-ocean runs.	112
B.5 NH subtropics response to abrupt CO ₂ forcing. Edge of dry zones (ϕ_{P-E} , red) and specific humidity (q , light blue) for a) GISS-E2.1-G and b) CESM-LE fully coupled (FOM) models. q is averaged over 30°N to 45°N. Error bars denote 95% confidence intervals calculated using Student's <i>t</i> -distribution.	113
C.1 Same as Figure 4.1 in main text but for the GISS-E2.1-G model.	115
C.2 Same as Figure 4.2a in main text but with 95% confidence intervals. The confidence intervals are 95% obtained by resampling the linear regressions 10,000 times.	116
C.3 Same as Figure 4.2b-d in main text but for 5×CO ₂	117
C.4 Individual feedback difference between 4×CO ₂ and 3×CO ₂ for Global, Global - North Atlantic, and the North Atlantic region. The North Atlantic is defined as a box between 0 to 60N and 80W to 10E.	118
C.5 Maps of individual feedbacks calculated from prescribed-SST runs for: a-c) albedo, d-f) longwave cloud, and g-i) shortwave cloud.	119
C.6 Maps of a-c) low cloud content, d-f) estimated inversion strength (EIS), and potential temperature g-j) near 700 hPa and j-l) surface. The left panels (a,d,g,j) are 4×CO ₂ runs with prescribed-SSTs, middle panels (b,e,h,k) are 4×CO ₂ runs with 3×CO ₂ pattern, and the left panels (c,f,i,l) are the difference.	120
C.7 Maps of surface temperature patterns from two CMIP6 models composites with (a,b,c) and without (d,e,f) North Atlantic Warming Hole (NAWH), defined as cooling in the North Atlantic, and the difference (g,h,i). Composites are shown for SSP2-4.5 (a,d,g), SSP5-8.5 (b,e,h), and abrupt-4xCO ₂ scenario (c,f,i). The models without NAWH are ACCESS-CM2, AWI-CM-1-1-MR, CAMS-CSM1-0, CMCC-CM2-SR5, CanESM5, INM-CM4-8, IPSL-CM6A-LR, MIROC6, MPI-ESM1-2-HR, MPI-ESM1-2-LR. Models with NAWH are BCC-CSM2-MR, CESM2-WACCM, FGOALS-g3, GFDL-ESM4, IITM-ESM, KACE-1-0-G, MRI-ESM2-0, NorESM2-MM, TaiESM1. The surface temperature patterns are calculated as local surface temperature changes regressed to global surface temperature response for years 2015 to 2100 for the SSP scenarios and the first 150 years of the abrupt-4xCO ₂ runs, and then averaged across models.	121

D.1	Maps of wintertime EKE (10^6 Jm^{-2}) for the abrupt (a,b) $2\times\text{CO}_2$, (c,d) $4\times\text{CO}_2$, and (e,f) $8\times\text{CO}_2$ experiments. The left column presents the data from the CESM-LE model, while the right column presents the data from the GISS-E2.1-G model.	123
D.2	Eady Growth rate ($\sigma = \frac{dT/dy}{N}$) integrated from 250hPa to the surface for the (a) CESM-LE model and (b) the GISS-E2.1-G model shown for the range of $2\times$ to $8\times\text{CO}_2$ for Southern Hemisphere winter (JJA).	124
D.3	The growth rate of high (solid) and low (dotted) midlatitude waves based on the linear normal-mode instability analysis in the (a) CESM-LE and the (b) GISS-E2.1-G model shown for the range of $2\times$ to $8\times\text{CO}_2$ for Southern Hemisphere winter (JJA).	125
D.4	Correlation between Potential to Kinetic energy conversion (PK) and upper (black) and lower (gray) tropospheric baroclinicity, as measured by the Eady Growth Rate $\sigma = \frac{dT/dy}{N}$. dT/dy are the meridional temperature gradient, and N is the static stability. Panels (a) and (b) represent high latitudes, with large scale waves (wavenumber 2) at low latitudes shown in panels (c) and (d), and small scale waves (wavenumber 7) at low latitudes in panels (e) and (f). The left column presents the data from the CESM-LE model, while the right column presents the data from the GISS-E2.1-G model. The σ values are expressed as a percentage change from the $1\times\text{CO}_2$ values, while PK is presented as a difference from the $1\times\text{CO}_2$ values. The upper tropospheric σ (black) is integrated from 250 to 500hPa, while the lower tropospheric σ from 500hPa to the surface. The correlation coefficient (r-value) is provided.	126
D.5	Correlation between Potential to Kinetic energy conversion (PK) and upper (black) and lower (gray) meridional temperature gradient dT/dy and the inverse of static stability $1/N$. Panels (a) and (b) represent high latitudes, with large scale waves (wavenumber 2) at low latitudes shown in panels (c) and (d), and small scale waves (wavenumber 7) at low latitudes in panels (e) and (f). The left column presents the data from the CESM-LE model, while the right column presents the data from the GISS-E2.1-G model. The dT/dy and $1/N$ values are expressed as a percentage change from the $1\times\text{CO}_2$ values, while PK is presented as a difference from the $1\times\text{CO}_2$ values. The $1/N$ term is integrated from 250hPa to the surface. The correlation coefficient (r-value) is provided.	127

List of Tables

3.1 Total feedbacks λ [$\text{Wm}^{-2}\text{K}^{-1}$] (slope in Gregory regression plot), Effective Climate Sensitivity (ECS_{eff}) calculated as $-\text{ERF}_{\text{fsST},2x\text{CO}_2}/\lambda$ [K] with $\text{ERF}_{\text{fsST},2x\text{CO}_2}$ being 3.63 Wm^{-2} for GISS-E2.1-G and 3.88 Wm^{-2} for CESM-LE model, and global surface temperature response ΔT_s [K].	30
--	----

Acknowledgements

I would like to thank my advisors, Prof. Lorenzo Polvani and Dr. Clara Orbe, for their endless support and encouragement, for being a constant source of inspiration, and for allowing me to explore my research interests. Their unwavering belief in my abilities and their commitment to fostering an intellectually stimulating environment have played a crucial role in making my experience in graduate school truly enjoyable. Their guidance and mentorship have been instrumental in my growth as a researcher.

I would also like to thank Dr. Ron Miller, Prof. Michael Tippett, and Prof. Maria Rubenstein for agreeing to serve on my committee. Their expertise and insights have been invaluable in shaping the direction of my research, and they have always provided valuable feedback. I am truly grateful for their time and effort in reviewing and evaluating my work. Their constructive criticism and suggestions have significantly enhanced the quality and rigor of my thesis.

I am deeply indebted to my wife, parents, brother, and sister-in-law for their unwavering support and understanding throughout my academic endeavors. Their constant encouragement and belief in my abilities have strengthened and motivated me.

I also extend my sincere appreciation to my fellow Ph.D. students who shared the same office space as me. Their camaraderie and friendship made this journey intellectually stimulating and enjoyable. Their insights and discussions enriched my understanding and broadened my perspectives.

Furthermore, I would like to acknowledge my research group's current and former post-docs. Their mentorship, guidance, and unwavering support have been invaluable in shaping my research and personal growth. I am especially grateful to them for their assistance in refining my academic writing skills alongside my advisors. Their expertise and constructive feedback have played a crucial role in enhancing the quality of my work.

Chapter 1: Introduction and Background

To investigate how the climate system responds to changing greenhouse gas concentrations, particularly CO₂, we conduct experiments by altering the CO₂ concentrations from the pre-industrial state (year 1850). In order to increase the signal to noise ratio, we make experiments with higher changes in CO₂ concentrations to reduce the influence of internal variability. We frequently employ abrupt changes in CO₂ levels, such as 2× or 4×CO₂, to examine the response of the climate system.

Considering the transient nature of our present day climate, where CO₂ concentrations are increasing annually, and currently about 1.5× the pre-industrial levels, it is crucial to examine how the climate system evolves under realistic scenarios. Therefore, we use future emissions scenarios such as the Shared Socioeconomic Pathways (SSP), Representative Concentration Pathways (RCP), and a scenario where CO₂ concentration increases by 1% annually (1pctCO₂) until 4×CO₂ levels are reached. Although these transient experiments do not reach quasi-equilibrium, they provide valuable insights.

When studying the quasi-equilibrium response to lower CO₂ levels, such as 2×CO₂, many studies (e.g., Zelinka et al. 2020) rely on scaling down the response observed in 4×CO₂ experiments. This scaling assumes linearity in the response to CO₂ perturbations. In light of these considerations, the main objective of this thesis is to conduct a comprehensive analysis of the assumption of linearity in CO₂ perturbations. This analysis will cover a wide range of CO₂ perturbations, including increases up to 8×CO₂ and decreases to 1/8×CO₂.

The equilibrium climate sensitivity (ECS) is a fundamental parameter in climate science, representing the global mean surface air warming in the equilibrium state following a doubling of CO₂ concentrations from pre-industrial levels. Despite representing an equilibrated response of the system, ECS still explains most of the spread in the 21st century projec-

tions (Sherwood et al. 2020). Hence, ECS plays a key role in climate assessments, informing economic and policy evaluations of future global warming.

However, due to the inherent complexity of the climate system, ECS has been historically characterized by significant uncertainty, as seen in the wide range of estimates across Intergovernmental Panel on Climate Change (IPCC) reports, ranging from 1.9-5.2K in the first report to 1.5-4.5K in the fifth report (Knutti and Hegerl 2008; Knutti et al. 2017; Tian 2015). The latest estimates from the Coupled Model Intercomparison Project 6 (CMIP6) further expand this range from 1.8-5.6K (Zelinka et al. 2020). Recently, advancements have been made in constraining ECS through a comprehensive analysis that integrates multiple lines of evidence from historical and paleoclimate records using a Bayesian framework, as demonstrated in a World Climate Research Programme (WCRP) report (Sherwood et al. 2020). This analysis narrowed the ECS range to 2.6-3.9K, providing a tighter constraint. Building upon this progress, the sixth IPCC assessment report (Forster et al. 2021) estimated the ECS range to be within 2.5-4K. While significant strides have been made in reducing the uncertainty surrounding ECS, further refinement of the estimate remains challenging.

ECS can be determined through experiments with Earth System Models, where the system is perturbed with CO₂ forcing starting from a pre-industrial state. The Earth's energy balance in response to an abrupt CO₂ forcing can be described by the equation:

$$\Delta R = F + \lambda \Delta T \quad (1.1)$$

Here, ΔR represents the top-of-atmosphere (TOA) radiative imbalance caused by the change in CO₂ concentrations, F is the radiative forcing induced by this change, ΔT is the surface temperature response, and λ represents the total feedback parameter. In the case of ECS, when ΔR approaches zero, the corresponding ΔT represents the equilibrium temperature response and equals ECS. However, in practice, it is often challenging to reach complete equilibrium in model simulations, except when running the model for thousands of years

(Rugenstein et al. 2019), necessitating the use of linear regression techniques to approximate ECS through Effective Climate Sensitivity (EffCS). By performing a linear regression analysis (Gregory et al. 2004) of ΔR versus ΔT using annual mean values, the total radiative feedbacks (λ , slope) and the EffCS (represented by the x -intercept of the regression, where ΔR equals zero) can be calculated. The response of ΔR to changes in ΔT exhibits linearity with a slope of λ and the radiative forcing F as the y -intercept. Thus, the effective climate sensitivity can be approximated as $\text{EffCS} = -F/\lambda$.

An alternative approach to estimating ECS or EffCS involves using observational constraints based on reconstructions of past climates. We can make inferences about ECS by analyzing temperature and CO₂ concentrations derived from paleoclimate records. One particularly valuable period for studying EffCS is the Last Glacial Maximum (LGM), which occurred approximately twenty-one thousand years ago. During this period, the Earth experienced significantly colder conditions compared to the pre-industrial era (Tierney et al. 2020). The LGM is of great interest due to its quasi-equilibrium state, substantial climate forcings, and relatively well-constrained surface temperature reconstructions (Zhu and Poulsen 2021).

When using estimates derived from paleoclimate data, it is essential to consider how feedback mechanisms in past climate states may differ from those in the modern era. The state dependence of the feedbacks poses a challenge in constraining the EffCS using paleoclimate information. Hence, an important question arises regarding the symmetry of the climate system's response to warming (due to increasing CO₂) and cooling (due to decreasing CO₂) and the need to account for the CO₂ dependence when calculating feedbacks and radiative forcing. Addressing this question is the primary focus of Chapter 2.

EffCS is typically estimated using 150-year abrupt 4×CO₂ simulations in Earth System Models, assuming a constant value for each CO₂ doubling. This assumption is based on the logarithmic relationship between radiative forcing and CO₂ concentration, where the forcing at 2×CO₂ is double that at 4×CO₂. Another assumption is that the slope λ of the linear

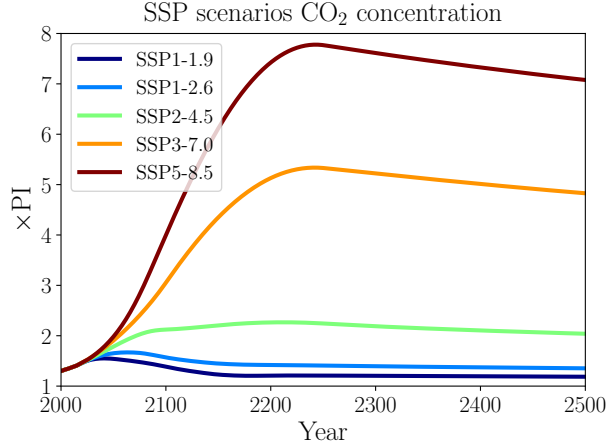


Figure 1.1: CO₂ concentration compared to pre-industrial (PI) value in various socioeconomic pathways. Data was taken from Meinshausen et al. 2020.

regression remains unchanged at higher CO₂ values. As a result, EffCS can be approximated at 2×CO₂ by dividing the EffCS estimated from 4×CO₂ by two, serving as an approximation for ECS.

However, previous modeling (Bloch-Johnson et al. 2021a; Mauritsen et al. 2019; Meraner et al. 2013; Sherwood et al. 2020; Zhu and Poulsen 2020) and paleoclimate studies (Anagnostou et al. 2020; Anagnostou et al. 2016; Farnsworth et al. 2019; Friedrich et al. 2016; Shaffer et al. 2016; Zhu et al. 2019) have shown that EffCS may not exhibit a constant behavior with successive CO₂ doublings. These studies have revealed an increasing trend in EffCS at higher CO₂ values, primarily driven by the nonlinear temperature dependence of the radiative feedbacks (λ), known as the state-dependence of feedbacks (Andrews et al. 2015; Bloch-Johnson et al. 2021a; Sherwood et al. 2015), with minor contributions from the nonlinear CO₂ dependence of radiative forcing (Byrne and Goldblatt 2014; Etminan et al. 2016). It is noteworthy that previous investigations of state dependence have focused on specific CO₂-doubling scenarios (2×, 4×, 8×CO₂) (Good et al. 2016; Rugenstein et al. 2019). The highest emission scenario (SSP5-8.5) outlined in the Shared Socioeconomic Pathways projects a transient increase in greenhouse gas forcing (see Fig. 1.1), reaching up to 8×CO₂ by 2250, encompassing intermediate CO₂ concentrations of 2×, 3×, 4×, 5×, 6×, 7×CO₂,

and $8 \times \text{CO}_2$ (Meinshausen et al. 2020). Hence, there is a need to investigate how EffCS and feedbacks respond to the increasing range of CO_2 concentrations, including the intermediate steps. Chapter 3 of this study is dedicated to addressing the question of whether EffCS and feedbacks remain constant as CO_2 concentrations increase.

In an abrupt- CO_2 forcing scenario, the relationship between ΔR and ΔT is not always linear in Earth System Models. In some cases, a linear approximation based on the term $\lambda \Delta T$ is insufficient. It becomes necessary to consider higher-order terms such as ΔT^2 or analyze different time intervals (time evolution of λ) within the simulation (Andrews et al. 2022; Andrews et al. 2015; Dong et al. 2019; Sherwood et al. 2020; Zhou et al. 2016). The time evolution of the feedback parameter λ has been linked to sea-surface temperature (SST) patterns, with a particular focus on their temporal changes (Andrews et al. 2022; Andrews et al. 2015; Dong et al. 2019; Sherwood et al. 2020; Zhou et al. 2016). For instance, estimates of EffCS derived from historical energy budget constraints tend to be lower than those obtained from long-term warming under CO_2 quadrupling, primarily due to differences in the cooling patterns observed in the Eastern tropical Pacific SSTs compared to model simulations (Andrews et al. 2022; Andrews et al. 2018; Bloch-Johnson et al. 2023; Dong et al. 2019; Gregory et al. 2020; Zhang et al. 2023; Zhou et al. 2016; Zhou et al. 2017). This discrepancy, known as the “pattern effect,” has been investigated using a Green’s function approach to identify the SST areas that have a more significant influence on the global feedback parameter λ (Dong et al. 2019; Zhang et al. 2023; Zhou et al. 2017). The analysis has revealed that tropical convective regions predominantly impact global feedback, while North Atlantic SSTs exhibit less sensitivity.

Moreover, the North Atlantic cooling pattern, known as the North Atlantic Warming Hole (NAWH), has been documented in historical records and model simulations (Chemke et al. 2020). This pattern is projected to persist under future greenhouse gas scenarios (Chemke et al. 2020; Gervais et al. 2018; Keil et al. 2020; Liu et al. 2020; Menary and Wood 2018; Ren and Liu 2021). Previous work (Lin et al. 2019) has indicated that the cooling

of sea-surface temperatures (SSTs) in the North Atlantic, relative to the tropical mean, associated with the formation of NAWH leads to a more negative feedback parameter (λ) and as a result lowers the estimate of equilibrium climate sensitivity (EffCS). Nevertheless, the specific contribution of this North Atlantic SST cooling pattern to the global feedback parameter λ has yet to be quantified.

Chapter 4 of this thesis evaluates the significance of the North Atlantic Warming Hole in determining the global feedback parameter λ . Unlike previous studies that primarily focused on examining the importance of the North Atlantic cooling pattern on the temporal evolution of λ at a single CO₂ concentration (Andrews et al. 2022; Andrews and Webb 2018; Dong et al. 2019; Lin et al. 2019; Zhou et al. 2016), this chapter expands the analysis to encompass multiple CO₂ levels. It also explores the changing significance of the pattern effect under increasing CO₂ concentrations.

Moreover, existing research has predominantly concentrated on the variations of EffCS and feedbacks in response to changes in global-mean temperatures under different CO₂ forcings (Bloch-Johnson et al. 2021a; Caballero and Huber 2013; Meraner et al. 2013), with limited consideration given to the response of spatial patterns of feedback and local surface warming to varying CO₂ forcings. Therefore, there exists a crucial need to investigate how the spatial distribution of feedbacks and the corresponding patterns of local surface warming respond to different CO₂ forcings, thus facilitating a more comprehensive understanding of the behavior of the climate system (Bloch-Johnson et al. 2021a; Caballero and Huber 2013; Meraner et al. 2013). Chapter 4 of this thesis also provides insights into this aspect.

Our current focus on studying the state dependence of EffCS has primarily revolved around the feedback component represented by λ . However, previous research (Colman and McAvaney 2009; Hansen et al. 2005) investigating EffCS across a broader range of CO₂ forcings has observed increased effective radiative forcing (ERF) with increasing CO₂ concentrations. Within the energy balance framework used to estimate EffCS, ERF is the most convenient definition of radiative forcing (Forster et al. 2016). The ERF associated

with CO₂ is typically divided into the instantaneous radiative forcing (IRF) attributable solely to CO₂ and the radiative adjustments resulting from rapid changes in atmospheric variables following the introduction of CO₂ (e.g., atmospheric temperature profile and water vapor before there is significant change in the ocean).

While much attention has been given to the state dependence of the IRF (He et al. 2022; Jeevanjee et al. 2021; Pincus et al. 2020), the state dependence of the adjustments has received less attention. Previous studies have primarily emphasized the IRF due to its better understanding and substantial contribution (accounting for approximately two-thirds) to the ERF. Additionally, the IRF is the primary driver of the adjustments. However, the ERF, which encompasses both the IRF and adjustments, is widely regarded as the most comprehensive measure of radiative forcing (Forster et al. 2016; Ramaswamy et al. 2018; Sherwood et al. 2015), given its significant impact on the surface climate (Hansen et al. 2005; Richardson et al. 2019). Therefore, this raises an important question regarding the contribution of the state dependence of ERF to the state dependence of EffCS and the underlying mechanisms driving this relationship. In Chapter 5, we address this question by examining both the IRF and adjustments and explain the mechanisms behind the state dependence of ERF.

Previous studies have explored the linearity of different aspects of the climate system, such as the hydrological cycle and the strength of the Hadley Cell, in idealized global circulation models (Levine and Schneider 2011; O’Gorman and Schneider 2008a; O’Gorman and Schneider 2008b). These studies have found a non-monotonic response of large-scale global mean precipitation with increasing surface temperature. Additionally, idealized studies have suggested that the strength of the Hadley Cell attains a maximum value under present-day climate conditions when compared to both warmer and colder climates (Levine and Schneider 2011; O’Gorman and Schneider 2008a). Comprehensive climate models have also demonstrated a monotonic widening of the tropical width in response to CO₂-induced warming (Chemke and Polvani 2019; Grise et al. 2019). Despite this, whether this widening

trend remains linear across a wide range of CO₂ forcings in fully coupled earth system models remains uncertain. Hence, in Chapter 3, I investigate the linearity of global precipitation, the Hadley Cell's strength, the tropics' width, and sea ice response to abrupt CO₂ experiments up to 8×CO₂.

Previous studies in idealized settings have also highlighted the non-monotonic behavior of storm tracks in response to global mean warming (O'Gorman and Schneider 2008a). Specifically, these investigations have shown that the Eddy Kinetic Energy (EKE) of the atmosphere, a measure used to characterize storm tracks, reaches a maximum at current surface temperatures and decreases under both warmer and colder surface temperature conditions. Given the possibility of non-monotonic variations in EKE in a substantially warmer climate and the projected high CO₂ levels in the future (Fig. 1.1), it is crucial to systematically examine the response of storm tracks at intermediate CO₂ forcing levels using more realistic Earth system model simulations. This undertaking holds significant importance as understanding and predicting the response of storm tracks in future warming scenarios beyond the 21st century is essential for the development of effective adaptation and mitigation strategies, particularly in the case of a non-monotonic response, as suggested by idealized studies. Hence, Chapter 6 of this thesis explores storm tracks.

Chapter 2: Asymmetric Warming/Cooling Response to CO₂

Increase/Decrease Mainly Due to Non-Logarithmic Forcing, not Feedbacks

Note: This chapter has been published in very near its present form as “Asymmetric Warming/Cooling Response to CO₂ Increase/Decrease Mainly Due to Non-Logarithmic Forcing, not Feedbacks” in Mitevski et al. [2022](#).

Abstract

We explore the CO₂ dependence of effective climate sensitivity (S_G) with symmetric abrupt and transient CO₂ forcing, spanning the range $1/8\times$, $1/4\times$, $1/2\times$, $2\times$, $4\times$, and $8\times\text{CO}_2$, using two state-of-the-art fully coupled atmosphere-ocean-sea-ice-land models. In both models, under abrupt CO₂ forcing, we find an asymmetric response in surface temperature and S_G . The surface global warming at $8\times\text{CO}_2$ is more than one third larger than the corresponding cooling at $1/8\times\text{CO}_2$, and S_G is CO₂ dependent, increasing non-monotonically from $1/8\times\text{CO}_2$ to $8\times\text{CO}_2$. We find similar CO₂ dependence in the transient runs, forced with $-1\%\text{yr}^{-1}\text{CO}_2$ and $+1\%\text{yr}^{-1}\text{CO}_2$ up to $1/8\times\text{CO}_2$ and $8\times\text{CO}_2$, respectively. The non-logarithmic effective radiative forcing – not the changing feedbacks – primarily explains the dependence of S_G on CO₂, particularly at low CO₂ levels. The changing feedbacks, however, explain S_G ’s non-monotonic behavior.

2.1 Introduction

Equilibrium climate sensitivity (ECS) is the global mean surface temperature change after the doubling of CO₂ concentrations from pre-industrial (PI) levels and restoration of

equilibrium. ECS is perhaps the most important metric in climate science, and it has been extensively investigated in the literature (Sherwood et al. 2020). An important question is whether the amount of warming for each CO₂ doubling (which we refer to as the effective climate sensitivity, S_G) is constant or not (i.e., whether it is CO₂ dependent). Sufficient conditions for a constant S_G are 1) that the radiative forcing of the climate system for each CO₂ doubling is constant and 2) that the net radiative feedback does not change with CO₂ levels. This question has been investigated in many modeling studies (Bloch-Johnson et al. 2021b; Mauritzen et al. 2019; Meraner et al. 2013; Sherwood et al. 2020), which have reported that S_G is indeed CO₂ dependent. Most of these studies find that S_G increases at higher CO₂ levels and that the change in feedbacks, not the change in CO₂ radiative forcing, is the primary driver of S_G CO₂ dependence.

An alternative approach to using climate models to investigate the dependency of S_G on CO₂ is to seek observational constraints from reconstructions of past climates. In particular, most studies conclude that S_G inferred from paleoclimate records does depend on CO₂ (Anagnostou et al. 2020; Anagnostou et al. 2016; Caballero and Huber 2013; Farnsworth et al. 2019; Friedrich et al. 2016; Shaffer et al. 2016; Zhu et al. 2019), although a few studies disagree (e.g., Martínez-Botí et al. 2015a). An ideal period to study the S_G from past climate is the Last Glacial Maximum (LGM), approximately 21 kyr ago, when the Earth was roughly 6K colder than PI conditions (Tierney et al. 2020). The LGM period is of particular interest because the climate system was in a quasi-equilibrium state, the climate forcings were large, and the surface temperature reconstructions are relatively well-constrained (Zhu and Poulsen 2021). However, when considering the LGM and other periods in Earth's past, one needs to account for how the feedbacks in those past climate states differ from the feedbacks operating in the modern state: hence the challenge in using paleoclimate-based estimates to constrain S_G .

While modeling and paleoclimatic evidence suggest that S_G depends on CO₂, a systematic exploration of the symmetry over a wide range of CO₂ forcing has yet to be performed. The

question thus remains: is the climate system response symmetric across a broad range of positive (warm) and negative (cold) CO₂ forcings? The question of symmetry was examined recently by Chalmers et al. 2022, who compared $1/2\times$ and $2\times$ CO₂ simulations performed with the CESM1-CAM5 model, and found that global surface temperatures warm 20% more than they cool. Roughly 50% of this asymmetry was shown to derive from an asymmetry in CO₂ radiative forcing; the rest was associated with differences in feedbacks which, interestingly, were found not to be related to clouds. Whether this result holds over a broader range of CO₂ forcing, and whether it is model dependent remains an open question.

We here address these questions using a much broader range of both abrupt and transient CO₂ forcings, and do so with two different climate models. Specifically, CO₂ is varied from $1/8\times$ to $8\times$ PI values, to test the CO₂ symmetry of the climate system response to comparable increased and decreased CO₂. While we are not the first ones to perform such symmetric CO₂ runs (Chalmers et al. 2022; Colman and McAvaney 2009; Hansen et al. 2005; Russell et al. 2013), here we explore 1) a larger CO₂ range than previously considered, 2) we do so using two different fully coupled climate models and, most importantly, 3) we perform the experiments with both abrupt and transient CO₂ runs.

Overall we confirm the asymmetric response in surface temperature: the climate system warms *more* with consecutive CO₂ doublings ($2\times$, $4\times$, and $8\times$ CO₂) than it cools with consecutive CO₂ halvings ($1/2\times$, $1/4\times$, and $1/8\times$ CO₂). This asymmetry is also reflected in S_G , which *increases* at higher CO₂ concentrations, consistent with previous studies. Surprisingly, we find that the non-logarithmic dependence of CO₂ radiative forcing (i.e., the fact that CO₂ radiative forcing increases more rapidly than the log of the CO₂ concentration) is primarily responsible for this asymmetric response, and not the changes in radiative feedbacks.

2.2 Methods

2.2.1 Models Used

We use two fully coupled atmosphere-ocean-sea-ice-land models: the large ensemble version of the Community Earth System Model (CESM-LE) and the NASA Goddard Institute for Space Studies Model E2.1-G (GISS-E2.1-G). CESM-LE comprises the Community Atmosphere Model version 5 (CAM5, 30 vertical levels), and parallel ocean program version 2 (POP2, 60 vertical levels) with approximately 1° horizontal resolution in all model components (Kay et al. 2015). GISS-E2.1-G is a 40-level atmospheric model with a resolution of $2^\circ \times 2.5^\circ$ latitude/longitude, coupled to a 1° horizontal resolution 40-level GISS Ocean v1 (GO1) (Kelley et al. 2020). This configuration of the GISS model contributed to the CMIP6 project under the label “GISS-E2-1-G”. We show CESM-LE results in the main text, and some GISS-E2.1-G results in Appendix A to corroborate CESM-LE findings.

2.2.2 Abrupt $n \times \text{CO}_2$ Experiments

We perform a series of abrupt CO_2 forcing runs using both models, subject to $^{1/8}\times$, $^{1/4}\times$, $^{1/2}\times$, $2\times$, $4\times$, and $8\times\text{CO}_2$ forcings, with all other trace gases, ozone concentrations, aerosols, and other forcings fixed at PI values. Following CMIP6 protocol for $4\times\text{CO}_2$ runs, we integrate all runs to 150 years starting from PI conditions. We contrast these to a PI control run to calculate the response.

For each model, we estimate the effective radiative forcing (ERF) with a companion series of CO_2 experiments, as per Forster et al. 2016, with prescribed PI sea surface temperatures (SSTs) and sea-ice concentrations (SICs). These experiments are 30-year-long. We calculate ERF as the difference between the global mean net top of the atmosphere (TOA) flux between PI and $n \times \text{CO}_2$ in these prescribed SSTs and SICs experiments. We do not here adjust for land warming simply because, in our ERF calculations, the surface temperature response in the fixed SSTs and SICs simulations is minimal (Smith et al. 2020b), but we have verified

that the adjustment does not change our results (see Figure A.3).

2.2.3 Transient Experiments

In addition to the abrupt CO₂ runs, we also perform transient CO₂ runs with the CESM-LE model. We start from PI conditions (same as in the abrupt CO₂ forcing), and we increase CO₂ at +1%yr⁻¹ for the “warm” case for 215 years (slightly above 8×CO₂) and -1%yr⁻¹ for the “cold” case for 215 years (slightly below 1/8×CO₂). We estimate transient effective radiative forcing as in the abrupt experiments, by running companion simulations with specified SSTs and SICs set to PI values (Forster et al. 2016), while ramping up CO₂ at rates of +1%yr⁻¹ and -1%yr⁻¹. We contrast all variables to PI values to compute the response.

2.2.4 Climate Sensitivity & Feedbacks

We define effective climate sensitivity S_G as the x-intercept of the Gregory regression (Gregory et al. 2004) for each abrupt $n \times \text{CO}_2$ run using the following equation:

$$S_G = \left| \frac{F_{y-\text{int}}(n \times \text{CO}_2)}{\lambda(n \times \text{CO}_2) \cdot \log_2 n} \right| \quad (2.1)$$

We find the radiative forcing $F_{y-\text{int}}$ as the y-intercept and the net feedback parameter λ as the slope from the Gregory regression (see Figure A.1) where we regress the net TOA radiative imbalance against the global mean surface temperature response for years 1-150. In order to compare S_G for different CO₂ doubling / halving, we divide by $\log_2 n$ (assuming a logarithmic CO₂ forcing) and take the absolute value in Equation 2.1. Note that our definition of the effective climate sensitivity S_G is a generalization of the more common definition of effective climate sensitivity (which is typically defined as per Equation 2.1 but with $n = 2$). To check for the possibility that λ and S_G may be strongly affected by the “pattern effect”, we have repeated the calculations by regressing years 21-150 only, and our

main results were not changed.

To calculate the individual feedbacks λ_i , we use radiative kernels (K_x) from both Pendergrass et al. 2018 and Huang et al. 2017 to quantify the sensitivity of TOA radiation imbalance (ΔR) to changes in surface and atmospheric temperature (T), water vapor (q), and surface albedo (α) (Shell et al. 2008; Soden et al. 2008). For each year of the 150-year experiment, we multiply the spatially-resolved kernels by the climate field anomalies ($R_x = K_x \cdot \Delta x$, where x is T, q, α), and then vertically integrate (for atmospheric temperature and water vapor) up to the tropopause. We define the tropopause as 100 hPa at the equator, 300 hPa at the poles, and in between, it varies by the cosine of the latitude (Soden and Held 2006). Lastly, we regress these quantities on the surface temperature response to find the radiative feedbacks as the regression slope. The cloud feedbacks are computed via the residual method (Soden and Held 2006) as follows. First, we subtract effective radiative forcing and the temperature, water vapor, and surface albedo radiative fluxes from the TOA net radiative flux, resulting in $\Delta R_{\text{cloud}} = \Delta R - \text{ERF} - \sum \Delta R_x$. Then, we regress ΔR_{cloud} onto ΔT_s anomalies and define the corresponding slope as the cloud feedback. Lastly, we find shortwave (SW) and longwave (LW) components of the cloud feedback by considering the radiative changes in LW and SW components separately.

In the transient runs, we estimate the net feedback parameter λ_{tr} following Rugenstein and Armour 2021 (see λ_{eff1pct} in their Figure 1d) with the expression:

$$\lambda_{\text{tr}} = -\frac{\text{ERF}(t) - \Delta R(t)}{\Delta T_s(t)} \quad (2.2)$$

$\Delta R(t)$ is the net TOA radiative imbalance, and $\Delta T_s(t)$ is the global mean surface temperature response in the transient runs at year t . $\Delta R(t)$ and $\Delta T_s(t)$ are 30-year moving averages of the respective terms. Note that we use different definitions for the feedback parameter in the abrupt and transient simulations.

2.3 Results

2.3.1 Abrupt CO₂ Experiments

We start by examining the global mean surface temperature response ($|\Delta T_s|$) timeseries for the abrupt CO₂ runs (Figure 2.1). We contrast – in panels a, b, and c – the timeseries of each corresponding “warm” ($2\times$, $4\times$, and $8\times$ CO₂) and “cold” simulation ($1/2\times$, $1/4\times$, and $1/8\times$ CO₂) by taking the absolute value of the response from PI: note that the $|\Delta T_s|$ in the “warm” case is always stronger than the “cold” case. In particular, we find 20% more warming at $2\times$ than cooling at $1/2\times$ CO₂ (Figure 2.1a), 15% more at $4\times$ than $1/4\times$ CO₂ (Figure 2.1b), and 41% more at $8\times$ than $1/8\times$ CO₂ (Figure 2.1c). The asymmetry in $|\Delta T_s|$ is amplified at higher CO₂ forcing, and largest in the $1/8\times$ CO₂ vs. $8\times$ CO₂ case (Figure 2.1c). The asymmetry is reduced at $4\times$ CO₂ vs. $1/4\times$ CO₂ due to changes in ocean heat transport which result in a formation of the North Atlantic Warming Hole in this model at $4\times$ CO₂ (see more details in Mitevski et al. 2021).

To quantify the timescale of the asymmetry in $|\Delta T_s|$ between “warm” and “cold” cases, we define the asymmetry between “warm” and “cold” cases as

$$\Delta_a X = |\Delta X(\text{warm})| - |\Delta X(\text{cold})| \quad (2.3)$$

where X is any climate variable (e.g., T_s), and subscript a refers to “asymmetry” (Figure 2.1d). In particular, we find that the asymmetry emerges rapidly in the first ten years (e.g., 90% at $8\times$ CO₂). Relative to the (slower) response associated with SST-driven feedbacks, the asymmetry appears quickly, suggesting that it might be due to radiative changes.

Next, we calculate effective climate sensitivity S_G from the Gregory regression (Equation 2.1), and plot it as percentage change from $2\times$ CO₂ (black line, Figure 2.2a). S_G is CO₂ dependent and increases with CO₂ concentration: at $1/8\times$ CO₂, it is more than 20% *lower* than $2\times$ CO₂ values, and at $8\times$ CO₂, it is around 5% *higher* than at $2\times$ CO₂. CO₂ dependent

S_G is possible if either the effective radiative forcing (ERF) or the net feedback parameter (λ) change with CO_2 . To individually test the relative importance of ERF and λ , we calculate the climate sensitivity in two different ways.

First, to examine the dependence of climate sensitivity on ERF, we calculate climate sensitivity as S_F using the expression:

$$S_F = \left| \frac{\text{ERF}(n \times \text{CO}_2)}{\lambda(2 \times \text{CO}_2) \cdot \log_2 n} \right| \quad (2.4)$$

where ERF is derived from the $n \times \text{CO}_2$ fixed SSTs and SICs runs, and λ (slope from Gregory Regression) is held constant at the $2 \times \text{CO}_2$ value. As seen in Figure 2.2a, we find that S_F (blue line) changes in tandem with S_G (black line), which reinforces the fact that changes in ERF explain the changes in S_G .

Second, to assess whether changes in feedback strength also contribute to S_G , we calculate climate sensitivity as S_λ :

$$S_\lambda = \left| \frac{\text{ERF}(2 \times \text{CO}_2)}{\lambda(n \times \text{CO}_2)} \right| \quad (2.5)$$

where λ is calculated at each $n \times \text{CO}_2$ and ERF is held constant at $2 \times \text{CO}_2$ value. As seen in Figure 2.2a, S_λ (red) changes in the opposite direction than S_G (black) for CO_2 values lower than $2 \times \text{CO}_2$. This suggests that changes in λ are not the main driver of the S_G dependence on CO_2 . However, it is important to note that for CO_2 values higher than $2 \times \text{CO}_2$, we find λ non-monotonically increasing to $8 \times \text{CO}_2$, which can be linked to the corresponding non-monotonic behavior of S_G . We find qualitatively similar results using the GISS-E2.1-G model (Figure A.2a), confirming that ERF is the primary driver of the dependence of S_G on CO_2 .

Next, we correlate S_G with $1/\lambda$ (Figure 2.2c) and ERF (Figure 2.2d) across all abrupt CO_2 experiments from $1/8 \times$ to $8 \times \text{CO}_2$ to examine whether feedbacks or forcing better correlate with changes in S_G . Overall, we find little correlation between S_G and $1/\lambda$ ($r=-0.44$) and a very strong correlation between S_G and ERF ($r=0.91$). Similarly, a high correlation be-

tween S_G and ERF is found in the GISS-E2.1-G model (Figure A.2d). This strengthens our conclusions from Figure 2.2a that the changes in ERF are driving the S_G increase. However, if one considers warm cases, one sees a strong correlation between S_G and $1/\lambda$, as indicated earlier. This is in agreement with previous studies (Bloch-Johnson et al. 2021b; Meraner et al. 2013), which reported that feedback changes are important for the dependence of S_G on CO₂. However, over a broad range of CO₂ forcing, including colder climates, that is not the case: changes in ERF are more important than feedback changes.

Given the aforementioned importance of ERF in driving the changes in S_G , we next look in more detail at ERF, calculated from fixed SSTs and SICs runs, following Forster et al. 2016, from $1/8\times$ to $8\times$ CO₂ (dark blue bars, Figure 2.2b). If ERF were scaled simply with the logarithm of CO₂ concentration, then the dark blue bars would be identical for all CO₂ values. However, we see that ERF grows more than logarithmically with CO₂. We find a similar but weaker non-logarithmic behavior in the instantaneous radiative forcing (IRF) reported in Byrne and Goldblatt 2014, which we obtain by linearly interpolating their line-by-line radiative calculations (SI file “text03.txt” in Byrne and Goldblatt 2014) and plot with light blue bars in Figure 2.2b. We also compare our ERF calculations with the proposed stratospherically adjusted radiative forcing fit in Etminan et al. 2016 for the warming case only (since it is not valid for low CO₂ values), and it appears both are in agreement.

A limitation to our ERF calculation approach is that we only fix the SSTs and SICs in the simulation, but not the land temperatures. Fixing the land temperatures has been shown to increase ERF in warmer climates even more than when only SSTs and SICs are fixed (Andrews et al. 2021). To account for this, we removed the land and sea-ice warming effects in our ERF calculations, following Equation 1 in Hansen et al. 2005 as shown in Figure A.3, and found that the correction (dashed blue lines) leads, if anything, to a stronger non-logarithmic ERF. Hence, incorporating fixed land temperatures leads to ERF increasing even more rapidly than the log of CO₂ concentration; this strengthens our argument that the S_G dependence on CO₂ is due to non-logarithmic CO₂ radiative forcing.

Next, we perform a standard decomposition of λ into individual radiative feedbacks λ_i . The summation of individual feedbacks ($\sum \lambda_i$) is shown in Figure 2.3a (blue). $\sum \lambda_i$ follows closely the net feedback calculated from the Gregory regression (black). We perform the decomposition using two radiative kernels from Pendergrass et al. 2018 and Huang et al. 2017, and we find minimal sensitivity to the choice of kernel (Figure A.4). The individual feedbacks, plotted as differences from $2\times\text{CO}_2$ values, from the Pendergrass et al. 2018 kernels are shown in Figure 2.3b. We see a clear signal in the lapse rate feedback, which weakens the net feedback in the “cold” case and strengthens it in the “warm” case. The longwave cloud feedback has clear global surface temperature dependence, increasing with CO_2 monotonically for all CO_2 values. However, in general, we find no clear pattern in the changes in individual feedbacks that would sufficiently explain the overall feedbacks CO_2 dependence. In addition, the changes in feedbacks in the GISS-E2.1-G model (Figure A.5) are qualitatively different from those in the CESM-LE model (Figure 2.3). Since our models do not agree on the changes in individual feedbacks across the CO_2 range, and since we showed that feedback changes are strongly not correlated with changes in S_G (Figure 2.2c), we do not explore further the mechanisms driving feedback changes in the individual models.

2.3.2 Transient CO_2 runs

The abrupt CO_2 forcing runs show that the effective climate sensitivity increases with CO_2 , and that the non-logarithmic nature of the ERF is largely responsible for this behavior. Now we seek to determine whether the same behavior is also seen in runs with transient CO_2 forcing, which are much more realistic. Our transient runs are forced, starting from PI, with CO_2 concentrations increasing at the rate of $1\%\text{yr}^{-1}$ and decreasing at $1\%\text{yr}^{-1}$. As seen in Figure 2.4a, the surface temperature response $|\Delta T_s|$ is stronger in the warming (red) than in the cooling (blue) case. Note that the responses computed from the last 50 years of the abrupt simulations at the corresponding CO_2 value (dots) are a good predictor of the response in the transient runs, demonstrating that the results of the abrupt runs carry

over to the transient runs. Together with the surface temperature, ERF also changes more rapidly in the warming than the cooling experiments, as seen in Figure 2.4b.

Next, we explore how the transient feedbacks (λ_{tr} , see Equation 2.2) change in the “warm” and “cold” cases (Figure 2.4c). The feedbacks timeseries are noisy at the beginning of the simulation, but in the last thirty years, the warm case shows 10% weaker (more positive) feedbacks compared to the cold case. The 10% difference indicates that S_G in the warming case should be higher than in the colder case. However, a robust difference in feedbacks only appears around year 130, whereas the $|\Delta T_s|$ asymmetry emerges much earlier, around year 60. This difference in the temporal evolution of the feedbacks, relative to the evolution of the forcing and S_G , adds additional strong evidence that the feedbacks are not driving the $|\Delta T_s|$ asymmetry.

Finally, as for the abrupt CO₂ runs, we correlate the asymmetry in global mean surface temperature response $\Delta_a T_s$ and effective radiative forcing $\Delta_a \text{ERF}$ (Figure 2.4d). We find a correlation of $r=0.96$, suggesting that the asymmetric changes in ERF drive the $|\Delta T_s|$ asymmetry between the “cold” and “warm” cases. As we can see in Figure 2.4c, the transient feedbacks are contributing to the $|\Delta T_s|$ asymmetry at the end of the run, but their impact is much smaller than the one from ERF.

2.4 Summary and Discussion

We have explored the effective climate sensitivity (S_G) dependence on CO₂ with abrupt *and* transient CO₂ experiments spanning the range $1/8\times$ to $8\times$ CO₂ using two distinct CMIP-class climate models. First, we have found a considerable asymmetry in surface temperature response, with the climate system warming more than cooling for identical factors used to increase and decrease the CO₂ concentration, starting from a pre-industrial climate. Second, we showed that the asymmetry is due to the non-logarithmic nature of CO₂ radiative forcing, not the feedback changes. Upon decomposing the total feedback into individual feedbacks, we found no simple explanation relating specific feedback changes to the changes in S_G across

the $1/8\times$ to $8\times$ CO₂ forcing range examined in this study.

Most studies to date have focused on the role of feedbacks in explaining the dependency of S_G on CO₂, with relatively little attention placed on radiative forcing. Indeed, consistent with these studies, we found that for warmer climates ($> 2 \times$ CO₂), feedbacks are important for determining the changing behavior of S_G with CO₂. However, by considering a broader range of CO₂ forcings, we have shown here that for cases in which CO₂ concentrations are less than PI values, non-logarithmic ERF is the primary driver of S_G changes. Our goal here has been to isolate the role of CO₂ alone, and we have set all other forcings to PI values. We have ignored the “slow” feedbacks present in cold climates (e.g., the LGM), such as the formation of land ice sheets.

The results with our abrupt runs have been shown to be robust with two climate models for simulations up to 150 years. One may argue that our runs are not equilibrated, and we agree with that caveat. However, we have found that the asymmetry and the key role of ERF are also robustly seen in the transient runs. Because of this, we expect that prolonging the abrupt simulation for more than 150 years will yield similar results. In any case, it will be important to repeat similar experiments with longer simulations as in LongRunMIP (Rugenstein et al. 2019) to confirm that this asymmetry is still present at long times closer to equilibration. Finally, our findings indicate that future studies should place more emphasis on accurately quantifying the changes in effective radiative forcing when studying the effective climate sensitivity dependency on CO₂. The feedbacks appear unable to explain the cooling phase.

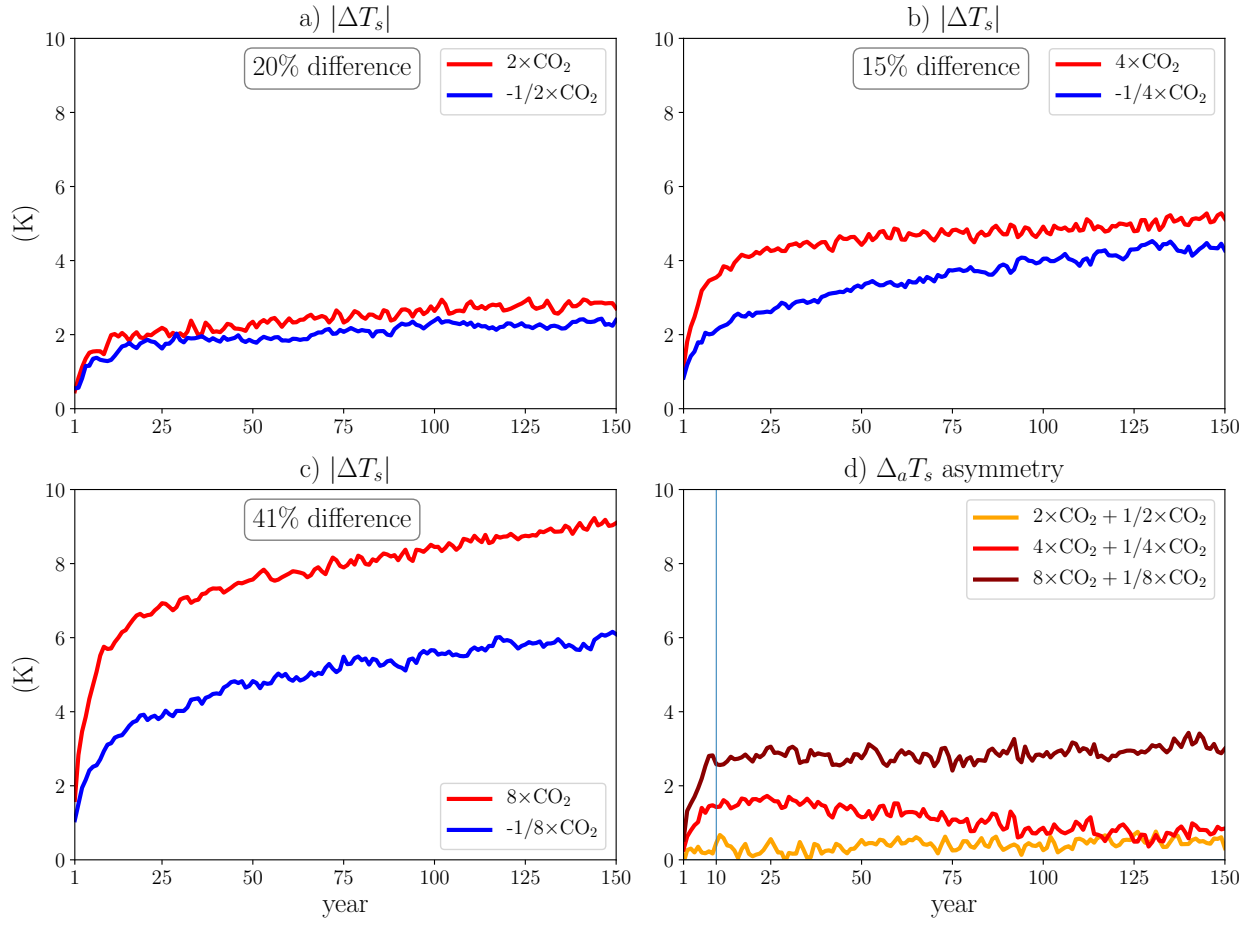


Figure 2.1: Timeseries of surface temperature response ($|\Delta T_s|$) for abrupt CO_2 runs with CESM-LE model. a) $2\times\text{CO}_2$ and $1/2\times\text{CO}_2$, b) $4\times\text{CO}_2$ and $1/4\times\text{CO}_2$, c) $8\times\text{CO}_2$ and $1/8\times\text{CO}_2$ runs, and d) surface temperature asymmetry ($\Delta_a T_s$) between “warm” and “cold” cases.

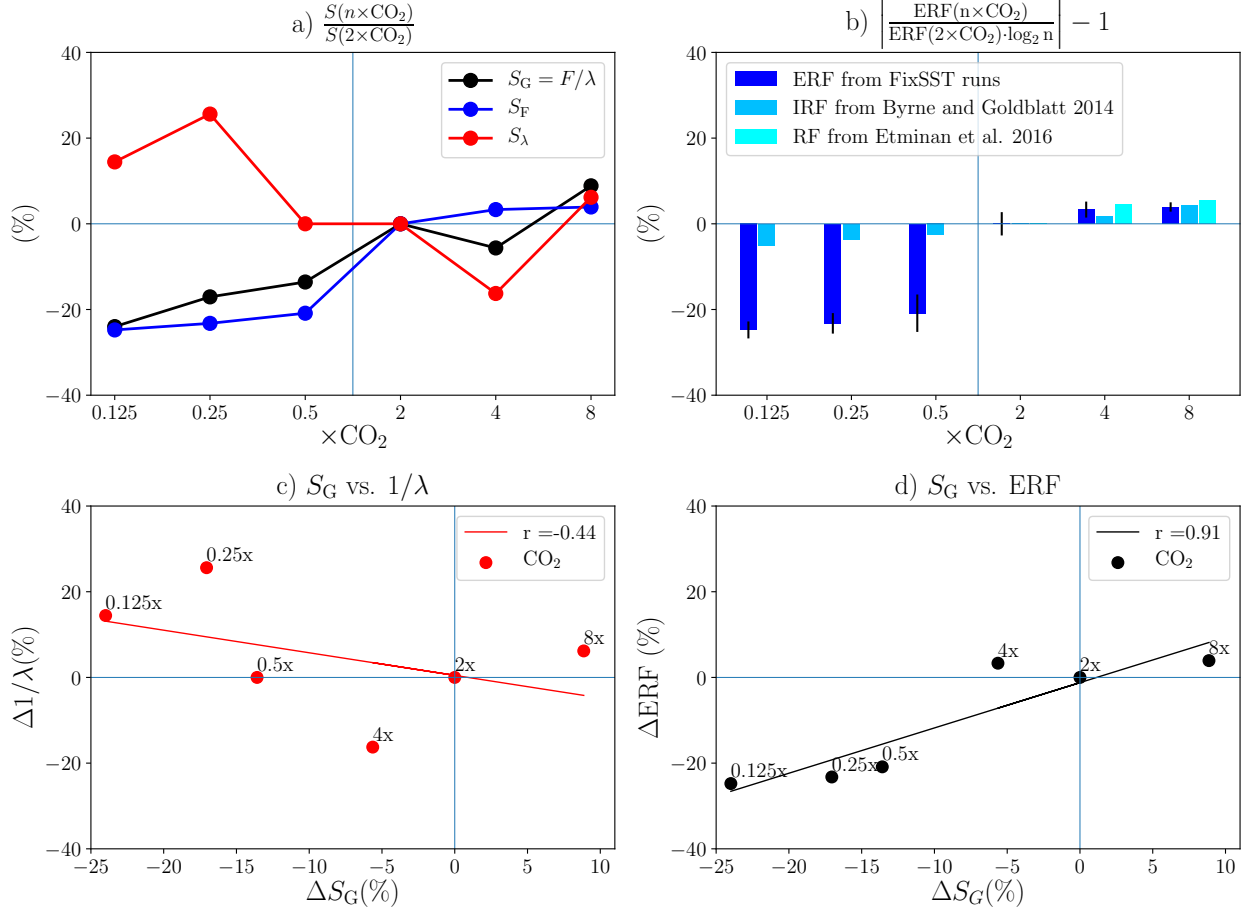


Figure 2.2: Percent change (from $2 \times \text{CO}_2$) for abrupt CO_2 runs with CESM-LE model of: a) climate sensitivity as x-intercept of Gregory Regression (black, S_G), as a function of ERF (blue, S_F), and as a function of $1/\lambda$ (red, S_λ); b) effective radiative forcing (dark blue, ERF), instantaneous radiative forcing (IRF) fit from Byrne and Goldblatt 2014 (light blue), and stratospherically adjusted radiative forcing (RF) fit from Etminan et al. 2016 (cyan). c) Percent change of S_G vs. $1/\lambda$ (red) and d) S_G vs. ERF (black). r is the Pearson correlation coefficient.

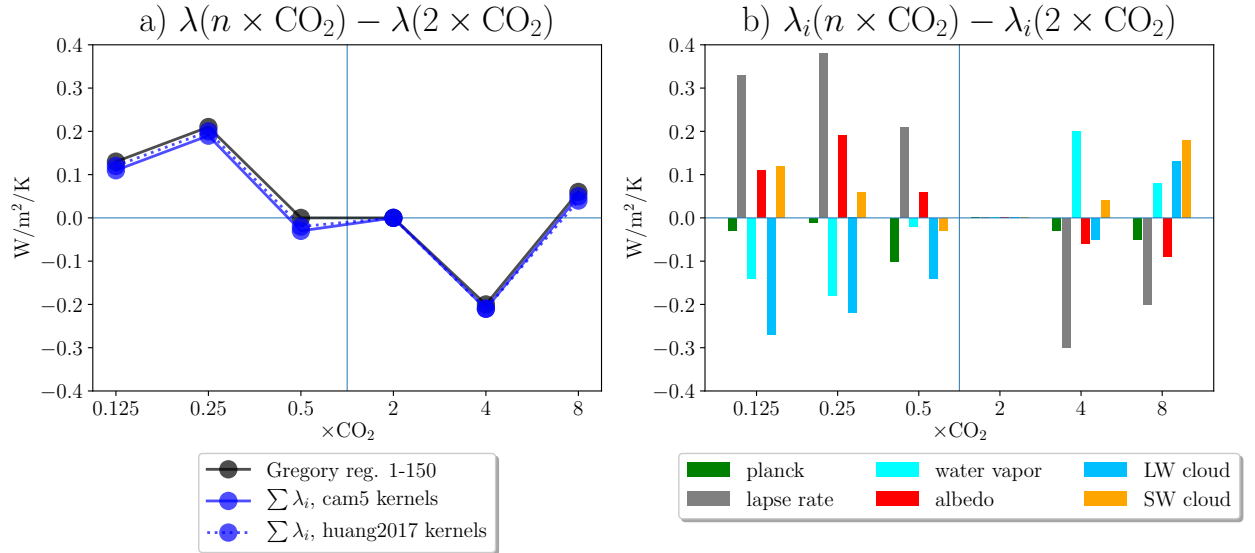


Figure 2.3: Feedbacks for abrupt CO_2 runs with CESM-LE model are shown as a difference from $2 \times \text{CO}_2$. a) Total feedback calculated with Gregory Regression years 1-150 (black), Pendergrass et al. 2018 kernels for CESM1-CAM5 (blue solid), and Huang et al. 2017 kernels (blue dashed). b) Individual feedbacks calculated with Pendergrass et al. 2018 kernels.

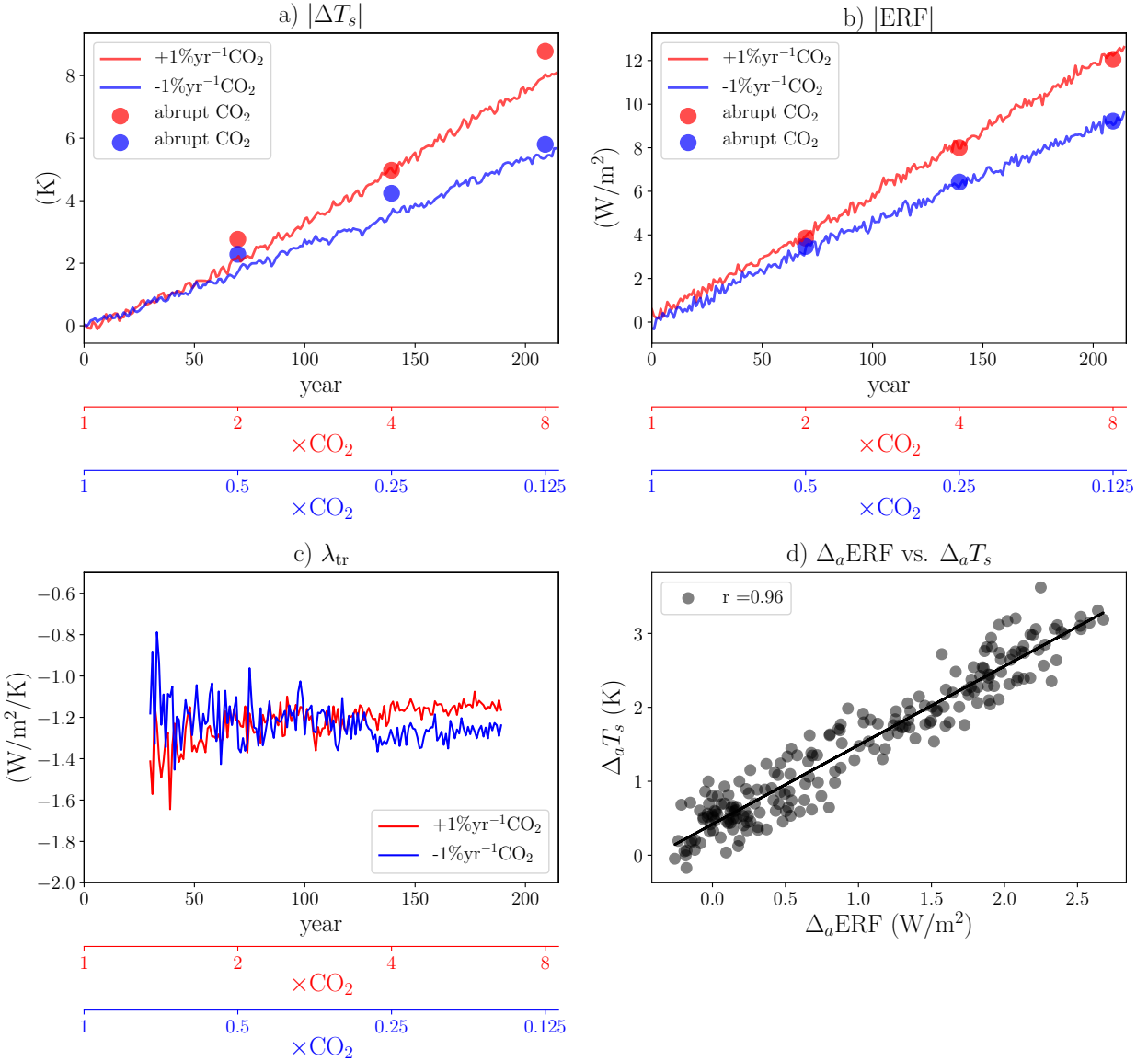


Figure 2.4: Transient runs annual timeseries with CESM-LE of a) the absolute value of surface temperature response ($|\Delta T_s|$), b) effective radiative forcing ($|\text{ERF}|$), c) net feedback (λ_{tr}), and d) correlation between asymmetries in $\Delta_a T_s$ and $\Delta_a \text{ERF}$. Responses from abrupt simulations are shown as dots.

Chapter 3: Non-monotonic Response of the Climate System to Abrupt CO₂ Forcing

Note: This chapter has been published in very near its present form as “Non-monotonic Response of the Climate System to Abrupt CO₂ Forcing” in Mitevski et al. [2021](#).

Abstract

We explore the climate system response to abrupt CO₂ forcing, spanning the range 1× to 8×CO₂, with two state-of-the-art coupled atmosphere-ocean-sea-ice-land models: the NASA Goddard Institute for Space Studies Model E2.1-G (GISS-E2.1-G) and the Community Earth System Model (CESM-LE). We find that the effective climate sensitivity is a non-monotonic function of CO₂ in both models, reaching a minimum at 3×CO₂ for GISS-E2.1-G, and 4×CO₂ for CESM-LE. A similar non-monotonic response is found in Northern Hemisphere surface temperature, sea-ice, precipitation, the latitude of zero precipitation-minus-evaporation, and the strength of the Hadley cell. Interestingly, the Atlantic meridional overturning circulation collapses when non-monotonicity appears and does not recover for larger CO₂ forcings. Analyzing the climate response over the same CO₂ range with slab-ocean versions of the same models, we demonstrate that the climate system’s non-monotonic response is linked to ocean dynamics.

3.1 Introduction

Equilibrium Climate Sensitivity (ECS) is the global mean surface warming at equilibrium following an instantaneous doubling of CO₂ relative to pre-industrial (PI) conditions (Knutti et al. [2017](#)). It is among the most important metrics in climate science, and is widely used

in economic and policy assessments of future global warming. Due to the complexity of the climate system, however, ECS is poorly constrained and its uncertainty has not narrowed across the reports of the Intergovernmental Panel on Climate Change (IPCC), from 1.9-5.2K in the first to 1.5-4.5K in the fifth report (Knutti and Hegerl 2008; Knutti et al. 2017; Tian 2015). ECS estimates from the Coupled Model Intercomparison Project 6 (CMIP6) span a still larger range of values (1.8-5.6K) (Zelinka et al. 2020). Analyzing individual feedback processes, in addition to both historical and paleoclimate records, a recent ECS assessment shows a 66% (17-83%) range spanning 2.6-3.9K (Sherwood et al. 2020).

Part of the difficulty in reducing ECS uncertainty is that it remains unclear to what degree ECS is a function of CO₂ concentration. Thus, while ECS estimates inferred from historical (observed) warming are lower than the ECS estimates derived from models subjected to abrupt CO₂ forcing (Knutti et al. 2017; Marvel et al. 2018), this does not necessarily imply that the model estimates are biased high. Comparisons of ECS derived from paleoclimate reconstructions also produce mixed results when compared with general circulation models (GCMs). While some paleoclimate studies indicate that climate sensitivity changes with CO₂ concentration (Friedrich et al. 2016; Shaffer et al. 2016; Stap et al. 2019), others do not (Martínez-Botí et al. 2015b). In contrast, for the present and future climate most GCM studies show that ECS increases with CO₂ (Caballero and Huber 2013; Colman and McAvaney 2009; Gregory et al. 2015; Jonko et al. 2013; Meraner et al. 2013). Of particular interest here, Meraner et al. 2013 showed that effective climate sensitivity (ECS_{eff}) increases monotonically in warmer climates, growing from 2.79K for an abrupt 2×CO₂ forcing to 10.22K for a 16×CO₂ forcing. However, that result was obtained using a single slab-ocean model, and whether it holds in the presence of a dynamically active ocean is still an open question.

Going beyond ECS, O’Gorman and Schneider 2008b explored the hydrological cycle response to increasing CO₂ using an idealized GCM, and reported a non-monotonic response in large-scale global mean precipitation with surface temperature. Idealized models also sug-

gest that the Hadley cell (HC) strength responds non-monotonically to surface temperature, reaching a maximum value near present-day climate (Levine and Schneider 2011; O’Gorman and Schneider 2008a). Studies with comprehensive models have also found that the width of the tropics will widen with increased warming (Chemke and Polvani 2019; Grise et al. 2019), but the question of whether the widening is monotonic over a wide range of CO₂ forcing in a comprehensive coupled climate model remains unexplored.

Here we perform a series of abrupt CO₂ model runs using the coupled atmosphere-ocean-sea-ice-land NASA Goddard Institute for Space Studies ModelE (GISS-E2.1-G) (Kelley et al. 2020), and Community Earth System Model Large Ensemble (CESM-LE) (Kay et al. 2015), to quantify the response of the climate system over an extensive range of CO₂ forcings (1× to 8×CO₂). Extending the work of Meraner et al. 2013, we explore the fully coupled atmosphere-ocean system (not only the slab-ocean system), and we go beyond ECS_{eff} to analyze the response of many other important components of the climate system, notably sea-ice, precipitation, and the HC. As shown below, we find the response for many such components to be not only a non-linear but a *non-monotonic* function of CO₂ forcing in both the GISS and CESM models.

3.2 Methods

We use fully coupled atmosphere-ocean-sea-ice-land (FOM) and the slab-ocean (SOM) versions of GISS-E2.1-G and CESM-LE. In the FOM version of GISS-E2.1-G, a 40-level atmospheric model with a resolution of 2° × 2.5° latitude/longitude is coupled to the 1° horizontal resolution 40-level GISS Ocean v1 (GO1) model: this model configuration contributed to the CMIP6 project, and is denoted as “GISS-E2-1-G, r1i1p1f1”. In the SOM version, the same atmospheric model is coupled to a mixed-layer ocean, with a prescribed ocean heat transport (OHT) derived from an atmosphere-only PI integration constrained with observed PI sea surface temperatures (Schmidt et al. 2006). The FOM of CESM-LE uses the Community Earth System Model version 1 (CESM1), the Community Atmosphere

Model version 5 (CAM5, 30 vertical levels), and parallel ocean program version 2 (POP2, 60 vertical levels) with approximately 1° horizontal resolution in all model components (Kay et al. 2015). The SOM configuration of CESM-LE uses the same atmospheric model coupled to a mixed-layer ocean with prescribed OHT (Bitz et al. 2012), kept constant at PI annual and monthly values of CESM, respectively.

For the FOM versions, we perform a series of abrupt CO₂ forcing runs, with $1.5 \times$ (only GISS-E2.1-G), $2 \times$, $3 \times$, $4 \times$, $5 \times$, $6 \times$, $7 \times$, and $8 \times$ CO₂ forcings, with all other trace gases, ozone concentrations, and aerosols fixed at PI values. We contrast these to a PI control run. To clarify: we are not progressively doubling CO₂, as done in some other studies, but we start each forced run from PI conditions. Following the $4 \times$ CO₂ protocol for CMIP6, all of our abrupt CO₂ model runs are integrated for 150 years starting from PI conditions.

In addition to the FOM runs, we also carry out 60-year-long integrations with the SOM version of the models for $2 \times$, $3 \times$, and $4 \times$ CO₂ forcings, and contrast them to a 60-year-long PI control run.

Following Forster et al. 2016, we estimate the effective radiative forcing (ERF_{fsst}) by performing 30-year-long integrations using prescribed pre-industrial sea surface temperatures (SST) and sea ice. As in the FOM simulations, these are performed for $1.5 \times$ (only for GISS-E2.1-G), $2 \times$, $3 \times$, $4 \times$, $5 \times$, $6 \times$, $7 \times$, and $8 \times$ CO₂. The ERF_{fsst} is then calculated as the difference in global mean net top of the atmosphere (TOA) flux between PI and $n \times$ CO₂, and it includes the adjustments of both the stratosphere and troposphere (Sherwood et al. 2015).

Following Meraner et al. 2013, we consider the Earth's energy balance in response to an abrupt CO₂ forcing in terms of

$$\Delta R = F + \lambda \Delta T \quad (3.1)$$

where F is the radiative forcing, ΔR is the TOA radiative imbalance, ΔT is the surface temperature response, and λ is the total feedback parameter. ECS_{eff}, defined as the temperature response when $\Delta R = 0$, is then calculated from the simple formula $ECS_{eff} = -F/\lambda$.

For each run, we perform a regression analysis (Gregory et al. 2004) of ΔR vs. ΔT , using annual mean values, to calculate total radiative feedbacks (λ , slope) and the effective radiative forcing (ERF_{reg}, y-intercept). We then evaluate the effective climate sensitivity, $ECS_{\text{eff}} = -\text{ERF}_{\text{fsst},2\times\text{CO}_2}/\lambda$, where ERF_{fsst,2×CO₂} is the ERF_{fsst} estimated from the 2×CO₂ fixed SST experiment.

In addition to the global mean surface temperature response, we examine the response of precipitation, sea-ice extent, the width of the tropical belt, and the strength of the Atlantic Meridional Overturning Circulation (AMOC, defined as the maximum between 30°N to 55°N and 800m to 2000m). To quantify the tropical width, we use the edge of the dry zones, ϕ_{P-E} , defined as the latitude where precipitation (P) minus evaporation (E) is zero poleward of the subtropical minimum and equatorward of 60° (see Fig. 1 in Grise and Polvani 2016). We calculate ϕ_{P-E} using the tropical-width diagnostics (TropD) code documented in Adam et al. 2018 by applying the “zero_crossing” method.

Finally, in all figures below we show the average over the last 50 years of the FOM runs and of the last 30 years of the SOM runs. For all quantities of interest, the annual mean response (denoted by Δ) is computed as the difference from the corresponding PI control run. The linearity of various climate metrics is evaluated with respect to the radiative forcing (RF) associated with each CO₂ perturbation, calculated from the expression $5.35 \ln(n \times \text{CO}_2 / 1 \times \text{CO}_2)$ (Byrne and Goldblatt 2014) where, for each run, n is the CO₂ multiple of the PI value. Note that, upon comparing this logarithmic RF value to ERF_{fsst} and ERF_{reg}, we find values that are very close to ERF_{fsst} and relatively close to ERF_{reg} (see Fig. B.1).

3.3 Results

Table 3.1 summarizes the Gregory regression analysis for all CO₂ integrations for both FOM and SOM configurations (the individual regression plots for each run are shown in Fig. B.2). Feedbacks in the FOM runs (denoted λ_F , Table 3.1, rows 1,7) initially increase

Table 3.1: Total feedbacks λ [$\text{Wm}^{-2}\text{K}^{-1}$] (slope in Gregory regression plot), Effective Climate Sensitivity (ECS_{eff}) calculated as $-\text{ERF}_{\text{fsst},2\times\text{CO}_2}/\lambda$ [K] with $\text{ERF}_{\text{fsst},2\times\text{CO}_2}$ being 3.63 Wm^{-2} for GISS-E2.1-G and 3.88 Wm^{-2} for CESM-LE model, and global surface temperature response ΔT_s [K].

	1.5×CO ₂	2×CO ₂	3×CO ₂	4×CO ₂	5×CO ₂	6×CO ₂	7×CO ₂	8×CO ₂
GISS-E2.1-G								
λ_F	-1.72 (-1.89, -1.56)	-1.62 (-1.77, -1.47)	-1.86 (-2.06, -1.72)	-1.51 (-1.63, -1.39)	-1.35 (-1.44, -1.24)	-1.26 (-1.34, -1.15)	-1.24 (-1.31, -1.14)	-1.22 (-1.29, -1.12)
$\text{ECS}_{\text{eff},F}$	2.11 (1.92, 2.34)	2.24 (2.05, 2.46)	1.95 (1.76, 2.11)	2.41 (2.23, 2.60)	2.69 (2.51, 2.92)	2.89 (2.71, 3.14)	2.93 (2.77, 3.19)	2.99 (2.82, 3.24)
$\Delta T_{s,F}$	1.28 (1.24, 1.32)	2.17 (2.12, 2.22)	2.83 (2.78, 2.88)	4.16 (4.11, 4.21)	5.18 (5.13, 5.23)	6.03 (5.98, 6.08)	6.70 (6.65, 6.75)	7.36 (7.31, 7.41)
λ_S	-	-1.30 (-1.40, -1.24)	-1.22 (-1.28, -1.15)	-1.20 (-1.24, -1.13)	-	-	-	-
$\text{ECS}_{\text{eff},S}$	-	2.80 (2.62, 2.93)	2.97 (2.84, 3.16)	3.04 (2.92, 3.22)	-	-	-	-
$\Delta T_{s,S}$	-	3.13 (3.10, 3.16)	4.99 (4.97, 5.01)	6.43 (6.41, 6.45)	-	-	-	-
CESM-LE								
λ_F	-	-1.08 (-1.20, -0.94)	-0.99 (-1.08, -0.88)	-1.25 (-1.31, -1.17)	-1.10 (-1.18, -1.00)	-1.03 (-1.11, -0.92)	-0.97 (-1.05, -0.89)	-0.97 (-1.04, -0.88)
$\text{ECS}_{\text{eff},F}$	-	3.60 (3.23, 4.11)	3.95 (3.59, 4.43)	3.11 (2.96, 3.32)	3.53 (3.30, 3.88)	3.79 (3.51, 4.21)	4.00 (3.70, 4.38)	3.99 (3.73, 4.39)
$\Delta T_{s,F}$	-	2.70 (2.64, 2.77)	4.47 (4.40, 4.55)	4.99 (4.90, 5.07)	6.22 (6.09, 6.35)	7.25 (7.12, 7.38)	8.06 (7.94, 8.18)	8.79 (8.67, 8.91)
λ_S	-	-0.80 (-0.91, -0.66)	-0.83 (-0.89, -0.77)	-0.82 (-0.89, -0.72)	-	-	-	-
$\text{ECS}_{\text{eff},S}$	-	4.90 (4.30, 5.79)	4.66 (4.35, 5.03)	4.74 (4.36, 5.35)	-	-	-	-
$\Delta T_{s,S}$	-	4.00 (3.96, 4.05)	6.37 (6.32, 6.42)	8.32 (8.28, 8.35)	-	-	-	-

^f Fully coupled (FOM); ^s Slab-ocean (SOM);

All confidence intervals (CIs) are 95%; CIs for λ and ECS_{eff} are obtained by resampling the linear regressions 10,000 times, and CIs for ΔT are calculated using Student's *t*-distribution.

(i.e., become less negative) with rising CO₂, but reach a minimum (maximum of $|\lambda_F|$) value at 3×CO₂ for GISS-E2.1-G and 4×CO₂ for CESM-LE. More precisely, for GISS-E2.1-G, λ_F becomes more positive from 1.5× to 2×CO₂ (-1.72 to -1.62), reaches an absolute minimum at 3×CO₂ ($\lambda_F = -1.86$), and then monotonically increases to a value of -1.22 at 8×CO₂. In other words, ECS_{eff,F}, which is inversely related to λ_F , reaches an absolute minimum (1.95) at 3×CO₂ for the FOM version of GISS-E2.1-G (Table 1, row 2). Similarly, for CESM-LE, λ_F becomes more positive from 2× to 3×CO₂ (-1.08 to -0.99), reaches an absolute minimum at 4×CO₂ ($\lambda_F = -1.25$), and then monotonically increases to a value of -0.97 at 8×CO₂. ECS_{eff,F} also reaches reaches an absolute minimum (3.11) at 4×CO₂ for the FOM run (Table 1, row 8).

In contrast to the FOM runs, the SOM integrations do not show this non-monotonicity for either model. Rather, the feedbacks in the SOM runs (denoted λ_S , Table 3.1, rows 4,10) increase monotonically from 2× to 4×CO₂ (the difference between 3× and 4×CO₂ in CESM-LE runs is not statistically significant). Correspondingly, ECS_{eff,S}, does not exhibit the minimum at 3×CO₂ for GISS-E2.1-G and 4×CO₂ for CESM-LE featured in the fully coupled runs. Our SOM results confirm the findings of Meraner et al. 2013, who also reported that ECS_{eff} increases monotonically with CO₂ concentrations using a SOM model. The monotonic behavior of ECS_{eff} with a SOM model clearly points to the ocean dynamics as key to understanding the non-monotonicity.

Next, going beyond the numerical value ECS, we examine several key aspects of the climate system response to increasing CO₂. The global mean surface temperature response ΔT_s (green lines in Fig. 3.1a,b and Table 3.1, rows 3,9) is a monotonic function of RF, although one can see an inflection in NH surface temperatures at 3×CO₂ in GISS-E2.1-G and 4×CO₂ in CESM-LE. Partitioning ΔT_s into northern (red lines in Fig. 3.1a,b) and southern (blue lines in Fig. 3.1a,b) hemispheric mean components reveals a clear cooling in the northern hemisphere (NH) as the forcing is increased from 2× to 3×CO₂ for GISS-E2.1-G and 3× to 4×CO₂ for CESM-LE model (this corresponds to the ECS_{eff} minimum).

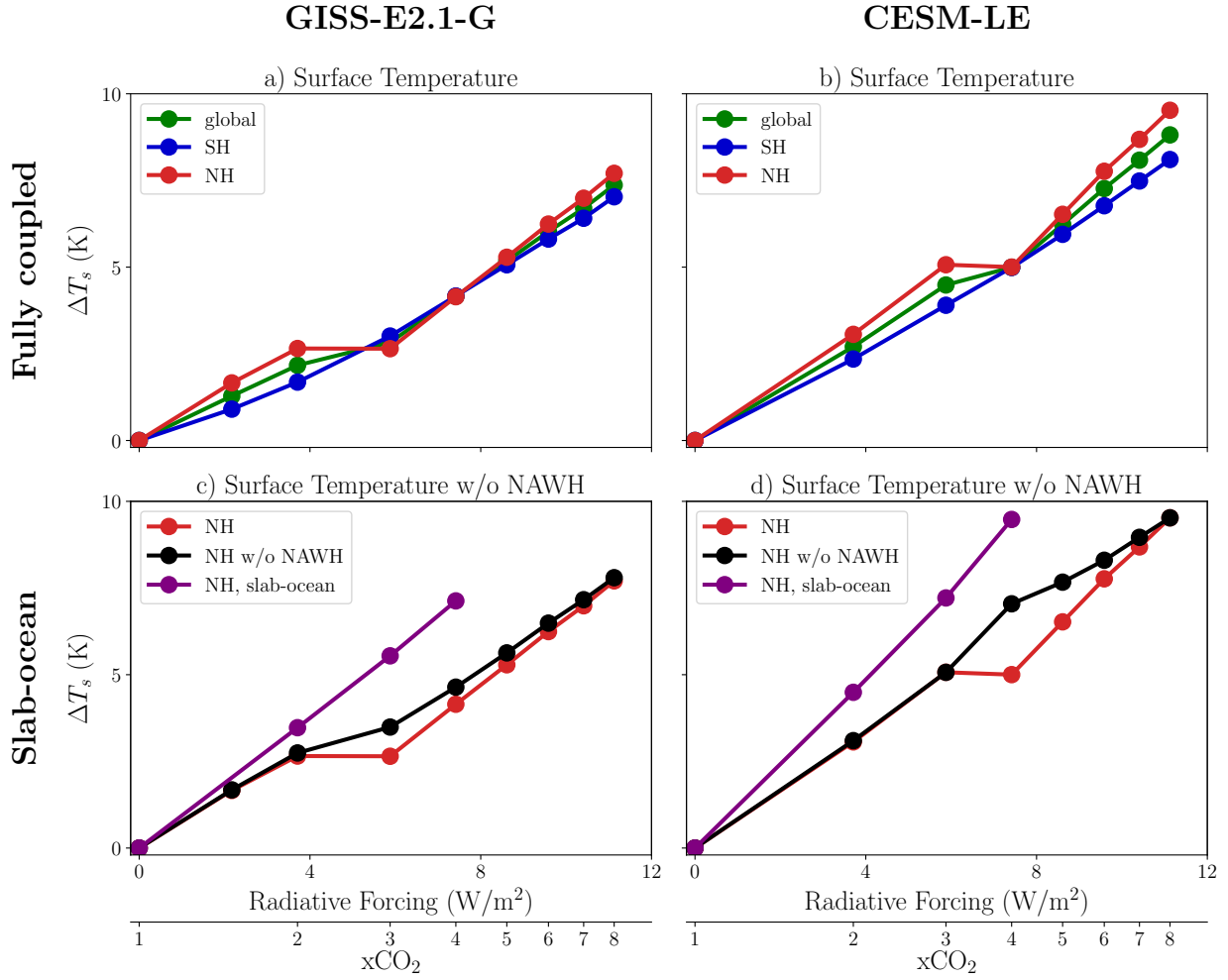


Figure 3.1: Annual surface temperature response (ΔT_s) as a function of radiative forcing in a,b) fully coupled model (FOM) runs for the global mean (green), NH (red), and SH (blue), and c,d) for the NH with (red) and without the North Atlantic Warming Hole (NAWH, black) and slab-ocean (SOM) runs (purple). Panels a,c) show GISS-E2.1-G data and panels b,d) show CESM-LE data.

In the southern hemisphere (SH), on the other hand, the surface temperature increases monotonically. The non-monotonic behavior in the NH surface temperature is absent in the SOM runs in both models (Fig. 3.1c,d, purple lines). This again demonstrates that ocean dynamics is responsible for the non-monotonic behavior of the NH surface temperature.

Inspection of global maps of ΔT_s (see Fig. 3.2) shows that the non-monotonicity in the coupled model run at $3\times\text{CO}_2$ for GISS-E2.1-G and $4\times\text{CO}_2$ for CESM-LE is associated with a non-monotonic response of the North Atlantic Warming Hole (NAWH), where there is a decline in SST in response to increasing greenhouse gases. To evaluate the contribution of this regional cooling to the total NH temperatures, we mask out all grid points corresponding to the NAWH, which we define here as regions where ΔT_s is negative (blue areas in Fig. 3.2). The resulting ΔT_s (Fig. 3.1c,d, black lines) is monotonic in NH as in the SOM runs. The latter, along with the behavior in the SOM runs, strongly suggests that changes in ocean dynamics are responsible for the non-monotonicity in NH surface temperature exhibited in the coupled model.

Recently, Chemke et al. 2020 showed that the formation of the NAWH in CESM-LE and the Max Planck Institute Earth System Model 100-member Grand Ensemble (MPI-GE) (Maher et al. 2019) under historical forcing from 1850 to 2005 and Representative Concentration Pathway 8.5 (RCP8.5) through 2100, is caused by a reduction in surface meridional OHT. Additionally, a reduction in the meridional overturning circulation (MOC) has been shown to reduce transient warming in numerous studies (Caesar et al. 2020; Palter 2015; Rugenstein et al. 2013; Trossman et al. 2016; Winton et al. 2013). Thus, it is tempting to relate the AMOC response (which plays a central role in the poleward OHT) to the surface temperature response. This can be seen in Fig. B.3a,b: as CO_2 increases, the AMOC weakens, and the associated reduction in OHT is accompanied by the NAWH, which maximizes (relative to ambient global warming) at $3\times\text{CO}_2$ in GISS-E2.1-G and $4\times\text{CO}_2$ in CESM-LE (Fig. 3.2c,f) when the AMOC entirely collapses. At higher forcings, $4\times$ to $8\times\text{CO}_2$ for GISS-E2.1-G, and $5\times$ to $8\times\text{CO}_2$ for CESM-LE, the AMOC remains shut down, but the surface

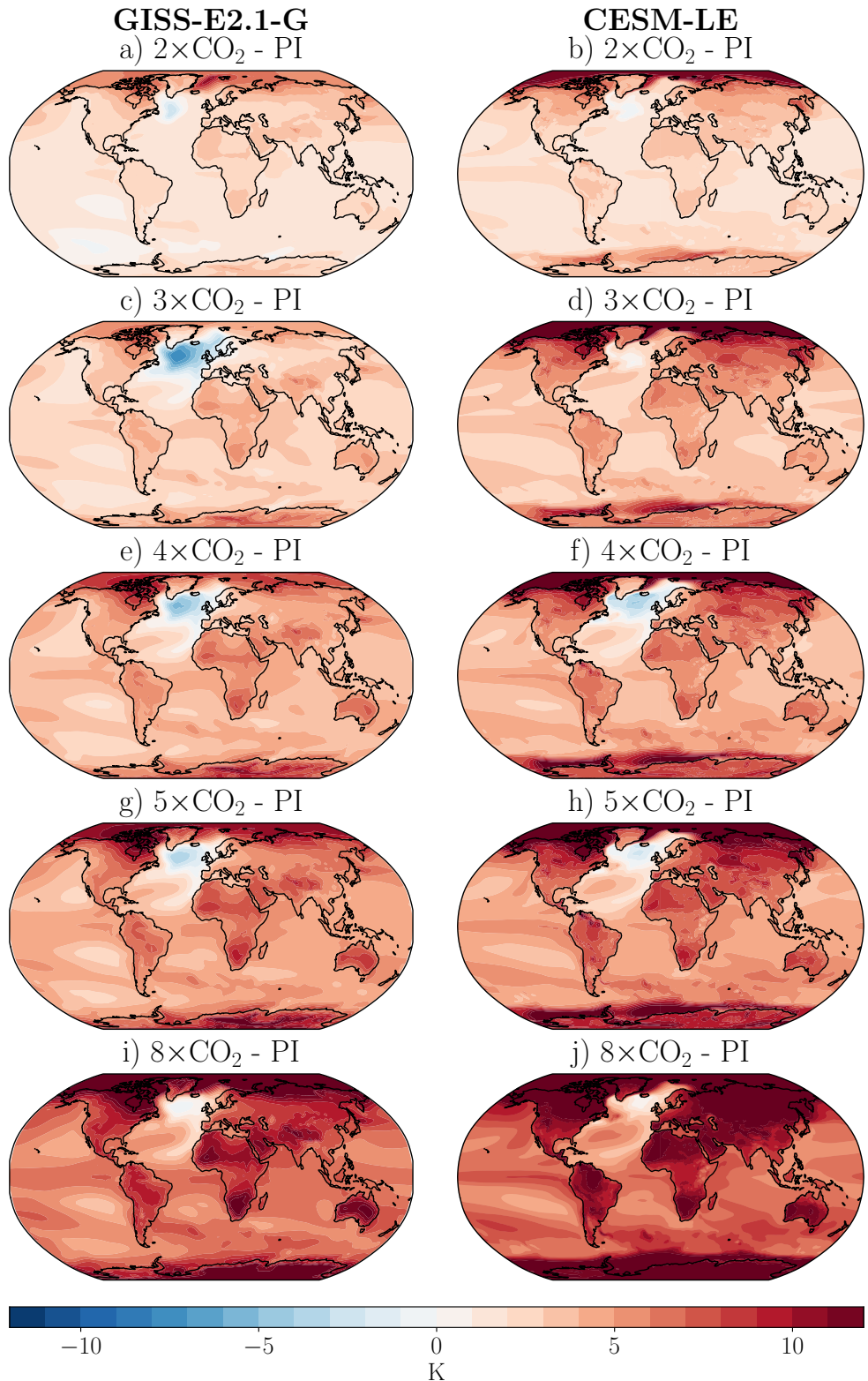


Figure 3.2: Annual mean surface temperature response (ΔT_s) to a,b) $2\times\text{CO}_2$, c,d) $3\times\text{CO}_2$, e,f) $4\times\text{CO}_2$, g,h) $5\times\text{CO}_2$, and i,j) $8\times\text{CO}_2$ shown for both GISS-E2.1-G (left) and CESM-LE (right) model runs. Note: higher warming than 12K is shown with same color as 12K.

warms as CO_2 increases (Fig. 3.2e,g-j), as seen in the linear progression of ΔT_s for forcings higher than $4\times\text{CO}_2$ for GISS-E2.1-G and $5\times\text{CO}_2$ for CESM-LE (Fig. 3.1a,b). However, the NAWH temperature relative to ambient warming in the NH stays relatively constant. Note that the AMOC collapse in our models is by no means exceptional; for example, most CMIP5 and CMIP6 models also exhibit a substantial AMOC weakening in response to an abrupt quadrupling of CO_2 (Fig. B.3c,d).

The non-monotonicity of the response to increased CO_2 is not only seen in surface temperature: it pervades many aspects of the climate system. Consider the sea-ice response, shown in Fig. 3.3 for both models. For GISS-E2.1-G, while the Arctic sea-ice decreases with CO_2 (Fig. 3.3, left) at large concentrations, from $2\times$ to $3\times\text{CO}_2$ sea-ice actually *increases* (Fig. 3.3c) over the North Atlantic around Greenland and the Norwegian sea, consistent with a maximum NAWH temperature decrease at $3\times\text{CO}_2$ (Fig. 3.2c). For CESM-LE, while Arctic sea-ice decreases with CO_2 (Fig. 3.3, right) at large concentrations, from $3\times$ to $4\times\text{CO}_2$ (Fig. 3.3d,f) sea-ice actually *increases* (less red at $4\times\text{CO}_2$ than $3\times\text{CO}_2$). Furthermore, the non-monotonic response of Arctic sea-ice is not merely regional in scope: it is clearly seen in the annual NH sea-ice extent, which exhibits a significant “jump” between $2\times$ and $3\times\text{CO}_2$ for GISS-E2.1-G and $3\times$ and $4\times\text{CO}_2$ for CESM-LE shown in Fig. 3.4a and Fig. 3.4b, respectively. While numerous studies have explored the mechanisms by which Arctic sea-ice loss directly affects the behavior of the AMOC through increased freshwater fluxes (Liu et al. 2019; Oudar et al. 2017; Scinocca et al. 2009; Sévellec et al. 2017; Sun et al. 2018), here the relationship is not simply “one-way” as sea-ice *increases* between $2\times$ to $3\times\text{CO}_2$ for GISS-E2.1-G, and between $3\times$ to $4\times\text{CO}_2$ for CESM-LE, while the AMOC weakens. This is consistent with the fact that the physical processes associated with how sea-ice modulates the AMOC are still unclear in comprehensive fully coupled climate models (Liu et al. 2019). A detailed investigation of the relationship between Arctic ice and AMOC is beyond the scope of this study, but an analysis of the AMOC collapse in a previous generation of the GISS model (GISS-E2-G) can be found in Rind et al. 2018.

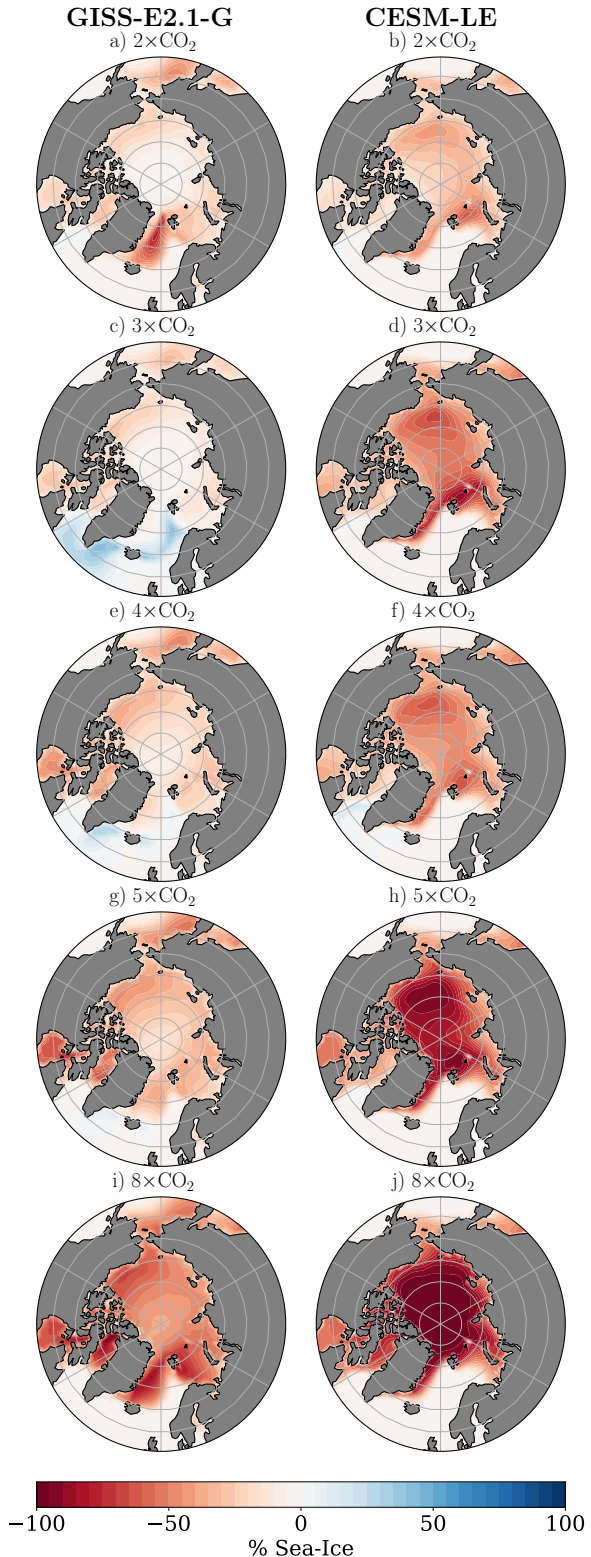


Figure 3.3: Annual Arctic sea-ice response to a,b) $2\times\text{CO}_2$, c,d) $3\times\text{CO}_2$, e,f) $4\times\text{CO}_2$, g,h) $5\times\text{CO}_2$, and i,j) $8\times\text{CO}_2$ shown for both GISS-E2.1-G (left) and CESM-LE (right) model runs.

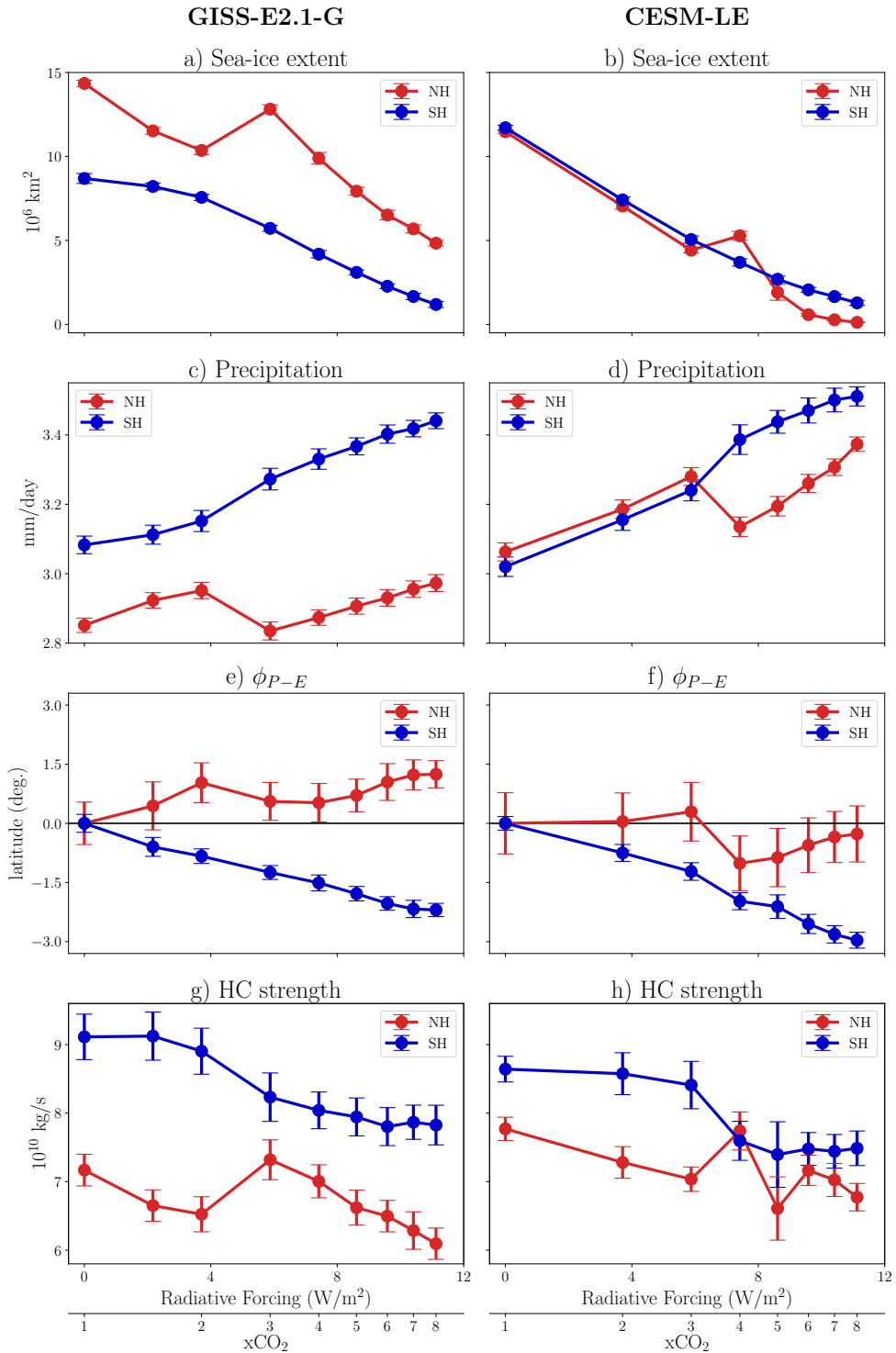


Figure 3.4: Annual mean a,b) sea-ice extent (10^6 km^2) defined as grid cell areas with more than 15% ice concentration, c,d) precipitation (mm/day), e,f) dry zone edge (ϕ_{P-E}), and g,h) HC strength (Ψ_{500}) for SH (blue) and NH (red) as a function of radiative forcing. Error bars denote 95% confidence intervals calculated using Student's t -distribution.

Many other climate variables also exhibit a non-monotonic response to increased CO₂ in both models. Of notable interest is the response of precipitation (Fig. 3.4c,d), which generally increases in both hemispheres as CO₂ concentrations rise (as one expects), but actually declines in the NH (red line) between 2× and 3×CO₂ for GISS-E2.1-G, and between 3× and 4×CO₂ for CESM-LE, in tandem with temperature (Fig. 3.1a,b) and sea-ice extent (Fig. 3.4a,b). Interestingly, note that NH precipitation at 3×CO₂ in GISS-E2.1-G is lower than in the PI control (RF = 0) and barely recovers to its 2×CO₂ value even at 8×CO₂ forcing. Even in the SH, where precipitation increases monotonically, one can see a marked increase in the slope between 2× and 3×CO₂ for GISS-E2.1-G, and between 3× and 4×CO₂ for CESM-LE. These features of the precipitation response are absent in the SOM runs (Fig. B.4a,b), and therefore, most likely are related to changes in the ocean dynamics.

The non-monotonic behavior is not confined to high or middle-latitude but extends to the tropics as well. The width of the tropical belt (Seidel et al. 2008), which is projected to increase with CO₂ (Chemke and Polvani 2019; Grise et al. 2019), also exhibits a non-monotonic behavior. Consider the response of ϕ_{P-E} (Fig. 3.4e,f), which is a critical metric of the hydrological cycle, separating zones of net precipitation and net evaporation. In the SH, ϕ_{P-E} shifts poleward with increased CO₂ in both models. On the other hand, in the NH, the models show a non-monotonic widening, with a contraction between 2× and 3×CO₂ in GISS-E2.1-G, and between 3× and 4×CO₂ in CESM-LE. By comparison, ϕ_{P-E} increases monotonically in the SOM runs in the NH (Fig. B.4c,d), which reinforces the notion that changes in ocean dynamics are important drivers of the non-monotonic climate response exhibited in these models.

The response of the edge of the dry zones (ϕ_{P-E}) is not only affected by atmospheric circulation changes but also by changes in moisture content, which is related to temperature, as shown in Chemke and Polvani 2019. Investigation of the moisture content in the NH (light blue line in Fig. B.5a,b) shows a clear “jump” between 2× and 3×CO₂ for GISS-E2.1-G, and between 3× and 4×CO₂ for CESM-LE, and confirms that changes in moisture content

affect the response in ϕ_{P-E} , as one expects from the Clausius-Clapeyron relation and the temperature response shown in Fig. 3.1.

Finally, we consider the strength of the HC, computed using the extremum of the stream-function Ψ at 500 hPa (Ψ_{500}): it also exhibits a non-monotonic behavior in the NH, with a “jump” between $2\times$ and $3\times$ CO₂ in GISS-E2.1-G, and between $3\times$ and $4\times$ CO₂ in CESM-LE, as seen in Fig. 3.4g and Fig. 3.4h, respectively (again, note that the “jump” disappears in the SOM runs (Fig. B.4e,f)). A detailed study contrasting the different behaviors of various tropical width metrics is beyond the scope of this study. The goal of this paper is simply to illustrate that the non-monotonic response to increased CO₂ appears in a wide array of different metrics of the climate system.

3.4 Summary and Discussion

We have explored the climate system response to abrupt CO₂ forcing, spanning the range of $1\times$ to $8\times$ CO₂ using the GISS-E2.1-G and the CESM-LE models. We found that, in both models, for many climate metrics – ECS_{eff}, Arctic sea-ice, Northern Hemisphere precipitation, tropical expansion, and Hadley cell strength – the response to increased CO₂ is not only a non-linear but, in fact, a non-monotonic function of the RF. Our models show that increasing CO₂ from $2\times$ to $3\times$ PI concentrations in GISS-E2.1-G, and from $3\times$ to $4\times$ PI in CESM-LE model, results – surprisingly – in smaller ECS_{eff}, expanded Arctic sea-ice, reduced Northern hemisphere precipitation, contracted dry zones and a stronger Hadley cell. Analyzing a companion set of runs with the slab-ocean version of the same models reveals that this non-monotonic behavior is related to the changes in the ocean dynamics under CO₂ forcing.

Our findings are robust across two climate models for runs up to 150 years. It will be important to repeat a similar exercise with other climate models to determine if non-monotonicity is a robust feature, and not an artifact of the models used here. Additionally, it would be important to extend the model runs closer to equilibration (minimum of 1000 years)

and verify whether the monotonicity persists. We extended a subset of these integrations ($2\times$, $3\times$, and $4\times\text{CO}_2$ with GISS-E2.1-G) for an additional 150 years, and our main results are unchanged. More broadly, while the DECK experiments in CMIP at present only require a single abrupt (4x) CO_2 experiment, thereby limiting our ability to test for non-monotonicity using the CMIP output, our findings suggest that it may be important to explore a broader range of CO_2 forcings in future CMIPs.

Finally, one may ask whether the non-monotonicity of the response to CO_2 forcing detailed above is an artifact of the abrupt nature of the forcing. In practice, atmospheric concentrations of carbon dioxide increase progressively, and an abrupt change is highly unrealistic. Thus, in addition to validating the result presented here with other climate models, it will be essential to explore whether the non-monotonicity is also present in forced simulations with continuous forcing (e.g., 1% per year), and to determine whether the transient climate response also exhibits non-monotonic behavior. Such questions, of course, are beyond the scope of the present study, but we hope to report on them in future papers.

Chapter 4: Non-monotonic feedback dependence under abrupt CO₂ forcing due to a North Atlantic pattern effect

Note: This chapter has been published in very near its present form as “Non-monotonic feedback dependence under abrupt CO₂ forcing due to a North Atlantic pattern effect” in Mitevski et al. 2023.

Abstract

Effective climate sensitivity (EffCS), commonly estimated from model simulations with abrupt 4×CO₂ for 150 years, has been shown to depend on the CO₂ forcing level. To understand this dependency systematically, we performed a series of simulations with a range of abrupt CO₂ forcing in two climate models. Our results indicate that normalized EffCS values in these simulations are a non-monotonic function of the CO₂ forcing, decreasing between 3× and 4×CO₂ in CESM1-LE (2× and 3×CO₂ in GISS-E2.1-G) and increasing at higher CO₂ levels. The minimum EffCS value, caused by anomalously negative radiative feedbacks, arises mainly from sea-surface temperature (SST) relative cooling in the tropical and subtropical North Atlantic. This cooling is associated with the formation of the North Atlantic Warming Hole and Atlantic Meridional Overturning Circulation collapse under CO₂ forcing. Our findings imply that understanding changes in North Atlantic SST patterns is important for constraining near-future and equilibrium global warming.

4.1 Introduction

Equilibrium climate sensitivity (ECS), the equilibrium global-mean surface air temperature response to a doubling of atmospheric CO₂ relative to pre-industrial (PI) levels, is one

of the most important metrics in climate science. The Charney 1979 report (Charney et al. 1979) estimated a “likely” ECS range of 1.5-4.5K; most recently, a tighter range of ECS values between 2.6-3.9K was established using a Bayesian framework that combines multiple lines of evidence (Sherwood et al. 2020).

When evaluated from climate models, ECS is often approximated with an effective climate sensitivity (EffCS), estimated from 150-year abrupt CO₂ quadrupling simulations within coupled global climate models (GCMs), with an underlying assumption that EffCS remains constant with different CO₂ doublings and over time. However, previous modeling (Bloch-Johnson et al. 2021a; Mauritsen et al. 2019; Meraner et al. 2013; Mitevski et al. 2021; Sherwood et al. 2020; Zhu and Poulsen 2020) and paleoclimate studies (Anagnostou et al. 2020; Anagnostou et al. 2016; Farnsworth et al. 2019; Friedrich et al. 2016; Shaffer et al. 2016; Zhu et al. 2019) have shown that EffCS may not be linear with each successive CO₂ doubling. It tends to increase at higher CO₂ values primarily due to a nonlinear temperature dependence of the radiative feedbacks (λ), referred to as the state-dependence of feedbacks (Bloch-Johnson et al. 2021a; Sherwood et al. 2015), with minor contributions from nonlinear CO₂ dependence of radiative forcing (Mitevski et al. 2022).

However, previous attempts to study the state dependence have been limited to CO₂-doubling scenarios (2×, 4×, 8×CO₂) (Good et al. 2016; Rugenstein et al. 2019), whereas the shared socioeconomic pathway for the highest emission scenarios (SSP5-8.5) projects a transient increase of greenhouse gas forcing up to 8×CO₂ at the year 2300 (Meinshausen et al. 2020) passing through all the intermediate states of $n \times \text{CO}_2$ ($n = 2, 3, 4, 5, 6, 7, 8$). Moreover, previous studies on state dependence have been focused on how EffCS and feedbacks vary in response to changes in global-mean temperatures under different CO₂ forcing (Bloch-Johnson et al. 2021a; Caballero and Huber 2013; Meraner et al. 2013). Additionally, there has been enormous attention on the dependence of EffCS and feedbacks on the spatial patterns of surface warming (e.g., Andrews et al. 2022; Andrews et al. 2015; Rugenstein et al. 2020; Rugenstein et al. 2016; Zhou et al. 2016). Here, we systematically examine the dependence

of EffCS on the level of abrupt CO₂ forcing, as well as its connection to the spatial patterns of surface warming and climate feedbacks. To accomplish this, we conduct and analyze GCM experiments with a range of abrupt CO₂ forcings including 2×, 3×, 4×, 5×, 6×, 7×, and 8×CO₂ relative to PI level (hereafter denoted as abrupt $n \times$ CO₂ experiments).

4.2 Materials and Methods

4.2.1 Models and Experiments

We use the original large ensemble version of the Community Earth System Model (CESM1-LE). CESM1-LE comprises the Community Atmosphere Model version 5 (CAM5, 30 vertical levels) and parallel ocean program version 2 (POP2, 60 vertical levels) with approximately 1° horizontal resolution in all model components (Kay et al. 2015). Some of the results are shown with the GISS-E2.1-G model (Kelley et al. 2020) in Appendix C. All experiments in this work are with abrupt CO₂ forcing.

We perform abrupt $n \times$ CO₂ experiments with the coupled version of the CESM1-LE and GISS-E2.1-G models (coupled runs) for 150 years with 2×, 3×, 4×, 5×, 6×, 7×, and 8×CO₂ forcing, with all other trace gases, aerosols, ozone concentrations, and solar forcing fixed at PI values. The response is defined as the difference between the $n \times$ CO₂ runs and the PI control run. The same experiments were analyzed in Mitevski et al. 2021 and Mitevski et al. 2022.

To estimate the effective radiative forcing (ERF) as per Forster et al. 2016, we perform prescribed pre-industrial SST and sea-ice runs for 30 years for each 2×, 3×, 4×, 5×, 6×, 7×, and 8×CO₂. The ERF is then calculated as the global mean net top of the atmosphere (TOA) net radiation between PI and $n \times$ CO₂, and it includes the stratospheric and tropospheric adjustments (Sherwood et al. 2015).

We also utilize atmosphere-only runs (AGCM) with prescribed monthly SST values taken from the 150-year abrupt $n \times$ CO₂ runs. The prescribed SST values are monthly data for 150 years. The CO₂ concentration, ozone concentrations, aerosols, solar forcing, and all other

trace gases are fixed at pre-industrial values.

In addition to only prescribing SST values from the $n \times \text{CO}_2$ runs, we also change the SST patterns. We use the pattern from $3 \times \text{CO}_2$ in CESM1-LE and then scale the pattern by the global-mean warming amplitude from $4 \times \text{CO}_2$ and $5 \times \text{CO}_2$. We do this by

$$\Delta\text{SST}(x, y, t) = \text{SST}_{3 \times \text{CO}_2}(x, y, t) - \text{SST}_{\text{PI}}(x, y, t),$$

t is monthly data from 150 years, x is longitude, and y is latitude. Next, we find the pattern S_p as

$$S_p(x, y, t) = \frac{\Delta\text{SST}(x, y, t)}{\overline{\Delta\text{SST}}(t)}$$

where $\overline{\Delta\text{SST}}$ is the global mean monthly data for 150 years. Then we have

$$\Delta\text{SST}'_{n \times \text{CO}_2}(x, y, t) = S_p(x, y, t) \cdot \overline{\Delta\text{SST}_{n \times \text{CO}_2}}.$$

And finally

$$\text{SST}_{n \times \text{CO}_2}(x, y, t) = \text{SST}_{\text{PI}}(x, y, t) + \Delta\text{SST}'_{n \times \text{CO}_2}(x, y, t).$$

One caveat here is that we are only changing the SSTs, and holding sea-ice fixed at $3 \times \text{CO}_2$. Although sea-ice changes also cause albedo feedback changes, Haugstad et al. 2017 find that imposing SSTs alone is sufficient to reproduce λ in the experiments.

4.2.2 Analysis

For each forcing experiment, we first estimate the long-term warming response from the Gregory method, namely, the x-intercept of regressing the change in net TOA radiation against surface air temperature over the 150 years of the simulations (Gregory et al. 2004; Zelinka et al. 2020). We then obtain EffCS for each forcing scenario by normalizing the warming response by $\log_2 n$ for the $n \times \text{CO}_2$ runs, assuming logarithmic CO₂ forcing, consistent with Bloch-Johnson et al. 2021a, even though this is not a precise assumption (Byrne

and Goldblatt 2014; Etminan et al. 2016).

We calculate individual feedbacks with radiative kernels from Pendergrass et al. 2018. For each year, we multiply the spatially resolved kernels by the climate field anomalies of atmospheric temperature T , water vapor q , and surface albedo α . We regress these quantities on the surface temperature response, and the slope of this regression is the feedback. The cloud feedbacks are computed via the residual method (Soden and Held 2006).

4.3 Results

4.3.1 Non-monotonic effective climate sensitivity and radiative feedbacks

Results from CESM1-LE show that although the global-mean surface air temperature increases monotonically as CO_2 increases (Fig. 4.1a), EffCS changes non-monotonically with CO_2 levels (Fig. 4.1b). That is, EffCS decreases between $3\times$ and $4\times\text{CO}_2$ and then increases between $4\times$ and $5\times\text{CO}_2$, and at higher CO_2 forcing, with a minimum value at $4\times\text{CO}_2$. We find the same non-monotonicity in the GISS-E2.1-G experiments except with a minimum EffCS at $3\times\text{CO}_2$ (Fig. C.1). In the rest of the paper, we will focus on the CESM1-LE simulations and note that the results hold for the GISS-E2.1-G simulations unless otherwise noted.

Changes in EffCS, in principle, are governed by changes in effective radiative forcing (ERF) and radiative feedbacks (λ). While the ERF, calculated from an additional 30-year fixed sea-surface temperature (SST) runs as per Forster et al. 2016, increases slightly more than the logarithm of the CO_2 concentration at higher CO_2 levels than $4\times\text{CO}_2$ (see Mitevski et al. 2022 for more detail), it is strongly monotonic with CO_2 and does not exhibit a minimum value (Fig. 4.1c). On the other hand, the net radiative feedback parameter λ (Fig. 4.1d), calculated from 150-year regressions of top-of-atmosphere (TOA) radiative response against surface air temperature change (Zelinka et al. 2020), exhibits a clearly non-monotonic behavior with respect to CO_2 levels, as for EffCS: λ becomes more negative (more stabilizing) between $3\times$ and $4\times\text{CO}_2$ and less negative between $4\times$ and $5\times\text{CO}_2$, corresponding

to the lowest EffCS at $4\times\text{CO}_2$. Similar results are also found in the GISS-E2.1-G model experiments (Fig. C.1). These results suggest that EffCS depends not only *nonlinearly* on CO_2 , as found in previous studies (Bloch-Johnson et al. 2021a; Caballero and Huber 2013; Meraner et al. 2013), but also *non-monotonically*, and that the non-monotonicity is caused by the radiative feedbacks in our simulations. Hence the question is: what causes the non-monotonic changes in feedbacks?

4.3.2 Non-monotonic λ traced to changes in surface warming patterns

We hypothesize two reasons for the non-monotonic changes in λ with CO_2 :

1. The non-monotonic dependence in λ may arise from a nonlinear state-dependence of the feedbacks. As noted above, previous studies have found that radiative feedbacks change nonlinearly with global-mean surface temperature changes (i.e., feedback temperature dependence), mostly owing to the cloud and water vapor feedbacks (Bloch-Johnson et al. 2021a; Caballero and Huber 2013; Meraner et al. 2013; Seeley and Jeevanjee 2021). Can the changes in global-mean surface temperature across the CO_2 levels in our simulations (Fig. 4.1a) explain the non-monotonic behavior of λ and, therefore, EffCS?
2. The non-monotonic dependence of λ may arise from a strong dependence of λ on the spatial pattern of SSTs. Recent studies have found a close coupling between SST patterns and radiative feedbacks in observations and model simulations, the so-called “pattern effect” (Dong et al. 2019; Sherwood et al. 2020; Zhou et al. 2016). If the SST pattern effect caused the non-monotonic response in λ , then what SST regions govern the global and local changes in our feedbacks?

To test the hypotheses, we run the atmospheric component of the coupled model CESM1-LE (CAM5) with specified SST boundary conditions, in order to examine the impacts of different surface warming on λ . First, we perform a set of 150-year long CAM5 simulations

where we fix all radiative forcing agents at pre-industrial levels, and prescribe the time-varying SSTs produced by the corresponding coupled model $n \times \text{CO}_2$ simulations. In these runs (denoted as “prescribed-SST”), TOA radiative fluxes and surface air temperature freely adjust to the underlying SSTs. Although not directly forced by CO_2 , we find that the prescribed-SST simulations accurately reproduce the values of λ from the corresponding coupled simulations (c.f. blue and black dots in Fig. 4.2a, error bars shown in Fig. C.2). This finding, consistent with other studies (Haugstad et al. 2017; Zhou et al. 2023), suggests that the dependence of λ on CO_2 forcing is primarily shaped by the SSTs induced by the CO_2 forcing and therefore confirms the validity of using prescribed-SST simulations to study radiative feedbacks to understand the coupled $n \times \text{CO}_2$ results.

Next, we perform another set of prescribed-SST simulations with adjusted SST boundary conditions. To test hypothesis # 1, i.e., whether λ responds non-monotonically to changes in global-mean surface temperatures, we conduct simulations where we scale the SST pattern from $3 \times \text{CO}_2$ by the actual global-mean SST changes in coupled $4 \times \text{CO}_2$ and $5 \times \text{CO}_2$, respectively. Such that these two runs have the same normalized global SST pattern (at every monthly time step) as the $3 \times \text{CO}_2$ run but different global-mean SST values (denoted “prescribed-SST with $3 \times \text{CO}_2$ pattern”). In these experiments, we find that the λ values do not reproduce those in the coupled & prescribed-SST simulations even though the same global-mean SST warming is prescribed (c.f. red and blue dots in Fig. 4.2a), suggesting that the non-monotonic response in λ arises from changes in the spatial pattern of SSTs (hypothesis # 2) and not the changes in the global-mean values of SSTs (hypothesis # 1).

The above CAM5 prescribed-SST simulations highlight the role of SST patterns in driving the non-monotonic response in λ . To understand what regions contribute to this non-monotonicity, we show the spatial pattern of λ calculated as the local net TOA radiation regressed to global-mean surface air temperature response, shown in Fig. 4.2b-d. The spatial pattern of λ in the $4 \times \text{CO}_2$ prescribed-SST run ($4 \times \text{CO}_2$ SST pattern), is shown in Fig. 4.2b, corresponding to the globally averaged λ at $4 \times \text{CO}_2$ shown by the blue dot in Fig. 4.2a. The

spatial pattern of λ in a $4\times\text{CO}_2$ run with $3\times\text{CO}_2$ SST pattern (red dot in Fig. 4.2a) is shown in Fig. 4.2c. Taking the difference between Fig. 4.2b and c (panel d) shows substantially more negative feedback in the North Atlantic with the $4\times\text{CO}_2$ pattern, and not much change when we use the $3\times\text{CO}_2$ pattern, indicating that the anomalously low EffCS at $4\times\text{CO}_2$ in our coupled simulations is primarily associated with an anomalously negative λ in the North Atlantic. We show the same λ spatial patterns for $5\times\text{CO}_2$ runs in Fig. C.3.

4.3.3 A local pattern effect from the North Atlantic

While the stronger negative feedbacks appear to be located mainly in the North Atlantic, it is unclear whether they are driven by the local North Atlantic SST changes, or by remote SST impacts from other basins. In a prior study (Lin et al. 2019) the effect of North Atlantic SSTs on λ was connected to tropospheric stability response in abrupt $4\times\text{CO}_2$ runs across CMIP models. Our present focus is on the North Atlantic SSTs influence on λ across various CO₂ levels. In Fig. 4.3, we show the normalized SST patterns from $3\times$, $4\times$, and $5\times\text{CO}_2$ simulations (panels a-c). We find that anomalous SST cooling primarily occurs in the North Atlantic: $4\times\text{CO}_2$ produces a strong cooling in the North Atlantic and less warming in the subtropical Atlantic (panel b), largely resembling the pattern of the North Atlantic Warming Hole (NAWH) (Chemke et al. 2020). However, this North Atlantic relative-cooling pattern to the global mean does not emerge at $3\times\text{CO}_2$ (panel a) and is much weaker at $5\times\text{CO}_2$ (panel c). Concurrently, we find that local feedbacks exhibit patterns that closely match the SST patterns (Fig. 4.3f,g, and h). The majority of the negative feedback strengthening, resulting in a lower EffCS, is found at $4\times$ relative to $3\times\text{CO}_2$ (Fig. 4.3i) in the North Atlantic, which aligns with the local cooling pattern (Fig. 4.3d). Conversely, most of the feedback weakening at $5\times$ relative to $4\times\text{CO}_2$ (higher EffCS, Fig. 4.3j) is also observed in the North Atlantic and corresponds with the local warming pattern (Fig. 4.3e). These results suggest that the non-monotonic response of the feedbacks found in our simulations (Fig. 4.2a) is predominately from feedback changes in the North Atlantic, associated with North Atlantic

local SST changes. We note that significant feedback changes also occur in the tropical Pacific (Fig. 4.3i,j), particularly the tropical Eastern Pacific, but these feedback changes are in the opposite sign to the global-mean feedback changes, and thus cannot account for the total feedback response we showed in Fig. 4.2a. While some other regions may contribute to the negative feedback change (e.g., the tropical Western Pacific and the Southern Ocean), we find that the North Atlantic local λ (area between 0 to 60N and 80W to 10E) explains up to 2/3 of the total change in the global-mean λ (Fig. C.4). This suggests that most of the non-monotonicity at $4\times\text{CO}_2$ is due to the North Atlantic pattern effect.

To further understand the processes causing the λ non-monotonicity, we further decompose the net feedback parameter λ into the individual feedbacks using radiative kernels (Pendergrass et al. 2018) (Fig. 4.4). In the North Atlantic at $4\times\text{CO}_2$, the Planck feedback (Fig. 4.4e) is strongly positive as the local cooling reduces outgoing radiation, whereas the combined lapse rate and water vapor feedback (Fig. 4.4h) and the cloud feedback (Fig. 4.4k) contribute negatively. The strong negative feedback at $4\times\text{CO}_2$ compared to $3\times\text{CO}_2$ in the subtropical North Atlantic is primarily due to the SW cloud feedback (Fig. C.4 and Fig. C.5h); hence, it is one of the key contributors to the λ non-monotonicity at $4\times\text{CO}_2$. Although our $4\times\text{CO}_2$ run shows little to no cooling in the tropical/subtropical North Atlantic (Fig. 4.3b), this region warms less than the tropical average due to the formation of the North Atlantic warming hole, which increases *local* low-level cloud cover (Fig. C.6a-c). This increase in low clouds coincides with an increase in the estimated inversion strength (EIS), which we find is primarily caused by local SST changes relative to the tropical average and not the upper tropospheric temperature changes (Fig. C.6). These results suggest that the anomalous subtropical SST changes between $3\times$ and $4\times\text{CO}_2$ (Fig. 4.3d), although weaker than the extratropical cooling, can efficiently change local cloud feedback and therefore global climate sensitivity. This EIS mechanism is consistent with the leading mechanism found in the tropical Pacific pattern effect (Andrews and Webb 2018; Dong et al. 2019; Zhou et al. 2016), except this pattern effect here is associated with the North Atlantic SST changes (Lin

et al. 2019), and causes the non-monotonic response in EffCS and λ across CO₂ levels in our experiments.

Additionally, it is important to note that 2/3 of the difference in feedbacks between 4×CO₂ and 3×CO₂ comes from the North Atlantic and 1/3 from the rest of the globe. At 4×CO₂, there are strong responses in the individual feedbacks in the tropical Pacific (see Fig. C.5 for albedo and longwave cloud feedbacks). However, the negative Planck feedback response in the tropical Pacific is compensated by the local positive feedback response from lapse rate, water vapor, and clouds (Fig. 4.4b,e,h,k), which makes the tropical Pacific less pronounced in the non-monotonic λ changes.

Having shown that feedback changes primarily come from the North Atlantic associated with local SST cooling, we finally return to the key pattern of North Atlantic SST cooling found in our simulations, the North Atlantic warming hole (NAWH). In the literature, the appearance of the NAWH has been attributed to the slowdown in the AMOC and linked to an atmospheric response (Caesar et al. 2018; Latif et al. 2022; Rahmstorf et al. 2015; Sévellec et al. 2017). Our previous work (Fig. B.3 in Mitevski et al. 2021) found the North Atlantic cooling (NAWH) in our experiments is primarily due to AMOC collapse. The AMOC collapses at 4×CO₂ in our GCM, and at all other higher CO₂ forcings. At higher CO₂ forcings (5×CO₂ and above), the AMOC collapse no longer produces anomalous North Atlantic cooling compared to the previous level of CO₂ forcing (e.g., 4×CO₂) because the AMOC collapse-induced SST cooling is further overwhelmed by the surrounding warming. Hence, the cooling over the NAWH is less pronounced at higher CO₂ forcings (Fig. 4.3c) and has a smaller impact on the feedbacks (Fig. 4.3h). The collapse of the AMOC under CO₂ forcing has been widely reported in climate models, including the GISS-E2.1-G model in this study (occurring at 3×CO₂ & higher) and many other CMIP5 and CMIP6 models (Fig. B.3 in Mitevski et al. 2021).

4.4 Discussion and Conclusion

In a series of $n \times \text{CO}_2$ ($n = 2, 3, 4, 5, 6, 7, 8$) experiments, we find a non-monotonic response in the effective climate sensitivity (EffCS) to CO_2 forcing using two state-of-the-art, coupled climate models. EffCS becomes anomalously low at an intermediate level of CO_2 ($4 \times \text{CO}_2$ in CESM1-LE and $3 \times \text{CO}_2$ in GISS-E2.1-G) but increases at higher CO_2 levels. This EffCS non-monotonicity is primarily linked to changes in radiative feedback λ due to tropical and subtropical North Atlantic cooling relative to the tropical mean; λ becomes anomalously negative when cooling emerges in the North Atlantic and forms a North Atlantic Warming Hole (NAWH).

The dependence of λ on sea-surface temperature (SST) patterns has been widely studied, with a focus on the time-evolution of those patterns (Andrews et al. 2022; Andrews et al. 2015; Dong et al. 2019; Sherwood et al. 2020; Zhou et al. 2016). For example, estimates of EffCS from the observed historical energy budget constraints are lower than those from long-term warming under CO_2 quadrupling, primarily owing to changes in the tropical Pacific SST patterns (Andrews et al. 2022; Andrews et al. 2018; Bloch-Johnson et al. 2023; Dong et al. 2019; Gregory et al. 2020; Zhou et al. 2016). This “pattern effect” has been studied with a Green’s function approach (Dong et al. 2019; Zhang et al. 2023; Zhou et al. 2017), which shows that the global feedback has a predominant dependence on tropical convective regions (Williams et al. 2023), and is less sensitive to the North Atlantic SSTs. This tropical Pacific SST pattern effect has been found to be a leading mechanism for the time evolution of EffCS estimates. However, our study proposes a North Atlantic pattern effect that accounts for changes in EffCS and feedbacks across different CO_2 forcing levels. This North Atlantic pattern effect shows that SST cooling (relative to the tropical mean) in the North Atlantic due to the formation of NAWH causes λ to become more negative and, therefore, lower EffCS. We note that the North Atlantic pattern effect proposed here operates on the dimension of increasing CO_2 forcing, instead of on the dimension of time evolution addressed in previous

studies (Andrews et al. 2022; Andrews and Webb 2018; Dong et al. 2019; Lin et al. 2019; Zhou et al. 2016). In particular, Lin et al. 2019 showed that the North Atlantic cooling pattern affects the evolution of λ in 150-year abrupt $4\times\text{CO}_2$ runs, whereas we have here considered how North Atlantic cooling impacts λ at different CO_2 forcing. Both findings highlight that the NAWH can influence λ depending on the timing of AMOC decline and feedback variations at other locations, and hence the NAWH is an important player in quantifying global warming.

The NAWH has been proposed to arise from the reduction of surface meridional ocean heat transport (Chemke et al. 2020) or AMOC slowdown that reduces transient warming due to increased ocean heat uptake (Caesar et al. 2020; Palter 2015; Rugenstein et al. 2013; Trossman et al. 2016; Winton et al. 2013). In our study, we find that the NAWH can further reduce EffCS and transient warming by causing more negative feedback (more efficient radiative damping at the top of the atmosphere). The fact that the NAWH has been observed in the historical period and is projected to persist in future scenarios with increasing GHG (Chemke et al. 2020; Gervais et al. 2018; Keil et al. 2020; Liu et al. 2020; Menary and Wood 2018; Ren and Liu 2021) suggests a considerable damping effect on global warming from the North Atlantic.

We further analyzed two subsets of CMIP6 models with and without NAWH in the abrupt- $4\times\text{CO}_2$ runs (Fig. C.7). Models with a NAWH in the abrupt- $4\times\text{CO}_2$ scenario also show more surface cooling in the North Atlantic in transient 21st-century simulations (under both SSP5-8.5 and SSP2-4.5 scenarios) than models without NAWH. This suggests that uncertainty in the projected long-term North Atlantic SST patterns in response to abrupt CO_2 forcing also persists in transient projections. Thus, understanding North Atlantic SST changes is crucial for constraining global climate change at both transient and equilibrium timescales.

One caveat to our findings is that the AMOC collapse in our models occurs at $3\times$ and $4\times\text{CO}_2$, which are relatively low CO_2 values, where the collapse can induce a substantial

cooling in the North Atlantic. When the AMOC collapses at a low CO₂ value, the North Atlantic cooling is strong, leading to a considerable non-monotonicity in EffCS. However, if the AMOC collapses at a higher CO₂ value, such as 5×CO₂, then the overwhelming CO₂ warming from the surrounding areas results in a weaker North Atlantic SST cooling or delayed warming pattern. In this case, the EffCS non-monotonicity would be smaller than the one reported in this study. Hence our results suggest that future changes in AMOC and NAWH may add additional uncertainty to EffCS and transient 21st century warming projections.

We also acknowledge that our results are based on only two GCMs, and that 150-year model runs are not fully equilibrated. The North Atlantic SST cooling and λ response in 150 years could be transient, as previous studies have shown that AMOC can resuscitate when models are run longer (e.g., Bonan et al. 2022; Rind et al. 2018). However, understanding AMOC changes under CO₂ forcing on centennial to millennial timescales is beyond the scope of this study. It is also important to note that the feedback dependence on CO₂ forcing we have reported here differs from the temperature dependence proposed in other studies (e.g., Bloch-Johnson et al. 2021a) because we have here shown that λ depends on the SST pattern (4×CO₂ blue vs. red dots in Fig. 4.2a) rather than the global mean surface temperature.

The fact that EffCS is nonlinear and even non-monotonic with respect to CO₂ levels complicates equilibrium climate sensitivity constraints using models, observations, the paleoclimate record, and process-based understanding. While the non-constant λ across different CO₂ levels has been mainly attributed to feedback temperature dependence within models (Bloch-Johnson et al. 2021a; Mauritsen et al. 2019; Meraner et al. 2013; Sherwood et al. 2020; Zhu and Poulsen 2020) and paleoclimate records (Anagnostou et al. 2020; Anagnostou et al. 2016; Farnsworth et al. 2019; Friedrich et al. 2016; Shaffer et al. 2016; Zhu et al. 2019), we here have shown that the SST pattern also plays a role. Our study adds additional evidence of EffCS state dependence and pattern effects, and adds to the growing body of evidence pointing to the North Atlantic as an important region for understanding climate

sensitivity and feedbacks.

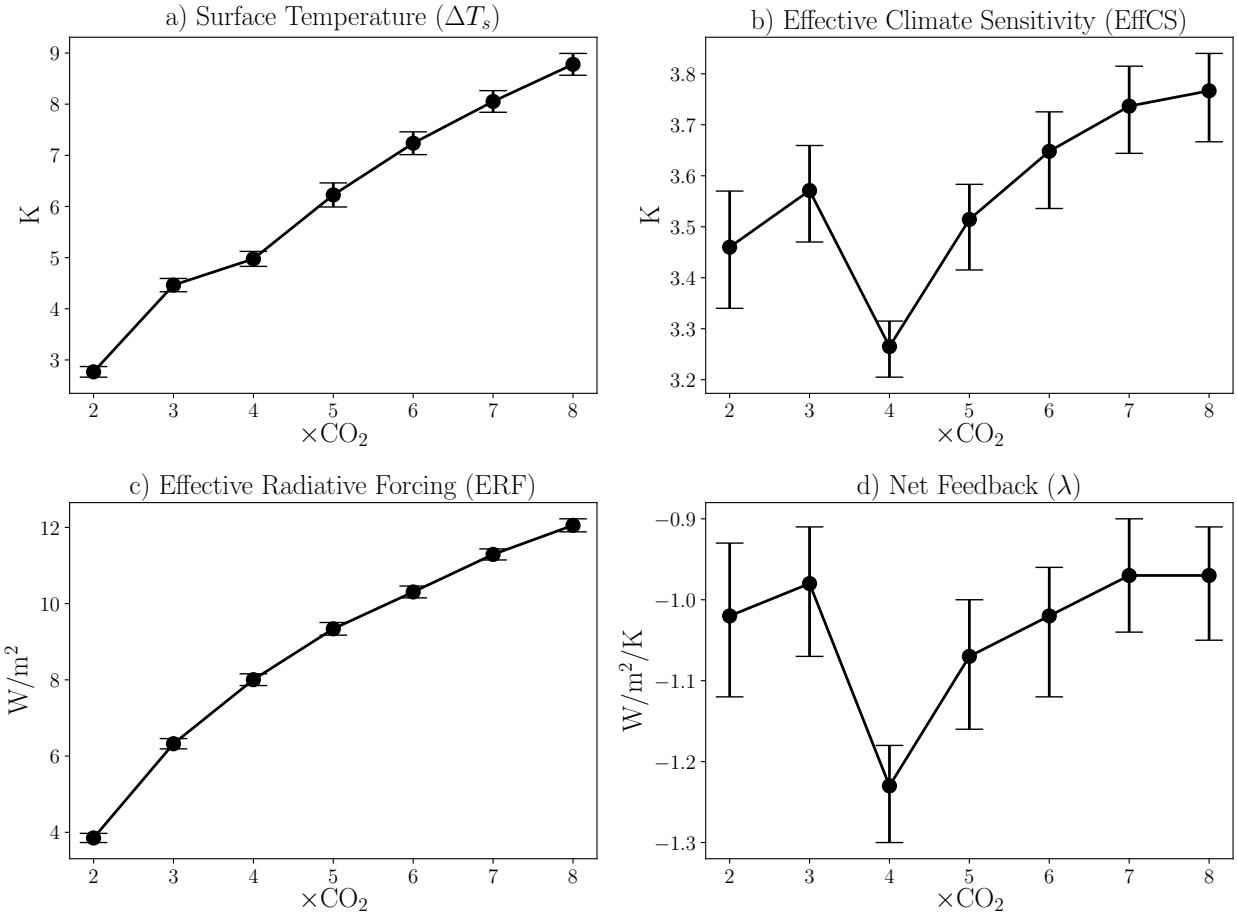


Figure 4.1: a) Global mean surface air temperature response (ΔT_s), b) effective climate sensitivity (EffCS), c) effective radiative forcing (ERF) from 30-year fixed sea-surface temperature runs, and d) net feedback parameter (λ) from the 150-year Gregory regression of abrupt $n \times \text{CO}_2$ runs. The confidence intervals for ΔT_s and ERF represent one standard deviation of the annual global mean values of the last 50 and 20 years of the runs, respectively. The confidence interval for the EffCS and λ are 95% obtained by resampling the linear regressions 10,000 times.

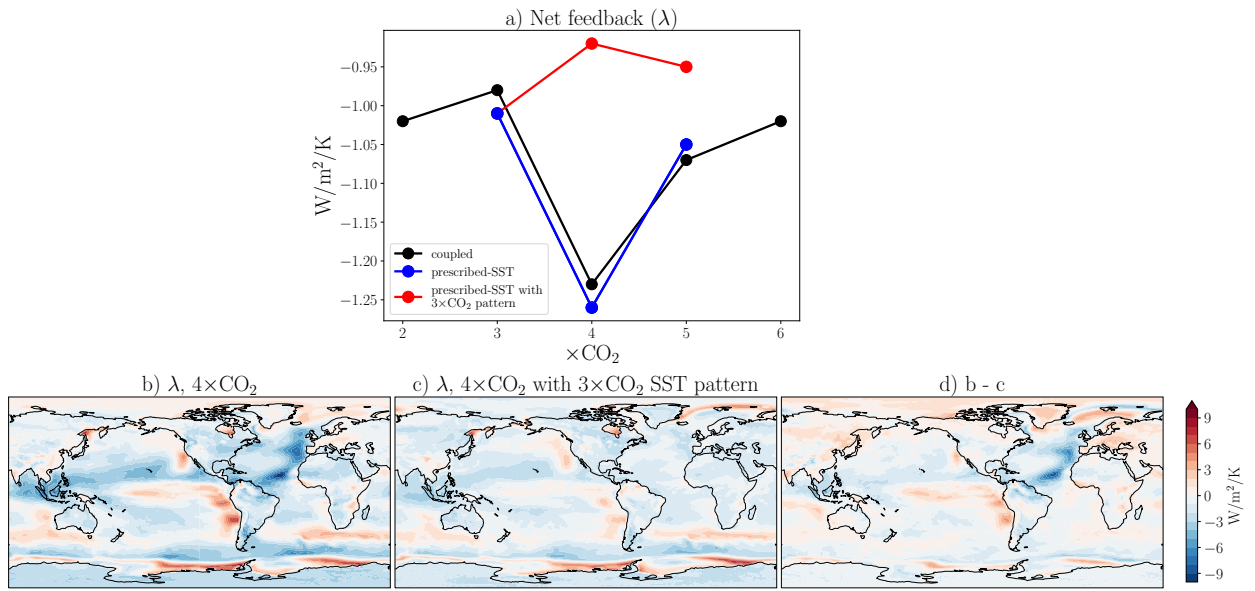


Figure 4.2: a) Global net feedback parameter λ from coupled runs, AGCM prescribed-SST runs with SSTs from coupled runs, and prescribed-SST runs with $3\times\text{CO}_2$ pattern, where the $3\times\text{CO}_2$ SST patterns are scaled with the actual global-mean SST values of $4\times\text{CO}_2$ and $5\times\text{CO}_2$, respectively. Spatial patterns of the local contribution to the global λ at $4\times\text{CO}_2$ from b) prescribed-SST, c) prescribed-SST with $3\times\text{CO}_2$ pattern and d) the difference.

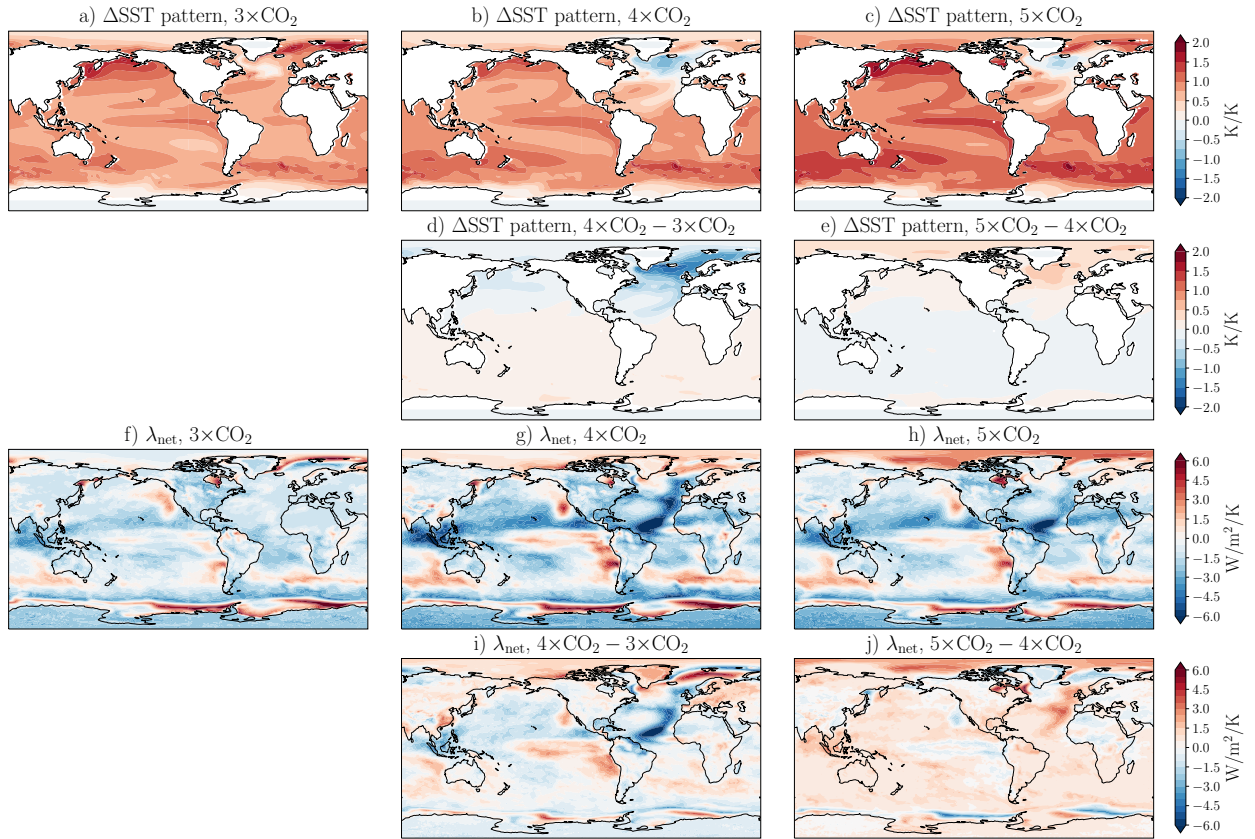


Figure 4.3: Maps of SST patterns (calculated as the regression of local temperature changes to global temperature changes for 150 years) in the coupled runs for a) $3\times\text{CO}_2$, b) $4\times\text{CO}_2$, and c) $5\times\text{CO}_2$. The differences between $4\times$ and $3\times\text{CO}_2$, and $5\times$ and $4\times\text{CO}_2$, are shown in d) and e), respectively. Figures f-j) show λ maps for the same CO_2 experiments.

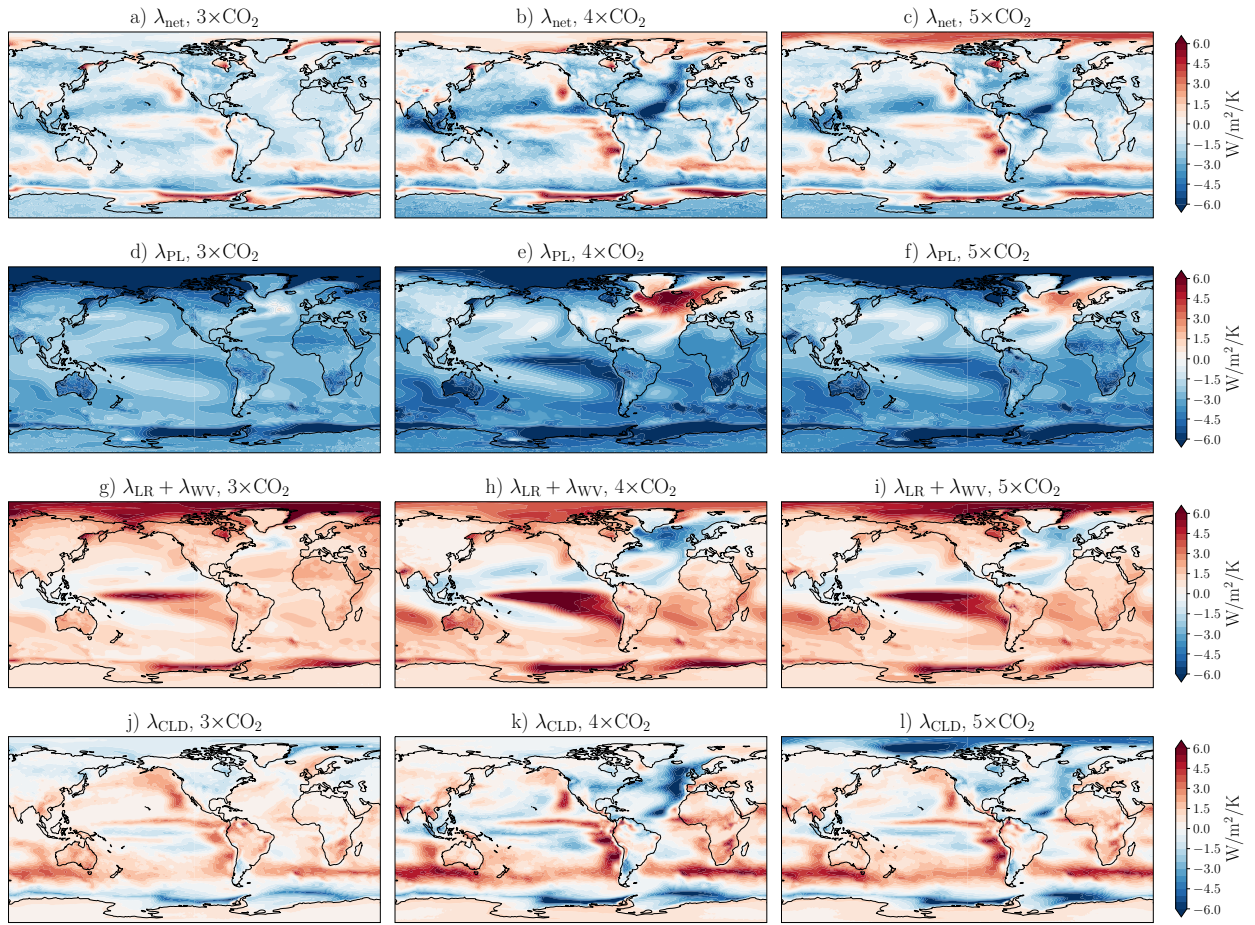


Figure 4.4: Maps of individual feedbacks calculated from prescribed-SST runs for: a-c) net, d-f) Planck, g-i) lapse rate + water vapor, j-i) net cloud.

Chapter 5: State dependence of CO₂ Effective Radiative Forcing from 1/16× to 16×CO₂

Abstract

Most research on the state dependence of climate sensitivity is focused on the radiative feedbacks with less attention on the radiative forcing. However, recent investigations have revealed that the instantaneous radiative forcing (IRF) is not solely dependent on CO₂ concentrations but also on the underlying state of the stratospheric temperature, which responds to CO₂ forcing. Hence, we here utilize atmosphere-only experiments with prescribed sea-surface temperatures using CESM1-LE, in combination with broadband radiative transfer calculations with SOCRATES, to thoroughly investigate the dependence of Effective Radiative Forcing (ERF) on varying levels of CO₂ forcing from 1/16× to 16×CO₂. We demonstrate that ERF exhibits a strong dependence on CO₂ concentrations where it doesn't simply change by the logarithm of the CO₂ concentration. Instead, the ERF increase (decrease) with CO₂ increase (decrease) exceeds the logarithmic change in CO₂ concentrations. By disentangling the ERF into IRF and radiative adjustments, we find that the IRF is primarily responsible for the CO₂ dependence of ERF. Furthermore, we find an asymmetric response of the adjustments between CO₂ increase and decrease, which we investigate through the radiative and dynamic responses within the stratosphere. A significant implication of our findings is that we should carefully consider the ERF state dependence when studying climate sensitivity under large CO₂ perturbations within the feedback-forcing framework.

5.1 Introduction

The estimation of Equilibrium climate sensitivity (ECS) plays a critical role in understanding the potential impacts of climate change. ECS is the global mean surface warming after doubling carbon dioxide (CO_2) from pre-industrial (PI) conditions. ECS has been approximated with effective climate sensitivity (EffCS), which is calculated from 150-year abrupt $4 \times \text{CO}_2$ runs and then divided by 2, assuming a logarithmic dependence on the radiative forcing with each doubling of CO_2 . EffCS is directly proportional to the radiative forcing imposed on the system, and inversely proportional to the feedback parameter λ ($\text{EffCS} = F/\lambda$).

Efforts to determine EffCS have involved various approaches, including the examination of paleoclimatic evidence (Anagnostou et al. 2020; Anagnostou et al. 2016; Farnsworth et al. 2019; Friedrich et al. 2016; Shaffer et al. 2016; Zhu et al. 2019) and modeling studies (Bloch-Johnson et al. 2021a; Mauritzen et al. 2019; Meraner et al. 2013; Mitevski et al. 2021; Sherwood et al. 2020; Zhu and Poulsen 2020). However, a major concern in estimating EffCS is the assumption that it remains constant with any CO_2 doubling, neglecting the potential for variation due to non-linear temperature dependence of radiative feedbacks caused by changes in base state and/or CO_2 perturbations (Bloch-Johnson et al. 2021a; Sherwood et al. 2015). Additionally, there have been indications of minor contributions from non-logarithmic CO_2 dependent radiative forcing (Mitevski et al. 2022).

A recent study by He et al. 2022 has provided new insights into the state dependence of ECS, highlighting not only the influence of feedback changes but also the role of the radiative forcing (F). The study revealed that the instantaneous radiative forcing (IRF), which is the majority of F , strongly depends on the climatological base state. Specifically, the IRF increases when computed from a higher CO_2 base state, and this increase is primarily related to stratospheric cooling due to CO_2 forcing. These findings align with earlier analytical work by Jeevanjee et al. 2021, emphasizing the importance of stratospheric-surface temperature

difference in determining CO₂ IRF.

Most of the attention on the state dependence of the radiative forcing has primarily centered around the IRF (He et al. 2022; Jeevanjee et al. 2021; Pincus et al. 2020), with less attention given to the state dependence of adjustments. Previous studies have predominately emphasized the IRF due to its better understanding (Mlynczak et al. 2016) and significant contribution (around two-thirds) to the effective radiative forcing (ERF). Additionally, the IRF is the primary driver of the adjustments (Forster et al. 2016; Hansen et al. 2005; Ramaswamy et al. 2018; Sherwood et al. 2015; Smith et al. 2020b; Smith et al. 2018). However, ERF, which is the sum of IRF and adjustments, is the most widely adopted definition of radiative forcing (Forster et al. 2016; Ramaswamy et al. 2018; Sherwood et al. 2015) because it has been found to be the most comprehensive measure of the radiative forcing's impact on the surface climate (Hansen et al. 2005; Richardson et al. 2019). Despite this, the state dependence of ERF in response to CO₂ forcing has yet to be explored in the literature.

Our previous study (Mitevski et al. 2022) demonstrated that ERF exhibits asymmetry across CO₂ doublings and halvings, leading to asymmetric surface temperature responses. Moreover, we observed that the ERF increases slightly more than the logarithm of CO₂ concentration. While previous ECS studies have demonstrated an increase in ERF with CO₂ concentration (Colman and McAvaney 2009; Hansen et al. 2005), the underlying mechanisms behind this ERF increase, and its decomposition into IRF and adjustments, have not been thoroughly explored. How much the state dependence of ERF contributes to the state dependence of EffCS, and the underlying mechanisms driving this relationship, remains an open question. To address this question, we conduct simulations using the CESM1-LE model, calculating ERF from atmosphere-only experiments with prescribed sea-surface temperatures and sea ice starting from different CO₂ states. By separately quantifying the IRF and adjustments, we aim to elucidate the mechanisms behind ERF state dependence. Specifically, we investigate whether changes in stratospheric temperature affect ERF and the adjustments, and what factors drive ERF to increase more than the logarithm of the CO₂

concentration.

5.2 Methods

Our study utilizes the original large ensemble version of the Community Earth System Model (CESM1-LE) (Kay et al. 2015). This model consists of the Community Atmosphere Model version 5 (CAM5) with prescribed pre-industrial (PI) sea-surface temperatures (SSTs) and sea ice (SIC). The model components have a horizontal resolution of approximately 1°. Additionally, we incorporate some results from the GISS-E2.1-G model (Kelley et al. 2020). To estimate the Instantaneous Radiative Forcing (IRF), we employ the broadband model SOCRATES (Edwards and Slingo 1996; Manners 2015).

We conduct step experiments using the CESM1-LE model with PI SSTs and SIC, referred to as “prescribed-SST” runs, to examine the effects of abrupt CO₂ doublings and halvings. For the doubling experiments, we start from PI conditions and, every ten years, abruptly double the CO₂ concentration up to 16×CO₂ (indicated in red in Fig. 5.1a). The halving experiments follow the same approach, starting from PI conditions and reducing the CO₂ concentration by half every ten years until 1/16×CO₂ (indicated in blue in Fig. 5.1a). The effective radiative forcing (ERF) is then calculated as the global mean net top of the atmosphere (TOA) radiation between two adjacent CO₂ steps, which includes stratospheric and tropospheric adjustments (Sherwood et al. 2015). While the SSTs and SICs are fixed to PI values, the land temperature is allowed to evolve because prescribing land surface conditions in a climate model poses technical difficulties (Ackerley et al. 2018; Andrews et al. 2021; Hansen et al. 2005). The land warms and cools when CO₂ increases and decreases, respectively. This surface temperature response introduces a radiative effect and some adjustments which are an important caveat in calculating the ERF (Andrews et al. 2021). To correct for this surface temperature response over land, we calculate the surface temperature adjustment A_{Ts} by multiplying the surface temperature kernel with surface temperature and subtracting it from the ERF ($ERF_{ts} = ERF - A_{Ts}$), following the approach in Smith et al.

2020b.

To calculate the IRF, we employ two different approaches. First, we estimate the all-sky longwave part of the IRF using offline radiative transfer calculations with the SOCRATES broadband model (Edwards and Slingo 1996; Manners 2015). In these calculations, we use the perturbed atmospheric state from each CO₂ level, ranging from 1/16× to 16×CO₂, and doubled the CO₂ concentration to find the IRF. Therefore, the IRF in this context incorporates the base state change and differs from the traditional definition of IRF, which represents the instantaneous change in radiative flux caused by the introduction of CO₂ (Andrews et al. 2021).

Second, we estimate IRF as a residual by subtracting the adjustments from the ERF. Following the approach of Smith et al. 2018 and Chung and Soden 2015, we express the ERF resulting from a climate perturbation as a sum of IRF and various rapid adjustments:

$$\text{ERF} = \text{IRF} + A_T + A_{T_s} + A_q + A_\alpha + A_c$$

where A_x are the rapid adjustments where x is atmospheric temperature T , surface temperature T_s , specific humidity q , surface albedo α , and clouds c . We further separate the rapid adjustments into stratospheric and tropospheric contributions using a tropopause that varies linearly from 100 hPa at the equator to 300hPa at the poles. The radiative kernel K_x approximates the change in TOA shortwave or longwave radiation ΔR resulting from a unit change in the state variable Δx , such that $K_x \approx \partial R / \partial x$ and $A_x = K_x \Delta x$. The cloud kernels A_c are determined following the method of Chung and Soden 2015 by computing the difference between all-sky and clear-sky kernel decomposition. The radiative kernels are calculated by making small perturbations in the model's base climatology and running the resulting atmosphere through an offline radiative transfer code. TOA fluxes are then compared between the perturbed and base states. As the stratospheric adjustments have been shown to depend on the choice of kernel (Smith et al. 2020b), we perform the adjust-

ment calculations using ten kernels from the following models: GFDL (Soden et al. 2008), BMRC (Soden et al. 2008), CAM5 (Pendergrass et al. 2018), ERAi (Huang et al. 2017), HadGEM3-GA7.1 (Smith et al. 2020b), HadGEM3, CCSM4 (Shell et al. 2008), ECHAM5 (Previdi 2010), HadGEM2 (Smith et al. 2018), and ECHAM6 (Block and Mauritsen 2013).

5.3 Results

Fig. 5.1a shows the step experiments with CESM1-LE where CO_2 is increased from PI to $16 \times \text{CO}_2$ values in 10-year steps (red), and similarly decreased to $1/16 \times \text{CO}_2$ (blue). We calculate the resulting ERF as the difference between two consecutive CO_2 steps. While a logarithmic relationship would imply equal ERF for each step, we observe that the “blue step” at year -40 is smaller than the “red step” at year 40. Fig. 5.1b displays the calculated ERF from each step adjusted for land warming, revealing that the ERF does not remain constant but increases more than the logarithm of the CO_2 concentration, with ERF around 3Wm^{-2} at $1/16 \times \text{CO}_2$ and 4.5Wm^{-2} at $16 \times \text{CO}_2$. We will explain in the next figures why ERF decreases from $1/16$ to $1/2 \times \text{CO}_2$.

In our previous work (Mitevski et al. 2021; Mitevski et al. 2022), we calculated the ERF from abrupt $n \times \text{CO}_2$ runs (from $1/8 \times$ to $8 \times \text{CO}_2$) as the net TOA radiation between the $n \times \text{CO}_2$ states and PI, as shown in Fig. 5.1c. The ERF calculated this way with the CESM1-LE model (Fig. 5.1d) also exhibited an increase that surpassed the logarithmic relationship with CO_2 concentration. Specifically, the ERF increased from 3Wm^{-2} at $1/8 \times \text{CO}_2$ to 4.2Wm^{-2} at $8 \times \text{CO}_2$. Notably, these experiments differ from the 10-year step experiments in Figs. 5.1a,b in that they always started from the PI atmospheric state yet yielded similar ERF increases with CO_2 . We obtained similar results with increasing and decreasing CO_2 by $1\%\text{yr}^{-1}$ (1pctCO₂ runs) with CESM1-LE, and abrupt $n \times \text{CO}_2$ runs with the GISS model (Fig. 5.1d). The ERF increase exceeded both the logarithmic relationship and the simplified expressions proposed in (Byrne and Goldblatt 2014; Etminan et al. 2016) (see Fig. 2.2 in Mitevski et al. 2022). By conducting abrupt $n \times \text{CO}_2$, 10-year abrupt step, and 1pctCO₂ ex-

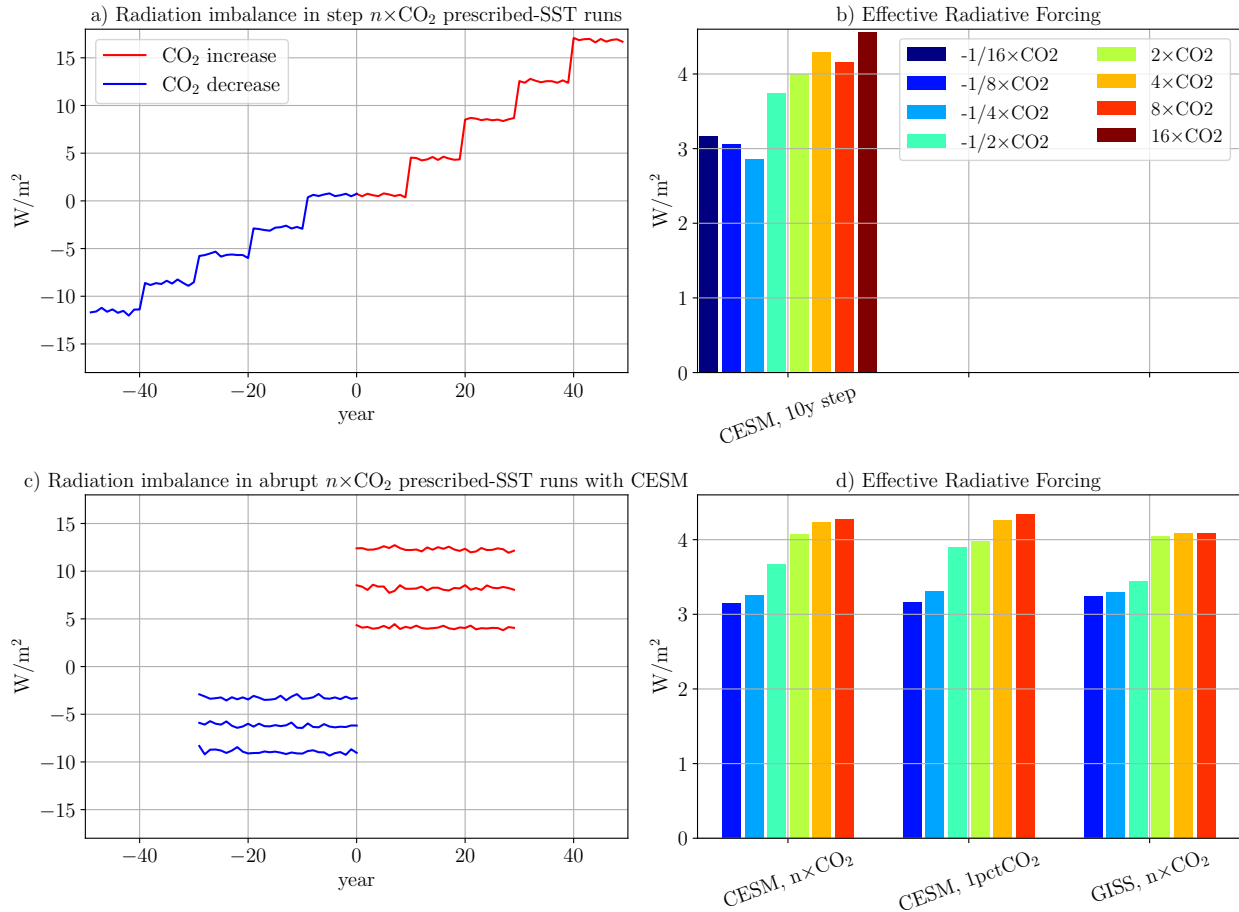


Figure 5.1: a) The radiative imbalance at the top of the atmosphere in the 10-year step experiments, where CO_2 is doubled (red) or halved (blue) starting from the pre-industrial (PI) condition. b) The Effective Radiative Forcing (ERF), calculated as the difference between two levels shown in panel a and adjusted for land warming (see methods). c) The radiative imbalance at the top of the atmosphere in the $n \times \text{CO}_2$ prescribed-SST runs, starting from the PI CO_2 concentration. d) Normalized ERF (divided by $\log_2 n$) obtained from the abrupt- $n \times \text{CO}_2$ run with CESM1-LE (left), 1pctCO₂ runs with CESM1-LE (middle), and abrupt- $n \times \text{CO}_2$ runs with the GISS-E2.1-G model, with adjustments made for land warming (see methods in (Mitevski et al. 2022)).

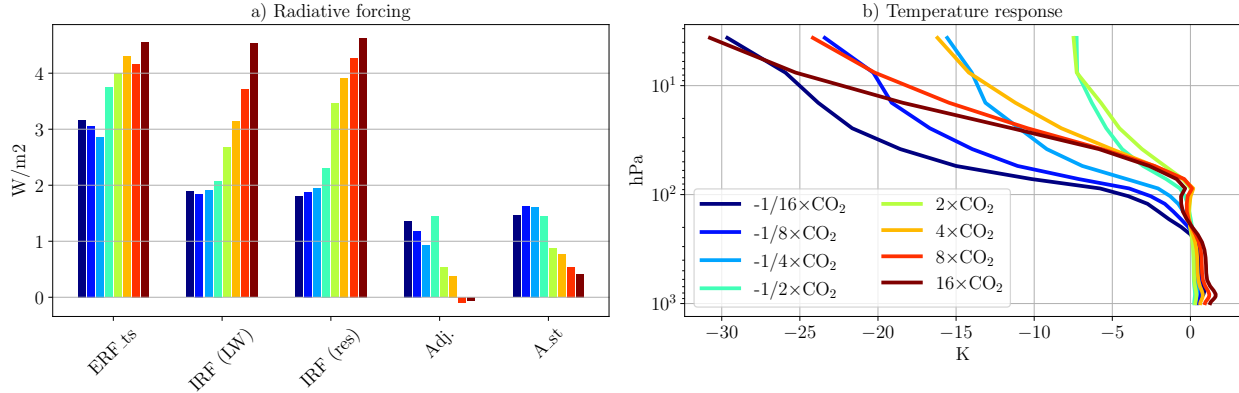


Figure 5.2: a) ERF decomposition into longwave IRF calculated from SOCRATES, IRF calculated as a residual from the adjustments, total adjustments (Adj.), and stratospheric adjustments (A_st). The global mean temperature response profile from the runs in a). All values for the CO₂ decrease runs are multiplied by -1 for better comparison with the CO₂ increase values.

periments, we demonstrate that the ERF increase with CO₂ concentration is independent of the method used to perturb CO₂ in the prescribed-SST runs. Furthermore, including GISS model results confirms that the ERF increase is not specific to a particular model. Lastly, our findings indicate that the ERF increases with CO₂ irrespective of whether we start from the PI or the $n \times$ CO₂ atmospheric state.

In Fig. 5.2a, we decompose the ERF into IRF and adjustments. Firstly, we compute the longwave component of IRF using SOCRATES, considering the base atmospheric state for each of the $n \times$ CO₂ runs (depicted by the second set of bars in Fig. 5.2a). The longwave IRF also increases with the CO₂ concentration, particularly from 2 \times to 16 \times CO₂, surpassing the increase from 1/16 \times to 1/2 \times CO₂. The shortwave component of IRF represents less than 5% of the total IRF; thus, we solely focus on the changes in the longwave component when performing radiative calculations with SOCRATES (Pincus et al. 2020; Shine et al. 2022). Alternatively, we compute the IRF as the residual obtained after subtracting the total adjustments from the ERF using kernels, denoted as IRF (res). The IRF (res) exhibits similar behavior to IRF (LW) in the 10-year step runs, displaying a comparable direction of change with CO₂. Therefore, the observed non-logarithmic increase in ERF coincides

with an increase in IRF. Note, however, that the IRF exhibits a greater increase with CO₂ compared to the ERF. This is because its rise is counteracted by the adjustments shown in Fig. 5.2a. These adjustments are larger in the CO₂ decrease scenarios compared to CO₂ increase. The adjustments oppose the increase in IRF, resulting in a smaller increase in ERF relative to IRF. The adjustments decrease with CO₂ primarily due to the asymmetry in the stratospheric adjustment (A_{st}, depicted in the last set of columns in Fig. 5.2a), which arises from the asymmetric stratospheric temperature response between comparable CO₂ increase and decrease scenarios as illustrated in Fig. 5.2b. Specifically, near the peak emission (around 10-15hPa), the scenarios involving a decrease in CO₂ exhibit a stronger stratospheric temperature response (warming) compared to the scenarios involving an increase in CO₂ (cooling) across all cases (keep in mind that we reverse the sign of the temperature adjustment for the CO₂ decrease runs). Consequently, the stratospheric temperature adjustments are larger in the CO₂ decrease cases. Furthermore, the decrease in ERF between $1/16\times$ and $1/4\times\text{CO}_2$ is attributed to the diminishing total adjustments, while the IRF remains relatively unchanged.

In order to gain further insights into the asymmetry in the stratospheric temperature response, we examine the zonal mean temperature patterns in our experiments in Fig. 5.3. As expected, the scenarios involving a decrease in CO₂ (Figs. 5.3a,d,g,j) exhibit stratospheric warming, while the scenarios involving an increase in CO₂ (Figs. 5.3b,e,h,k) display stratospheric cooling. It is well-established in the literature that the addition of CO₂ leads to surface and tropospheric warming but induces stratospheric cooling (Goessling and Bathiany 2016). Conversely, the opposite occurs when CO₂ is removed: the surface and troposphere cool while the stratosphere warms. Interestingly, we find that the magnitude of stratospheric warming in the CO₂ decrease scenarios ($1/2\times$, $1/4\times$, $1/8\times$, $1/16\times\text{CO}_2$) is greater than the magnitude of stratospheric cooling in the corresponding CO₂ increase experiments ($2\times$, $4\times$, $8\times$, and $16\times\text{CO}_2$) (depicted in red in Figs. 5.3c,f,i,l). This asymmetry in the stratospheric temperature response is primarily observed between 10 and 100hPa, from 50 degrees south to the Arctic.

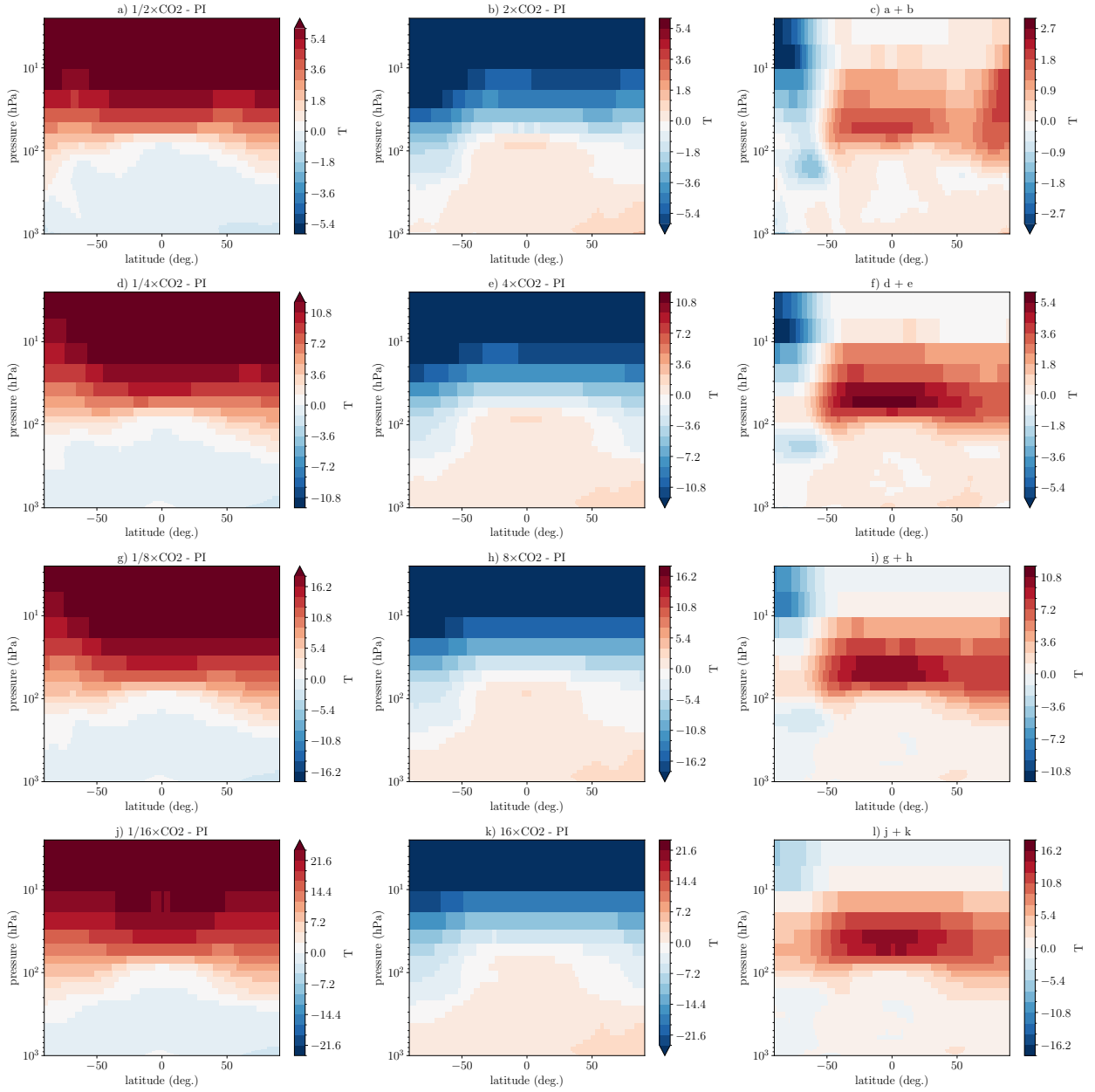


Figure 5.3: Zonal temperature response and asymmetry between $1/2$ and $2\times\text{CO}_2$ (a,b,c), $1/4$ and $4\times\text{CO}_2$ (d,e,f), $1/8$ and $8\times\text{CO}_2$ (g,h,i), and $1/16$ and $16\times\text{CO}_2$ (j,k,l).

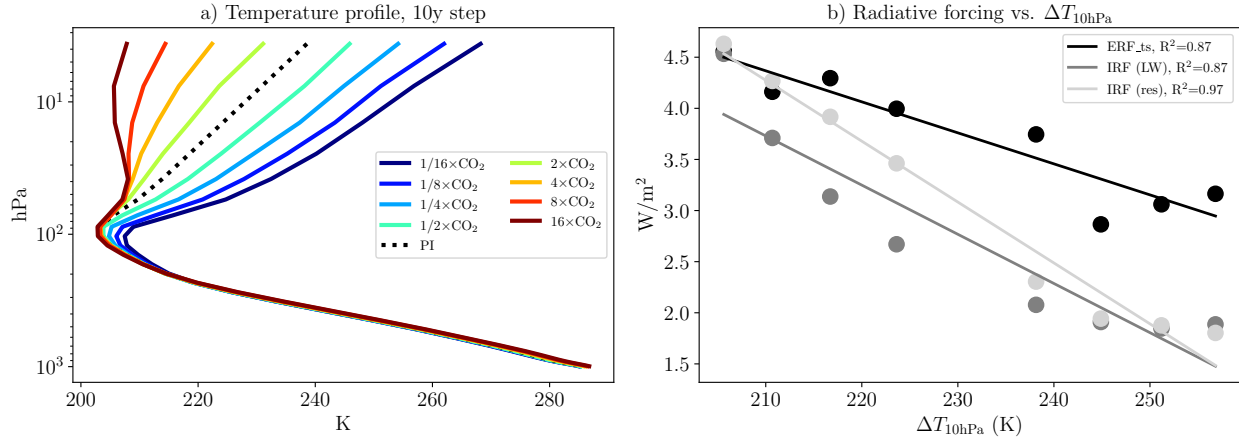


Figure 5.4: Global mean temperature profiles of a) 10-year step and b) abrupt- $n \times \text{CO}_2$ experiments.

Previous work (Jeevanjee et al. 2021) has shown that the influence of emission temperatures in the troposphere and stratosphere can explain the CO₂ dependence of IRF. Specifically, a decrease in stratospheric temperature is expected to correspond to an increase in IRF. To examine this relationship, we show in Fig. 5.4b a strong correlation between the stratospheric temperature at 10hPa ($\Delta T_{10\text{hPa}}$) and ERF. Notably, as the stratospheric temperature cools (Fig. 5.4a), the ERF exhibits an increase. Additionally, the longwave and residual IRF show similar correlations with $\Delta T_{10\text{hPa}}$, aligning with their concurrent increase with CO₂ and ERF. Therefore, the rise in IRF associated with $\Delta T_{10\text{hPa}}$ accounts for the observed increase in ERF, establishing a direct link between the stratospheric temperature state and the ERF.

It is important to note that the IRF calculations in this context are performed using the perturbed state, which incorporates the rapid adjustments resulting from temperature, humidity, albedo, and cloud changes. Hence, we can only quantify the base state (mostly stratospheric temperature) dependence of IRF, and not the CO₂ dependence. To quantify solely the CO₂ dependence, we would need to use the same PI base state and only change CO₂. He et al. 2022 investigated the influence of CO₂ concentration on IRF by conducting SOCRATES simulations with the same atmospheric base state while only modifying the

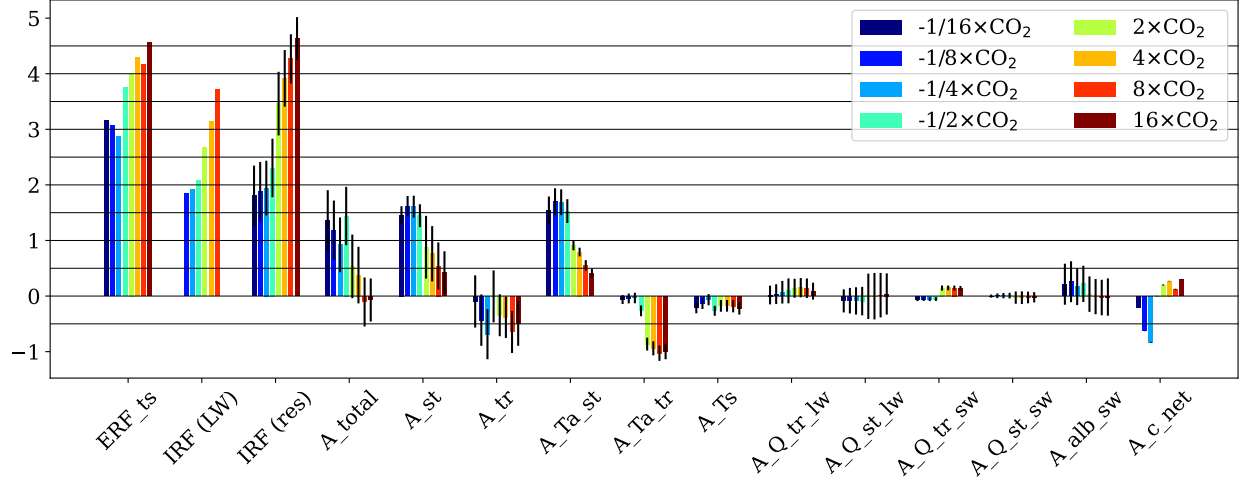


Figure 5.5: ERF decomposition into IRF, total (A_{total}), stratospheric (A_{st}), tropospheric (A_{tr}), stratospheric temperature ($A_{\text{Ta_st}}$), tropospheric temperature ($A_{\text{Ta_tr}}$), surface temperature (A_{Ts}), longwave tropospheric water vapor ($A_{\text{Q_tr_lw}}$), longwave stratospheric water vapor ($A_{\text{Q_st_lw}}$), shortwave tropospheric water vapor ($A_{\text{Q_tr_sw}}$), shortwave stratospheric water vapor ($A_{\text{Q_st_sw}}$), shortwave albedo ($A_{\text{alb_sw}}$), and net cloud ($A_{\text{c_net}}$) adjustment. The vertical lines show one standard deviation of the ten kernels, and the bars show the mean.

CO₂ concentration to 4×CO₂. Their findings revealed a relatively small dependence on CO₂ alone, indicating that if IRF is calculated using the traditionally defined base state, there would be no noticeable CO₂ dependence. However, the alteration in the atmospheric state, primarily characterized by stratospheric cooling, leads to an increase in IRF (and consequently ERF) with varying CO₂ concentrations. Further investigation is needed to quantify the contribution of IRF state dependence resulting from changes in stratospheric temperature and CO₂ forcing.

Finally, we present the decomposition of ERF into IRF and individual adjustments in Fig. 5.5. Consistent with our previous discussions, the IRF accounts for the ERF increase from 1/16× to 16×CO₂, while the total adjustment (A_{total}) acts to decrease it. The majority of changes in the total adjustments between 1/16× and 16×CO₂ stem from stratospheric adjustments (A_{st}), while the tropospheric adjustments (A_{tr}) predominantly exhibit negative values and do not contribute significantly to the overall trend. Within the stratospheric adjustments, the temperature response ($A_{\text{Ta_st}}$) is the primary driver, with minimal con-

tributions from stratospheric water vapor in the longwave and shortwave ($A_Q_st_lw$ and $A_Q_st_sw$). Regarding the tropospheric adjustments, the most notable contributor to the overall increasing trend in ERF is the cloud contribution (A_c_net); however, the tropospheric temperature trend (A_Ta_tr) opposes it.

The stratospheric adjustments exhibit a decreasing trend with higher CO_2 values, which is confirmed by the temperature profile differences between each consecutive CO_2 value (not shown), where the temperature response between $1/16 \times \text{CO}_2$ and $1/8 \times \text{CO}_2$ is stronger than the response between pre-industrial (PI) and $2 \times \text{CO}_2$, and this, in turn, is stronger than the response between $8 \times$ and $16 \times \text{CO}_2$. This suggests a state dependence of the stratospheric temperature response, indicating that as the CO_2 value increases, the stratospheric temperature response diminishes with each CO_2 doubling. Investigating this decrease in stratospheric temperature response would involve exploring the radiative and dynamical aspects. From a radiative perspective, it is worth investigating whether there is an expected decrease in stratospheric cooling according to Planck's function as we reach higher CO_2 values. On the other hand, from a dynamical standpoint, since we are keeping the atmospheric composition fixed (e.g., ozone), one potential factor that could contribute to this difference in stratospheric temperature response is the Brewer-Dobson Circulation. In future work, it would be valuable to further explore whether the dynamical or radiative components drive this asymmetry.

5.4 Discussion and Conclusion

In this study, we investigated the state dependence of the effective radiative forcing (ERF) using CESM1-LE, ranging from $1/16 \times$ to $16 \times \text{CO}_2$, and found that the ERF increases from around 3Wm^{-2} to 4.5Wm^{-2} , respectively. We attributed this ERF increase to the increase in instantaneous radiative forcing (IRF), which we calculated with broadband calculations with SOCRATES and as a residual from the radiative adjustments. We further attributed the increase in IRF to the cooling of the stratospheric temperatures as CO_2 concentrations

increase. Additionally, we found an asymmetric stratospheric temperature adjustment between comparable CO₂ warming ($n \times \text{CO}_2$) and cooling ($1/n \times \text{CO}_2$) because the stratosphere warms more in $1/n \times \text{CO}_2$ than it cools in $n \times \text{CO}_2$ runs. The majority of the asymmetric temperature response between cooling and warming occurred in the lower stratosphere, and future work will focus on elucidating the causes and implications of this asymmetry.

Our findings have important implications regarding the ozone response to CO₂ forcing in interactive chemistry models, as it can influence stratospheric temperature and, consequently, radiative forcing, which in turn affects surface warming. Previous studies have investigated the impact of ozone on effective climate sensitivity (EffCS), and radiative forcing, but the results have been mixed. Some studies have reported EffCS changes ranging from up to 20% (Nowack et al. 2015) to around 8% (Dietmüller et al. 2014; Muthers et al. 2014), while others have found no significant impact (Marsh et al. 2016). The role of interactive chemistry in the Last Glacial Maximum has also been explored, showing a similar range of results with surface temperature responses ranging from -20% (Noda et al. 2018) to around 3% (Zhu et al. 2022). However, most of these studies have primarily focused on the overall dynamics and chemistry response in the stratosphere without specifically isolating the influence of ozone on stratospheric temperature and its subsequent effect on radiative forcing. To better understand the effect of stratospheric temperature on CO₂'s radiative forcing and surface climate, it is crucial to conduct more detailed investigations that quantify this impact and differentiate it from other components of the stratospheric dynamics and chemistry response to CO₂.

It is important to acknowledge that our adjustment calculations are subject to uncertainties arising from the choice of kernel base state, kernel model top, and kernel perturbation. Pincus et al. 2020 demonstrated that radiative transfer calculations across different line-by-line (LBL) models yield consistent results when considering the same base state. Therefore, the base state is the primary source of uncertainty among LBL models, and this base state dependence is also critical for kernel calculations. By performing calculations with ten dif-

ferent kernels, we attempt to estimate this uncertainty. Secondly, the uncertainty associated with kernels is also influenced by the model top, as described in Smith et al. 2020a. Variations in stratospheric adjustments derived from kernels can exhibit nearly a twofold difference, as depicted in Fig. 5 of Smith et al. 2020a. Thirdly, the kernel method relies on the assumption of linearity between top-of-atmosphere (TOA) radiative fluxes and atmospheric variables. However, this linearity assumption is limited to small climate perturbations and may break down under higher forcing scenarios (e.g., $8\times\text{CO}_2$), as shown in studies by Jonko et al. 2012; Jonko et al. 2013. Furthermore, we were unable to find verification of the kernel technique for very low CO₂ values such as $1/16\times\text{CO}_2$. Hence, these limitations should be considered when utilizing kernels to quantify adjustments in our work.

Another limitation of our IRF calculations using SOCRATES is that we performed them at the base state corresponding to $n\times\text{CO}_2$. As a result, the non-log behavior of IRF is solely attributed to the changes in atmospheric state, predominantly stratospheric cooling, at $n\times\text{CO}_2$. By doubling the CO₂ concentration from each base state, we did not specifically investigate the extent to which IRF depends solely on CO₂ forcing. To shed light on this aspect, He et al. 2022 (their Fig. S1) and Pincus et al. 2020 conducted experiments by perturbing the PI base state with $0.5\times\text{CO}_2$, $2\times\text{CO}_2$, and $4\times\text{CO}_2$ concentrations and they discovered that the change in IRF was less than 0.1 W/m^2 , which is relatively small compared to the increase observed when altering the atmospheric state (Fig. 5.2a). Therefore, in future work, it will be important to separate and quantify how much of the IRF increase with CO₂ comes from the change in base state compared to CO₂ increase. This can be achieved by using SOCRATES to calculate IRF at the PI base state and selectively modifying a single atmospheric variable (such as temperature, humidity, albedo, and cloud properties) in the perturbed state, enabling accurate calculations of the corresponding adjustments. Furthermore, to enhance the accuracy of quantifying IRF and adjustments, we should utilize the parallel offline radiative transfer model (PORT) (Conley et al. 2013) from CESM1-LE, as it allows for precise calculations of IRF and its associated adjustments.

A third limitation of our experiments is the absence of fixed land temperatures, which introduces a significant caveat. Land warming has the potential to induce feedback and influence atmospheric circulation, which, in turn, can impact cloud adjustment. To address this issue, we can incorporate either the surface temperature adjustments calculated from kernels, as demonstrated in this work, or consider the global radiative feedback. It is important to examine these factors to ensure that the spatial distribution of radiative forcing and land adjustments does not significantly affect the ERF. Finally, it is crucial to acknowledge that our results, obtained from the 10-year step experiments with prescribed SSTs, are based on a single climate model. To enhance the robustness of our findings, we should repeat these experiments using other climate models.

Our findings highlight that the Effective Radiative Forcing exhibits a non-logarithmic change with increasing CO₂ concentrations. This underscores the importance of carefully considering radiative forcing when studying the climate system under large CO₂ perturbations within the feedback-forcing framework. Furthermore, our results demonstrate that the radiative adjustments vary across different CO₂ forcings. Thus, it is crucial not only to calculate IRF using line-by-line models but also to incorporate the adjustments when determining ERF.

Chapter 6: Southern Hemisphere Winter Storm Tracks Respond Differently to Low and High CO₂ Forcings

Abstract

In the Southern Hemisphere, Earth system models project an intensification of winter storm tracks by the end of the 21st century. However, it is unknown whether such an intensification will continue with increasing greenhouse gases. Previous studies using idealized models showed a non-linear behavior of storm track intensity with increasing temperatures. Thus, here we examine the response of mid-latitude winter storm tracks in the Southern Hemisphere to increasing CO₂ concentrations, up to eight times the preindustrial CO₂ levels. We find that at high CO₂ levels (i.e., 5×CO₂), winter storm tracks no longer exhibit an intensification across the extratropics, as predicted by the end of this century. Instead, winter storm tracks shift poleward, similar to the projected response of summer storm tracks, including a reduction of the storm tracks at low-mid latitudes and intensification at mid-high latitudes. By analyzing the eddy kinetic energy (EKE) budget, the non-linear storm track response to an increase in CO₂ levels is found to stem from a scale dependent conversion of eddy available potential energy to EKE at low mid-latitudes. Specifically, while at low CO₂ levels, this energy conversion increases the EKE of large scales, at high CO₂ levels, it reduces the EKE of small scales, resulting in the poleward shift of the storms. Our results suggest that in the next century, the storms' response might differ from the response projected by 2100, not only in magnitude but in their latitudinal distribution.

6.1 Introduction

Extratropical storm tracks transport heat, momentum, and moisture, and thereby directly influence the general circulation of the atmosphere (Harvey et al. 2014; Schwierz et al. 2010). These storm tracks play a significant role in shaping regional weather and climate by impacting the variability of precipitation, temperature, and winds in the extratropical regions (Chang et al. 2022; Pfahl and Wernli 2012; Yau and Chang 2020). Given their dominance in weather variability, any future alterations in storm tracks resulting from increased greenhouse gas (GHG) emissions will have consequential effects on regional climate. Therefore, understanding how storm tracks will change in a warmer world becomes a critically important question to address.

The extratropical storm tracks consist of transient eddies which extract their energy from the mean available potential energy (MAPE) via the process of baroclinic instability (Lorenz 1955; O’Gorman 2010). Since MAPE depends on both the horizontal (meridional) and vertical (static stability) temperature gradients (Lorenz 1955; Peixóto and Oort 1974), changes in the temperature gradients in a warmer climate will directly impact the storm tracks. In a warmer climate, the upper tropical troposphere is projected to warm more than the upper polar troposphere, leading to a stronger upper meridional temperature gradient. Conversely, near the surface, polar regions are anticipated to warm more than the tropics, decreasing the lower meridional temperature gradient.

According to the IPCC Sixth Assessment Report (AR6) (IPCC 2021), there has been a noticeable poleward shift of the annual mid-latitude storm tracks in both hemispheres since the 1970s. In the Northern Hemisphere, there is low confidence in this poleward shift due to substantial internal variability and structural uncertainty in model simulations. In the Southern Hemisphere (SH), there is high confidence in the observed poleward shift of storm tracks, particularly during the seasons of December to February and September to November. It is important to highlight that the observed poleward shift in the SH storm tracks can be

attributed to both the increase in greenhouse gases (GHGs) and to ozone depletion (Bender et al. 2012; Fyfe 2003; Grise et al. 2014). Ozone depletion, which results in cooling in mid-high latitudes (Randel and Wu 1999), strengthens the meridional temperature gradient and, consequently, the baroclinicity. However, the ozone hole is expected to recover by the end of the 21st century, potentially counteracting the poleward shift of storm tracks (Banerjee et al. 2020; Barnes et al. 2014). Nevertheless, the ongoing increase in GHGs will likely continue contributing to the poleward shift of storm tracks in both hemispheres.

Numerous Earth system model studies have extensively explored the future response of storm tracks to increased greenhouse gas (GHG) concentrations (Chang et al. 2012; Harvey et al. 2020; Harvey et al. 2014; Lehmann et al. 2014; Yin 2005; Zappa et al. 2013). In the Northern Hemisphere, these studies suggest a weakening of summer (JJA) storm tracks, while winter (DJF) storm tracks are expected to strengthen by the end of the 21st century only over the North Atlantic / Western Europe. In the Southern Hemisphere, summer (DJF) storm tracks are projected to shift poleward, while winter (JJA) storm tracks are anticipated to intensify. Some of these storm tracks responses have already been observed in recent decades, including the shift in SH summer (Bender et al. 2012; Fyfe 2003), the intensification in SH winter (Chemke et al. 2022a), and the weakening in NH summer (Chang et al. 2016; Coumou et al. 2015). It is important to acknowledge that most previous work has primarily focused on the future storm tracks response under scenarios involving CO₂-quadrupling by the end of this century (e.g., RCP8.5, SSP5-8.5). Yet, without any mitigation policy, the CO₂ concentrations are expected to continue and increase beyond 2100. For example, the highest emission socio-economic pathways scenario (SSP5-8.5) projects a transient increase in greenhouse gas forcing up to 8×CO₂, relative to PI values, by the year 2250 (Meinshausen et al. 2020). Therefore, a more comprehensive understanding of the storm track response at intermediate CO₂ levels above 4×CO₂ is essential.

Furthermore, previous idealized studies (e.g., O’Gorman and Schneider 2008a) have revealed a non-linear behavior of storm tracks in relation to global mean warming. Specif-

ically, these studies demonstrated that the EKE exhibits a maximum at current surface temperatures and decreases under both warmer and colder surface temperature conditions. Considering that other studies have indicated the potential for non-linear variations in EKE in a significantly warmer world (Orbe et al. 2023), and given our expectation of reaching high CO₂ levels in the future, it becomes crucial to systematically investigate the response of storm tracks at intermediate CO₂ forcing levels above 4×CO₂ using more realistic Earth system model simulations. This endeavor is important because comprehending and predicting how storm tracks will respond in future warming scenarios beyond the 21st century is essential for developing effective adaptation and mitigation strategies in the next century, particularly in the event of a non-linear response.

Our primary objective here is to address the question regarding the linearity of the intensification of the winter storm tracks in the Southern Hemisphere in relation to increasing CO₂ concentrations. We focus on the storm tracks in the Southern Hemisphere, as they exhibit a nearly zonally symmetric structure (Chemke et al. 2022a), which not only allows us to revisit the non-linear behavior of the storms previously found in zonally-symmetric idealized models (O’Gorman and Schneider 2008a), but such zonal symmetry is necessary for conducting a zonal spectral analysis. As further discussed below, the storms’ spectral response to different CO₂ levels is a key component in their non-linear behavior.

6.2 Methods

6.2.1 Models

We utilize two Earth system models: the large ensemble version of the Community Earth System Model (CESM-LE) and the NASA Goddard Institute for Space Studies Model E2.1-G (GISS-E2.1-G). The CESM-LE model incorporates the Community Atmosphere Model version 5 (CAM5) with 30 vertical levels, along with the Parallel Ocean Program version 2 (POP2) featuring 60 vertical levels. It employs a 1° horizontal resolution across all model components (Kay et al. 2015). The GISS-E2.1-G model includes a 40-level atmosphere with

a $2^\circ \times 2.5^\circ$ latitude/longitude resolution and a 40-level GISS Ocean v1 (GO1) component with a 1° horizontal resolution (Kelley et al. 2020). This specific GISS model configuration contributes to the Coupled Model Intercomparison Project 6 (CMIP6) project and is referred to as “GISS-E2-1-G”.

In addition, we utilize experiment output from the extended Representative Concentration Pathway 8.5 (RCP8.5) scenario from CMIP5 and Shared Socioeconomic Pathway 5-8.5 (SSP5-8.5) from CMIP6. These scenarios run up to year 2300 with up to $7.6 \times \text{CO}_2$ relative to PI levels. We only use seven models in total because those were the only models we could find output for daily variables for the zonal and meridional winds. The CMIP5 models used are MPI-ESM-LR, IPSL-CM5A-LR, CSIRO-Mk3-6-0, and the CMIP6 models are CanESM5, ACCESS-ESM1-5, MRI-ESM2-0, EC-Earth3-Veg.

6.2.2 Experiments

In our study, we conduct abrupt- CO_2 experiments using both CESM-LE and GISS-E2.1-G models, applying forcings of $2\times$, $3\times$, $4\times$, $5\times$, $6\times$, $7\times$, and $8\times\text{CO}_2$, relative to pre-industrial climate. During these experiments, trace gases, ozone concentrations, aerosols, and other forcings are maintained at pre-industrial (PI) values. The integration period for all runs is set to 150 years, starting from PI conditions, following a similar protocol to the CMIP6 guidelines for $4\times\text{CO}_2$ runs. The response to abrupt CO_2 forcing is assessed by comparing these experiments with a PI control run.

To verify that our results also hold under a more realistic increase in CO_2 , we conduct transient CO_2 experiments using both models. These experiments begin from PI conditions, similar to the abrupt CO_2 experiments. The CO_2 concentration is then increased at a rate of 1% per year (1pctCO2) for a duration of 215 years, reaching slightly above $8\times\text{CO}_2$. The response to transient CO_2 forcing is assessed by comparing this experiment with a PI control run.

6.2.3 EKE Calculation

Consistent with previous studies (Chang et al. 2012; Chemke and Ming 2020; Chemke et al. 2022b; Coumou et al. 2015; O’Gorman and Schneider 2008a), we assess the intensity of the winter (June-August) storm tracks in the Southern Hemisphere using the vertically integrated transient eddy kinetic energy (EKE) as,

$$\text{EKE} = \frac{1}{2g} \int_0^{p_s} (u'^2 + v'^2) dp \quad (6.1)$$

where g is the gravitational constant, u and v are the zonal and meridional wind, respectively, and prime denotes deviation from the monthly mean. We define the eddies as deviations from the monthly mean. Nevertheless, defining the eddies using a bandpass filter of 2-6 days does not change our results.

Additionally, the EKE spectrum is computed using a one-dimensional Fourier analysis in the zonal direction at each latitude (Saltzman 1957), following the methodology employed in Chemke and Ming 2020,

$$\text{EKE}_k = \frac{1}{2g} \int_0^{p_s} (|u'_k|^2 + |v'_k|^2) dp, \quad (6.2)$$

where subscript k denotes the zonal wavenumber.

6.2.4 Spectral EKE budget

To identify the factors responsible for the changes in the EKE spectrum, we follow previous studies (Chemke and Ming 2020; Chemke and Kaspi 2015; Saltzman 1957) and calculate the EKE_k budget,

$$\frac{\partial \text{EKE}_k}{\partial t} = \text{PK} + \text{EM} + \text{EE} + \text{F}. \quad (6.3)$$

The term PK corresponds to the conversion of eddy available potential energy to eddy kinetic energy,

$$PK = -\frac{2}{g} \int_0^{p_s} \text{Re}\{\mathbf{u}'^* \cdot \nabla \varphi'_k\} dp \quad (6.4)$$

where \mathbf{u} represents the horizontal velocity vector, φ is geopotential, and p_s is the surface pressure. The asterisk symbol denotes the complex conjugate. The term EM describes the transfer of kinetic energy between the eddies and the zonal mean flow, with the overbar indicating the zonal average and θ the latitude.

$$\begin{aligned} EM = & -\frac{2}{g} \int_0^{p_s} \text{Re} \left\{ u'_k^* \cdot \left(\bar{\mathbf{u}} \cdot \nabla u' + \mathbf{u}' \cdot \nabla \bar{u} - \frac{\bar{u}v' \tan(\theta)}{a} - \frac{u'\bar{v} \tan(\theta)}{a} \right)_k \right. \\ & \left. + v'_k^* \cdot \left(\bar{\mathbf{u}} \cdot \nabla v' + \mathbf{u}' \cdot \nabla \bar{v} + 2\frac{\bar{u}u' \tan(\theta)}{a} \right)_k \right\} dp \end{aligned} \quad (6.5)$$

The term EE represents the energy transfer between different waves (eddies of different wavenumbers).

$$\begin{aligned} EE = & -\frac{2}{g} \int_0^{p_s} \text{Re} \left\{ u'_k^* \left(\mathbf{u}' \cdot \nabla u' - \frac{u'v' \tan \theta}{a} \right)_k \right. \\ & \left. + v'_k^* \left(\mathbf{u}' \cdot \nabla v' + \frac{u'u' \tan \theta}{a} \right)_k \right\} dp \end{aligned} \quad (6.6)$$

Finally, the term F incorporates the dissipation processes and is defined as the residual in our budget calculation.

6.3 Results

6.3.1 The non-linear behavior of the Southern Hemisphere EKE

We start by analyzing Southern Hemisphere wintertime EKE response in the historical and the extended highest emission scenarios SSP5-8.5 (CMIP6) and RCP8.5 (CMIP5) up to the year 2300. The multi model means and the cross-model spread in EKE response is

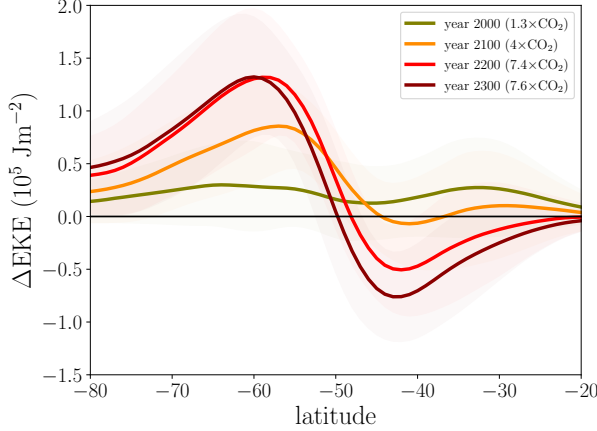


Figure 6.1: Vertically integrated zonal mean winter EKE response (relative to PI control run) in the Southern Hemisphere from CMIP models with extended SSP5-8.5 and RCP8.5 scenarios (see methods). The solid lines show the CMIP mean, and the shading shows one standard deviation across the models.

shown in Fig. 6.1. In the historical runs by the year 2000 (average over 1980-2000), there is an EKE intensification in both the low-mid and the mid-high latitudes (olive line). By 2100, the highest emissions scenarios, which correspond to around $4\times\text{CO}_2$, project an EKE intensification at mid-high latitudes and almost no response in the low-mid latitudes (orange line). By the year 2200, these emission scenarios reach around $7.4\times\text{CO}_2$, and a stronger EKE intensification occurs at mid-high latitudes, and a significant EKE reduction in the low-mid latitudes (red line). From year 2200 to year 2300, the CO₂ values increase from $7.4\times$ to $7.6\times\text{CO}_2$, which does not yield much EKE intensification in the mid-high latitudes, but a stronger reduction in the low-mid latitudes (dark red). Hence we find a non-linear EKE response in low-mid latitudes in the extended high emission scenarios: EKE initially intensifies up to 2100 and then weakens to year 2300. To further investigate the role of the CO₂ forcing alone in this non-linear response of the EKE in low-mid latitudes, we utilize idealized CO₂ increase experiments.

We analyze the wintertime EKE response in our idealized CO₂ experiments up to $8\times\text{CO}_2$ in Fig. 6.2. In the abrupt-CO₂ runs (Figs. 6.2a,b), we find that at low CO₂ levels ($2\times$ and $3\times\text{CO}_2$), the EKE intensifies more at mid-high latitudes than low-mid latitudes, consistent

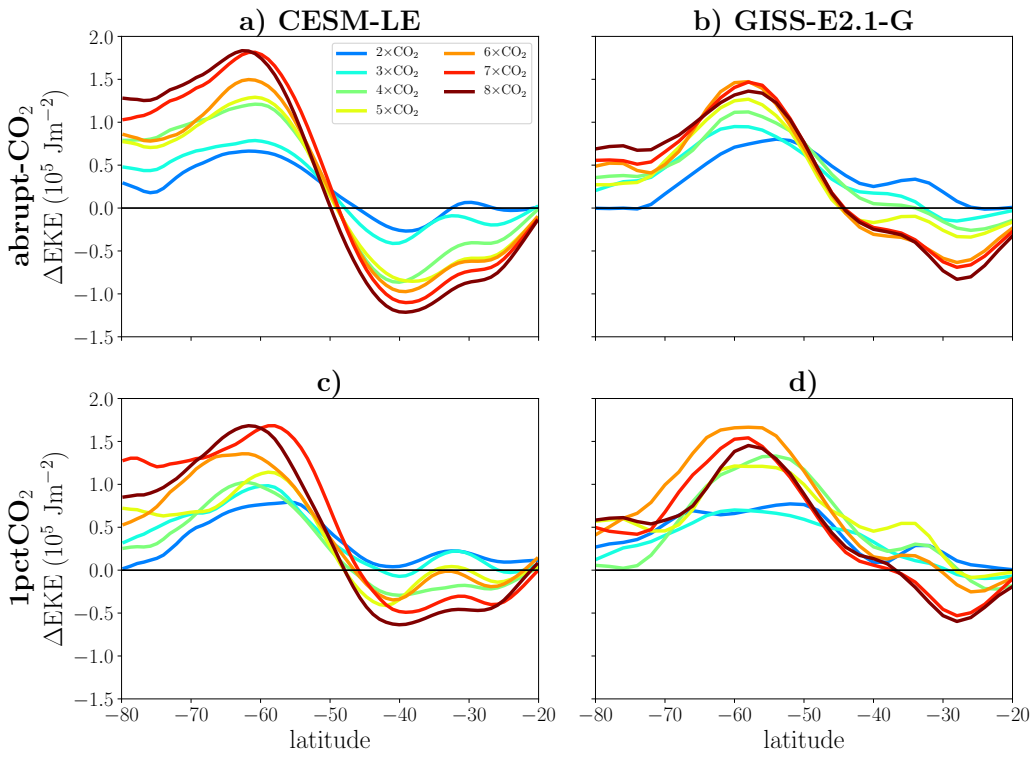


Figure 6.2: Vertically integrated zonal mean winter (JJA) Eddy Kinetic Energy (EKE) in the Southern Hemisphere for the (a,c) CESM-LE and (b,d) GISS-E2.1-G models. Panels (a) and (b) display the results from the abrupt-CO₂ runs, while panels (c) and (d) present the findings from the transient 1pctCO₂ runs.

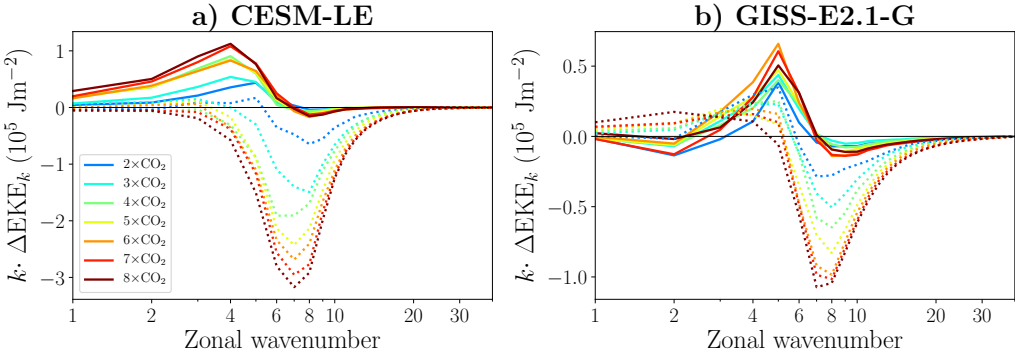


Figure 6.3: EKE_{*k*} as a function of zonal wavenumber in (a) CESM-LE and (b) GISS-E2.1-G models. The solid lines represent mid-high latitudes, while the dotted lines indicate low-mid latitudes. High and low latitudes are 30 degrees north and south, respectively, of the EKE maximum in the pre-industrial run (53°S for CESM-LE and 51°S for GISS-E2.1-G). The EKE changes are multiplied by the zonal wavenumber to preserve the logarithmic *x*-axis integral and are smoothed with a 3-point running mean for plotting purposes.

with the reported intensification by the end of this century in CMIP5 and CMIP6 models (Chang et al. 2012; Harvey et al. 2014). The EKE exhibits minor changes in the low-mid latitudes, with a slight reduction in the CESM-LE model (Fig. 6.2a) and some intensification in the GISS-E2.1-G model (Fig. 6.2b). As CO₂ levels increase (above 3×CO₂ for CESM-LE and 5×CO₂ for GISS-E2.1-G), extending up to 8×CO₂, the EKE continues to intensify in mid-high latitudes while decreasing in low-mid latitudes, resulting in a poleward shift of the EKE. This behavior is also evident under the more realistic transient 1pctCO₂ runs (Figs. 6.2c,d), although the response is weaker predominantly for the low-mid latitude EKE weakening. To further illustrate the zonally symmetric shift of the Southern hemisphere EKE towards mid-high latitudes, we present the EKE maps in Fig. D.1, supporting our focus on studying the storm track behavior from a zonal perspective.

Recently, Chemke and Ming 2020 demonstrated a scale-dependent response of projected EKE in 21st century emission scenarios; while large scale waves were found to intensify, small scale waves were found to weaken in the coming decades. It is thus crucial to examine the future changes in the storms as a function of their scale. To investigate this behavior in our experiments, we next examine the spectral structure of EKE (EKE_{*k*}, Equation 6.2). Fig. 6.3

reveals distinct patterns in the spectral EKE response. At mid-high latitudes (solid lines), EKE_k strengthens over large waves (wavenumbers 6 and below) with increasing CO₂ concentrations, exhibiting a nearly monotonic increase, with a minor decrease at small scales. At low-mid latitudes (dotted lines), EKE_k weakens monotonically over small waves (wavenumbers 7 and above) with increasing CO₂, with a minor increase at large scales (mostly in the GISS-E2.1-G model). Note that while the peak EKE increase at mid-high latitudes and the peak EKE decrease at low-mid latitudes occur on different wavenumbers, they occur over similar length scales (as the same wavenumber in different latitudes does not correspond to the same length scale). Nevertheless, as noted above, scale-dependent changes are evident even over the same latitudinal bands (solid/dotted lines). Neglecting the spectral structure of the EKE response would obscure these nuanced changes.

6.3.2 EKE_k Budget

We now investigate the underlying physical processes responsible for the scale-dependent response of EKE_k . We start by analyzing the budget equation of EKE_k (Chemke 2017; Chemke and Kaspi 2015; Saltzman 1957) as expressed in Equation 6.3. The EKE_k budget comprises four distinct terms that elucidate the factors contributing to changes in EKE_k : the conversion from eddy available potential energy to EKE (PK), the transfer of energy between waves and the zonal mean flow (EM), the interactions between different waves (EE), and the dissipation processes (F). In Fig. 6.4, we present the response of each term in the EKE_k budget relative to the PI for both the CESM-LE and GISS-E2.1-G models.

We first examine the EKE_k budget in the mid-high latitudes, where EKE_k intensifies roughly monotonically with increasing CO₂ forcing (solid lines in Fig. 6.4). We start with the analysis of the potential to kinetic energy conversion term (PK) in Figs. 6.4a and 6.4b. PK captures the process by which waves acquire kinetic energy by converting eddy available potential energy. This conversion, driven by baroclinic instability, is fundamental to the generation of atmospheric weather systems (Charney 1947; Eady 1949; Vallis 2017). In our

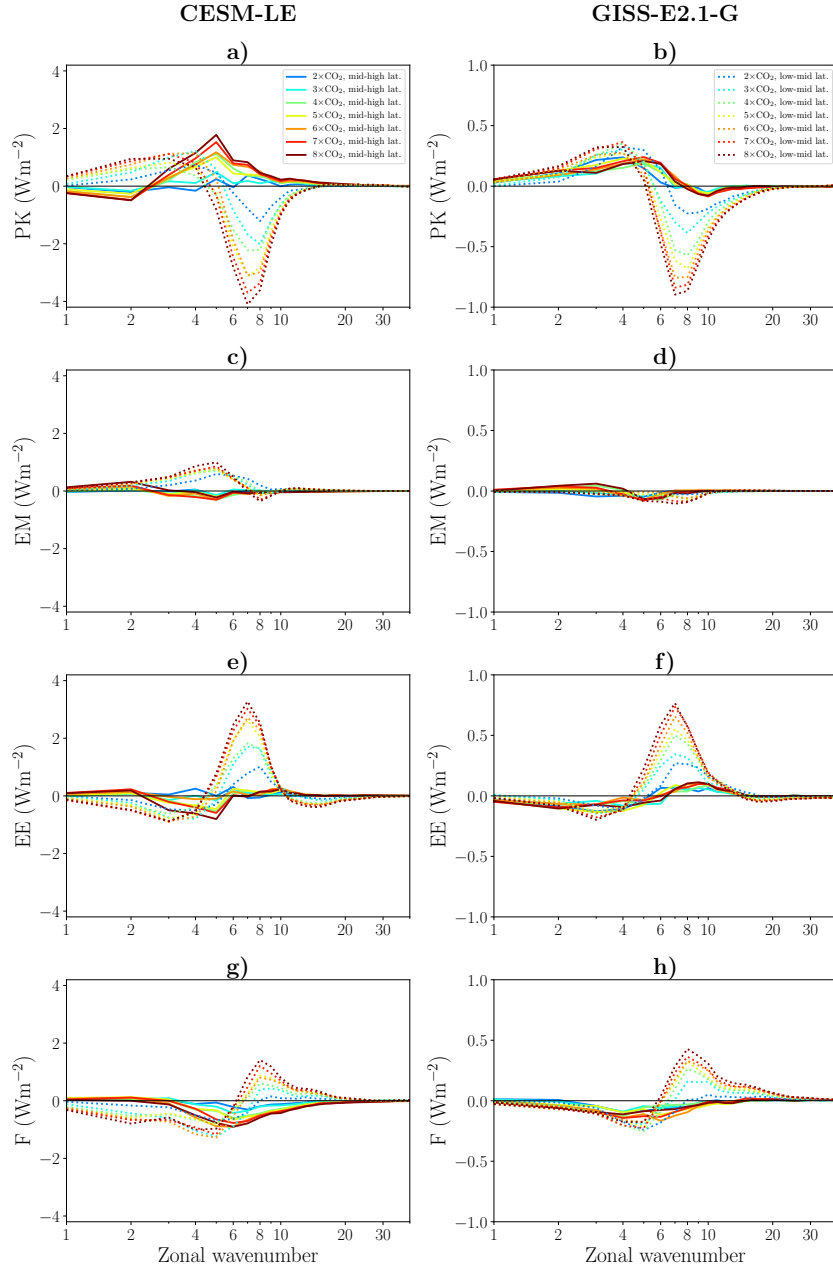


Figure 6.4: Components of the EKE_k budget from Equation 6.3: (a) and (b) depict the conversion of eddy available potential energy to EKE (PK), (c) and (d) illustrate the transfer of kinetic energy between the waves and the zonal mean flow (EM), (e) and (f) represent the energy transfer between different waves (EE), and (g) and (h) show the dissipation processes (F). The left column presents the data from the CESM-LE model, while the right column presents the data from the GISS-E2.1-G model. The response is multiplied by the zonal wavenumber to ensure the preservation of the integral on the logarithmic x -axis, and a 3-point running mean is applied for smoothing purposes.

experiments, the PK term explains the strengthening of EKE_k at high latitudes in both the CESM-LE and GISS-E2.1-G models. The increase in EKE_k at high latitudes (solid lines in Fig. 6.3) occurs primarily in large-scale waves (wavenumber 4 in CESM-LE and 5 in GISS-E2.1-G), and the peaks of PK (solid lines in Figs. 6.4a and 6.4b) correspond to the same peaks in EKE_k . These peaks exhibit a nearly monotonic upward shift in the CESM-LE model and, to a lesser extent, in the GISS-E2.1-G model. However, the EKE intensification at high latitudes is counteracted by the energy transfer from waves to the mean flow (EM, Figs. 6.4c and 6.4d) and the dissipation of energy (F, Figs. 6.4g and 6.4h). Moreover, the EKE gain in large scale waves is partially offset by the wave-to-wave interactions (EE, Figs. 6.4e and 6.4f) term, which involves the transfer of energy from small to large scale waves through an inverse cascade process (Chemke 2017; Chemke and Ming 2020; Chemke and Kaspi 2015).

The PK term also elucidates the scale-dependent decrease of EKE_k in low-mid latitudes (dotted lines in Fig. 6.4). It exhibits a scale-dependent response to CO_2 forcing, wherein large scale waves (e.g., wavenumber 2) strengthen at high CO_2 values, while small scale waves (e.g., wavenumber 7) weaken. This pattern is found in both the CESM-LE model (Fig. 6.4a) and the GISS-E2.1-G model (Fig. 6.4b). Moreover, the weakening of EKE_k at small scales and the strengthening at large scales, as seen in the EKE_k spectrum (Fig. 6.3), correspond to the response of the PK term. The EKE_k decrease at small scales is balanced by EKE_k gain from the EE and F terms, while the EKE_k increase at large scales is offset by EKE_k loss in the EE and F terms. Therefore, the scale-dependent response in the low-mid latitudes emphasizes the importance of examining the wave's response to CO_2 forcing with consideration of the wave scale.

We show that the PK term is responsible for the scale-dependent response and decrease of EKE_k in low-mid latitudes, which suggests that the baroclinic instability, which drives the generation of transient midlatitude waves, likely plays a crucial role in the scale-dependent response of EKE_k . However, the scale-dependent response in EKE_k at low-mid latitudes, where large waves intensify and small waves weaken, resulting in an overall decrease, may

pose challenges in explaining this EKE decrease using linear metrics such as the Eady Growth rate and the growth rate from the linear normal-mode instability analysis (see section 2.3 of Chemke and Ming 2020) integrated over the entire troposphere. We have computed both the Eady Growth rate and the growth rate from the instability problem on a latitude-by-latitude basis and found that they do not fully capture the complex behavior of EKE. The Eady Growth rate in the CESM-LE model (Fig. D.2a) captures the general intensification of EKE at high latitudes and reduction at low latitudes, but the relationship is not strictly monotonic with increasing CO₂. Similarly, the GISS-E2.1-G model (Fig. D.2b) exhibits contrasting behavior between the Eady Growth rate and EKE at low and high latitudes. The growth rate derived from the instability problem (Fig. D.3) also struggles to fully capture the intricate behavior of EKE. These findings suggest that the complex dynamics driving the scale-dependent response of EKE in low-mid latitudes may not be fully captured by these linear metrics integrated over the troposphere.

We are unable to fully explain the scale-dependent response in PK (and EKE) with the total baroclinicity of the atmospheric column. However, previous studies have investigated the impact of upper and lower tropospheric baroclinicity separately. For instance, Rivière 2011 found a scale-dependent response when the upper tropospheric baroclinicity was increased: large waves became more unstable, while small waves became less unstable. Conversely, when the lower tropospheric baroclinicity was enhanced, all wavenumbers exhibited increased instability. Furthermore, other studies have explored the mechanisms associated with baroclinicity, such as the position and magnitude of the lower and upper tropospheric temperature gradient, as well as their relationship to static stability (Harvey et al. 2014; Held and O'Brien 1992; Pavan 1996; Yuval and Kaspi 2020). In light of these findings, our subsequent analysis will investigate the response of PK in relation to changes in lower and upper baroclinicity.

We begin by examining the correlation between the PK response and the upper and lower level baroclinicity, as depicted in Fig. 6.5a-c (correlation scatterplots are shown in Fig. D.4).

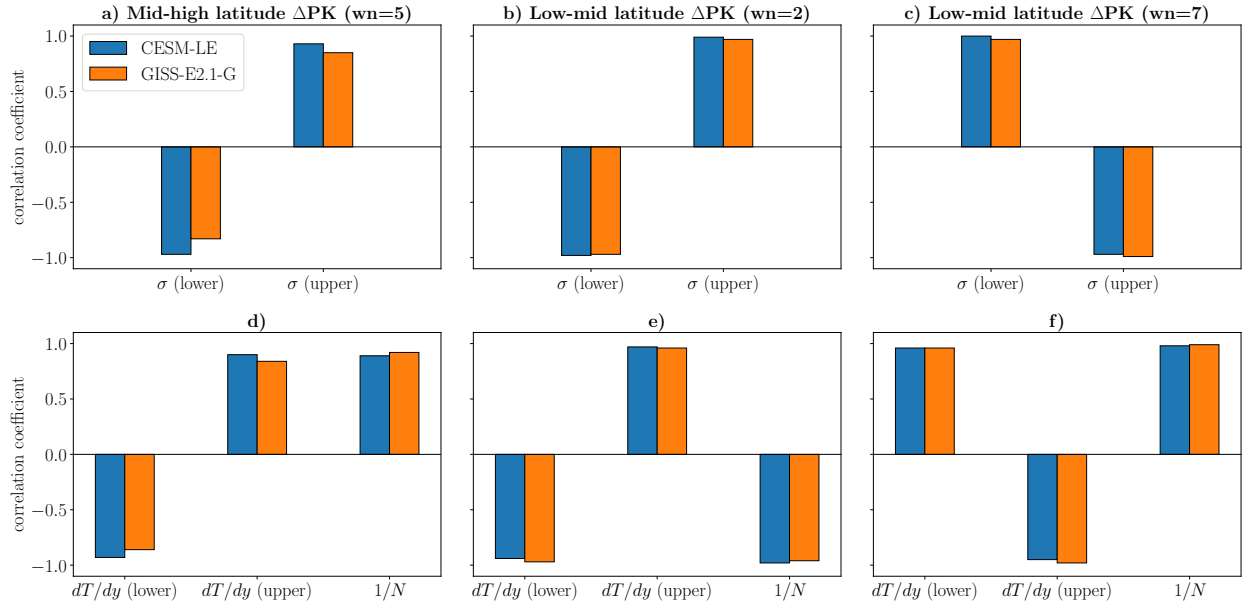


Figure 6.5: (a-c) Correlation between PK and lower & upper baroclinicity from $2\times$ to $8\times\text{CO}_2$ in the abrupt experiments. We approximate the baroclinicity with the Eady Growth Rate as $\sigma = \frac{dT/dy}{N}$. (d-e) Correlation between PK and the mechanisms governing σ : the meridional temperature gradient dT/dy and the inverse of static stability $1/N$. Panels (a) and (d) represent mid-high latitudes, and panels (b), (c), (e), and (f) the low-mid latitudes. The large scale waves (wavenumber 2) at low latitudes are shown in panels (b) and (e), and small scale waves (wavenumber 7) in panels (c) and (f). The upper tropospheric σ (black) is integrated from 250 to 500hPa, while the lower tropospheric σ from 500hPa to the surface. The correlation coefficient is the r-value.

We use positive correlations to explain the PK response. Specifically, at mid-high latitudes, where EKE intensifies, we correlate the maximum PK response across wavenumbers (in this case, wavenumber 5) with the upper and lower baroclinicity represented by the Eady Growth Rate σ in Fig. 6.5a. We find strong positive correlations between PK and the σ (upper) in both models (blue and orange), which reveal that the increase in PK at mid-high latitudes is associated with the amplification of upper level baroclinicity. These findings are consistent with previous studies that have established a link between the upper-level baroclinicity increase and EKE intensification at mid-high latitudes (Harvey et al. 2014; Yuval and Kaspi 2020). It is important to note that while PK at high latitudes demonstrates a strong positive correlation with the upper level σ , the correlation with lower level σ is strongly negative but not meaningful (it implies that the increase in PK is correlated with a decrease in lower level baroclinicity). To ensure clarity, only the positive correlations explain changes in PK.

Next, we focus on the PK response in the low latitudes (Figs. 6.5b,c), which exhibits a non-linear behavior. We first investigate the large scale waves (wavenumber 2, Fig. 6.5b) that drive the PK intensification at low-mid latitudes. We find that the increase in upper level baroclinicity also drives their intensification. However, the PK decrease in the low latitudes, which is primarily driven by the small scale waves (wavenumber 7) compensating for the intensification of large waves, is associated with the decrease in lower level baroclinicity, as depicted in Fig. 6.5c. Thus, the PK decrease at low-mid latitudes is attributed to the weakening of lower level σ . Consequently, the opposing behaviors in small and large scale waves stem from the contrasting responses in low and high tropospheric σ . Specifically, as CO₂ forcing increases, the intensification of PK in the low latitudes due to upper level baroclinicity is offset by the decrease in PK resulting from lower level baroclinicity. This interplay between upper and lower level baroclinicity under increasing CO₂ leads to the non-linear response in PK (and hence EKE) at low latitudes.

To investigate the mechanisms influencing baroclinicity and PK in both high and low

latitudes, we examine the variables related to available potential energy, specifically the meridional and vertical temperature gradients. In Fig. 6.5d-f, we analyze the upper and lower tropospheric temperature gradients (dT/dy) separately and the inverse of static stability ($1/N$). We show the correlation scatterplots in Fig. D.5. At high latitudes (Fig. 6.5d), the increase in PK at high CO₂ values is attributed to the decrease in static stability (increase in $1/N$) and the increase in the upper tropospheric temperature gradient. These results are consistent with the findings of Chemke and Ming 2020, which showed that the increase in PK is associated with a decrease in static stability and an increase in the meridional temperature gradient.

In the low latitudes, the PK intensification at large waves (wavenumber 2) is explained by the increase in the upper tropospheric temperature gradient (Fig. 6.5e). On the other hand, the PK decrease at small waves (wavenumber 7) in the low latitudes is attributed to the increase in static stability and the decrease in the lower tropospheric temperature gradient (Fig. 6.5f). Both the lower tropospheric gradient and the static stability in the low-mid latitudes are expected to decrease in a warmer world, reducing atmospheric baroclinicity and EKE (Harvey et al. 2014; Lim and Simmonds 2009).

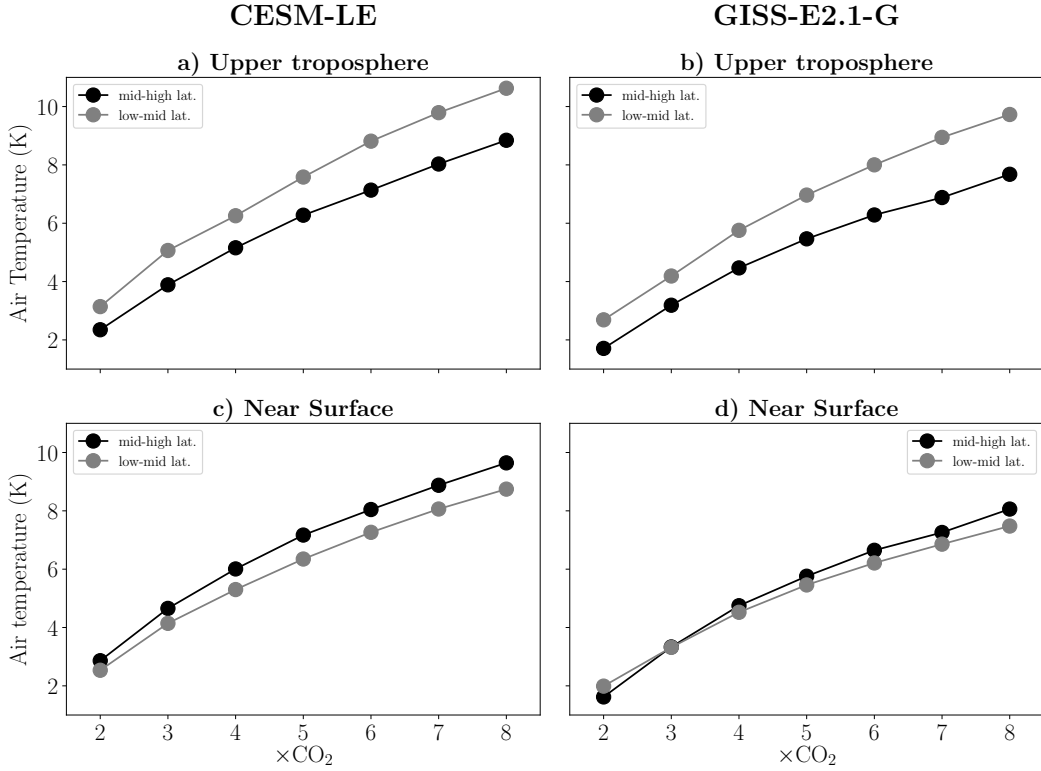


Figure 6.6: Southern Hemisphere winter air temperature response in (a,b) the upper troposphere and (c,d) near surface for mid-high (black) and low-mid (gray) latitudes. The left column presents the data from the CESM-LE model, while the right column presents the data from the GISS-E2.1-G model. The upper troposphere is 250 to 500hPa, and the “near surface” is 500hPa to the surface.

Our findings highlight the significant relationship between the decrease in Eddy Kinetic Energy (EKE) in low latitudes and the corresponding decline in the lower tropospheric meridional temperature gradient (dT/dy). To better understand the response of the upper and lower tropospheric dT/dy , we show the air temperature response (dT) in the mid-high and low-mid latitudes as a function of CO_2 values in Fig 6.6. The difference between the low-mid (gray) and mid-high latitudes (black) is how we approximate dT/dy . In the upper troposphere (Figs. 6.6a,b), dT/dy is positive and intensifies as CO_2 concentrations increase. Near the surface (Figs. 6.6c,d), at low CO_2 values of $2\times$ and $3\times\text{CO}_2$, dT/dy is either very small (Fig. 6.6c) or negative (Fig. 6.6d), but at high CO_2 values dT/dy is negative. As a result, the increase in EKE at high latitudes occurs at low and high CO_2 levels, while the decrease in EKE at low-mid latitudes occurs at higher CO_2 levels after near surface dT/dy

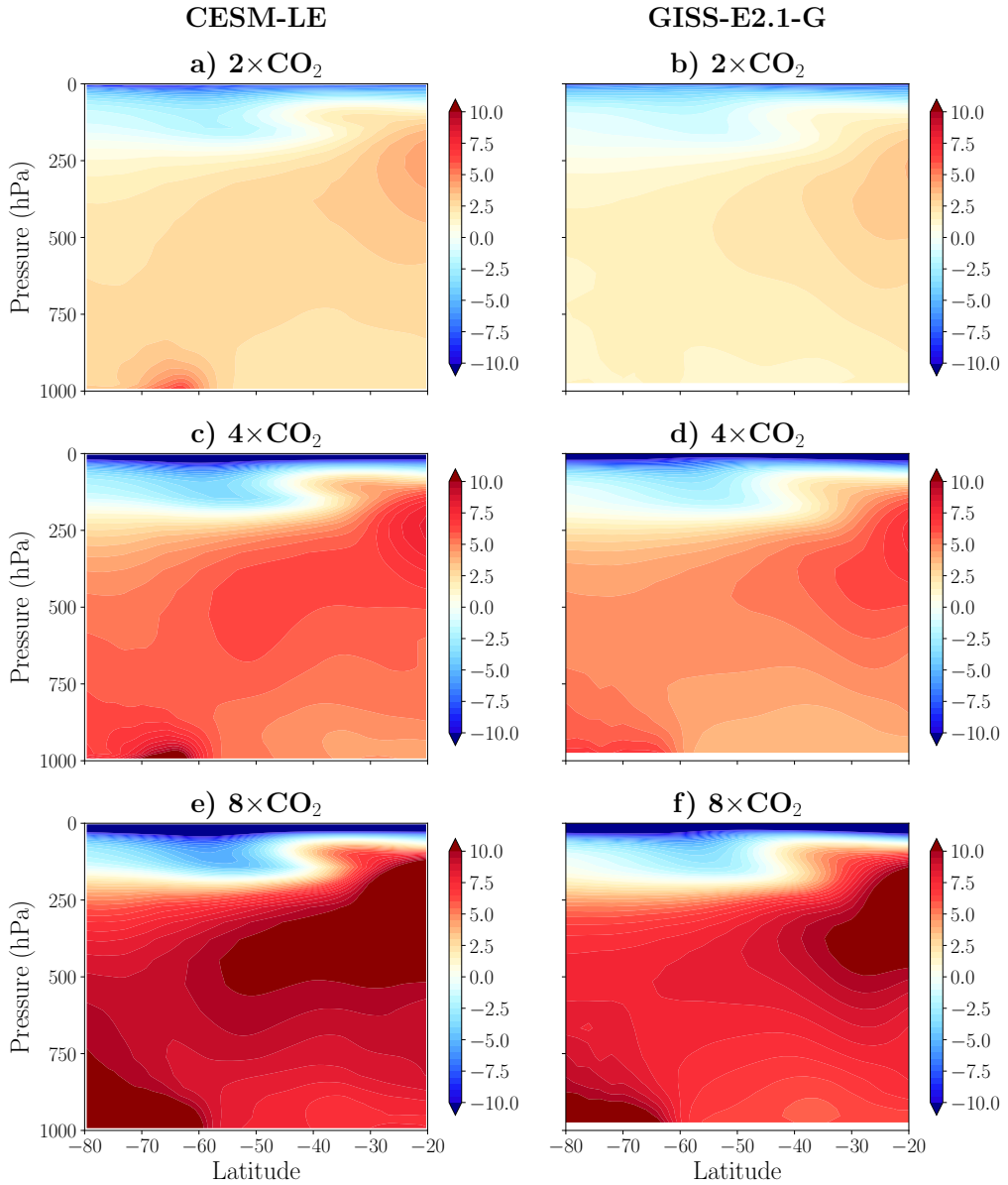


Figure 6.7: Southern Hemisphere winter (JJA) air temperature response in (a,b) 2 \times CO₂, (c,d) 4 \times CO₂, and (e,f) 8 \times CO₂ for the last 50 years of the abrupt-CO₂ runs. The left column presents the data from the CESM-LE model, while the right column presents the data from the GISS-E2.1-G model.

becomes more negative.

Furthermore, we show the zonal air temperature response in our abrupt-CO₂ experiments in Fig. 6.7. It is evident that the upper troposphere warms faster in the low-mid latitudes compared to mid-high latitudes, and the opposite occurs in the lower troposphere. The near surface warming in the mid-high latitudes is less pronounced at 2×CO₂ (Figs 6.7a,b) and more evident at higher CO₂ values such as 4× (Figs. 6.7c,d) and 8×CO₂ (Figs. 6.7e,f). The opposing behaviors of the meridional temperature gradient, with a strengthening aloft and a reduction near the surface, significantly contribute to the EKE shift, weakening EKE in low-mid latitudes and strengthening in mid-high latitudes.

In their analysis of CMIP5 models, Harvey et al. 2014 found an increase in both the upper and lower tropospheric meridional temperature gradients during winter in the Southern Hemisphere. They demonstrated a strong correlation between these temperature gradients and storm tracks, resulting in an increase in EKE in mid-high latitudes and a minor increase in low-mid latitudes in their 21st century projections. However, unlike the Northern Hemisphere, where the lower tropospheric temperature gradient decreased due to polar amplification, they found a weak to no polar amplification in the Southern Hemisphere. Consequently, the lower tropospheric temperature gradient in the Southern Hemisphere increased (similar to our GISS-E2.1-G model in Fig. 6.6d), with the tropics experiencing more significant warming than the polar region. In our simulations, as we increase CO₂ up to 8×CO₂, we find a minor increase in the lower tropospheric temperature gradient in the GISS-E2.1-G model (Fig. 6.6d) and a minor decrease in the lower tropospheric temperature gradient in the CESM-LE model (Fig. 6.6c). This leads to a minor increase in EKE in the GISS-E2.1-G model and a decrease in EKE in the CESM-LE model at low latitudes. However, at sufficiently high CO₂ levels where polar amplification becomes evident (Fig. 6.7), the increase in the lower tropospheric temperature gradient outweighs the EKE increase in low latitudes, particularly in the small scale waves (large wavenumbers), resulting in an overall reduction in EKE.

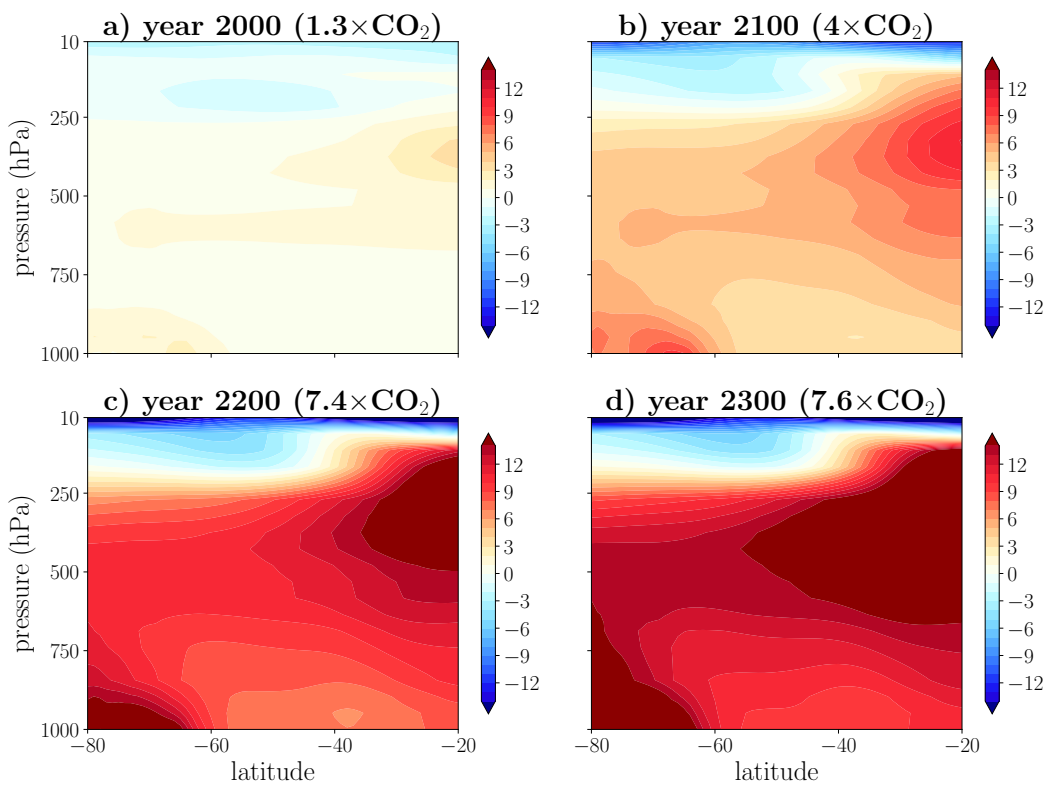


Figure 6.8: Multi model mean Southern Hemisphere winter air temperature response in extended RCP8.5 and SSP5-8.5 scenarios up to (a) year 2000, (b) year 2100 with approximate $4 \times \text{CO}_2$, (c) year 2200 with $7.4 \times \text{CO}_2$, and (d) year 2300 with $7.6 \times \text{CO}_2$.

Furthermore, the air temperature response in the extended RCP8.5 and SSP5-8.5 emissions scenarios in Fig. 6.8 looks very similar to the response in our idealized CO₂ experiments (Fig. 6.7). By the year 2100 (Fig. 6.8b), the upper troposphere warms faster in the low-mid latitudes compared to mid-high latitudes, inducing positive dT/dy that acts to strengthen the baroclinicity and EKE over all latitudes. The lower tropospheric dT/dy weakens and acts to decrease the baroclinicity and EKE at low-mid latitudes, but the weakening is minor compared to the dT/dy weakening by the year 2200 at 7.4×CO₂ (Fig. 6.8c). Hence, at 2200 we have EKE reduction in the low-mid latitudes, which follows the dT/dy and baroclinicity mechanism from Figs. 6.4 and 6.5. By 2300 (Fig. 6.8d), the lower tropospheric dT/dy has strengthened even more than 2200, yielding an even greater reduction in low-mid latitude EKE. Hence, we confirmed our temperature gradient mechanism from the idealized CO₂ experiments with the extended emission scenarios.

6.4 Discussion and Conclusion

We examine the behavior of Southern Hemisphere winter storm tracks through the analysis of eddy kinetic energy (EKE) during June-July-August (JJA) under high CO₂ experiments using the 1) extended RCP8.5 and SSP5-8.5 scenarios and 2) experiments with two Earth system models with abrupt and transient CO₂ experiments. While previous studies using CMIP5 and CMIP6 models have generally reported an overall intensification of EKE in the Southern Hemisphere winter, our findings reveal a non-linear response to increasing CO₂ levels beyond 2100. Specifically, we find that at low CO₂ values, EKE strengthens at high latitudes with minimal changes at low latitudes. However, as CO₂ levels continue to rise, EKE weakens at low latitudes and maintains its intensification at high latitudes.

This non-linear EKE response can be attributed to scale-dependent effects. Large waves amplify under both low and high CO₂ conditions, while small waves attenuate primarily at high CO₂ levels. In the Southern Hemisphere's low-mid latitudes, the weakening of small waves outweighs the strengthening of large waves, resulting in a decrease in EKE. By analyz-

ing the spectral EKE budget, we identify the conversion of eddy available potential energy to EKE (PK) as the primary driver of this scale-dependent response. The strengthening of large waves and the subsequent increase in EKE at mid-high and low-mid latitudes are associated with enhanced upper tropospheric baroclinicity (as indicated by the Eady growth rate σ). In contrast, the weakening of small waves and the consequent decrease in EKE at low-mid latitudes are linked to reduced lower tropospheric baroclinicity. Further decomposition reveals that the upper tropospheric meridional temperature gradient (dT/dy) leads to an increase in upper tropospheric σ , while the lower tropospheric dT/dy contributes to a decrease in lower tropospheric σ . The overall baroclinicity response is enhanced by changes in the static stability ($1/N$) in both high and low latitudes.

In addition to our idealized abrupt and transient CO₂ experiments, we find the same Southern Hemisphere wintertime EKE shift within the extended RCP8.5 and SSP5-8.5 scenarios. By 2100, the storm tracks intensify over all latitudes due to upper tropospheric dT/dy strengthening, with little to no response in the lower tropospheric dT/dy . As we advance to 2200 and 2300, EKE intensifies at mid-high latitudes and weakens in the low-mid latitudes. The weakening is likely due to the lower tropospheric dT/dy weakening at higher CO₂ values when delayed polar amplification kicks in the Southern Hemisphere (Fig. 6.8). The EKE weakening at mid-low latitudes and strengthening at mid-high latitudes results in a similar EKE shift we find with our idealized CO₂ experiments. Hence, we confirm our idealized CO₂ experiments with the more realistic emission pathways that not only consider changes in CO₂ but other constituents as well.

While our results demonstrate consistent EKE shifts in the transient 1pctCO₂ runs, the magnitude of EKE reduction in the low-mid latitudes is smaller than in the abrupt-CO₂ runs. This discrepancy could be attributed to the level of equilibration reached in the simulations and the time required for polar amplification to fully manifest, influencing the strength of the lower tropospheric temperature gradient. As in the extended runs between years 2200 and 2300, there is little change in CO₂ from $7.4 \times$ to $7.6 \times$ CO₂, but the EKE reduction at year

2300 is almost a third higher than the reduction at 2200. Hence, the lower response in the transient 1pctCO₂ runs is likely due to the transient state being far from quasi-equilibrium.

Our study highlights the contrasting responses of the upper and lower tropospheric meridional temperature gradients, which have opposing effects on the baroclinicity of the atmospheric flow. The strengthening of the upper tropospheric gradient enhances baroclinicity, while the decreasing lower tropospheric gradient under high CO₂ conditions, driven by polar amplification, weakens baroclinicity. Consequently, simple metrics such as the Eady growth rate averaged over the entire atmospheric column are insufficient to explain the EKE shift (Fig. D.2). To better understand the non-linear EKE shift, it is necessary to consider the contributions of upper and lower baroclinicity separately (Fig. 6.4). The scale-dependent response of EKE (Fig. 6.2) and the conversion of eddy available potential energy to EKE (Fig. 6.3a,b) in our study presents a challenge for linear normal-mode instability analysis (Fig. D.3), which does not account for the interaction between large and small waves. While previous studies have successfully explained baroclinicity changes using linear theory, it is worth noting that most of these investigations focused on single forcing levels across models. Our analysis, encompassing a range of forcing levels from 2× to 8×CO₂, suggests that linearity may not be applicable in this context.

In conclusion, our findings reveal a non-linear response of Southern Hemisphere winter storm tracks to high CO₂ scenarios, which we attribute to the baroclinicity response associated with polar amplification. Despite projections of overall increased EKE in the Southern Hemisphere's winter by the end of the 21st century, our study demonstrates the importance of considering the spatial and temporal variability of storm tracks. This non-linear behavior has important implications for time-sensitive mitigation strategies in the next century, as current approaches focusing solely on increasing storminess need to be adapted. Mitigation strategies should account for the spatial heterogeneity of storm track activity, with some regions experiencing reduced storminess in a warmer world while mid-high latitudes are expected to undergo increased storm track activity.

Chapter 7: Conclusion

In this thesis, I investigate the response of the climate system to a wide range of CO₂ forcing ranging from $1/8$ to 8 times pre-industrial levels. I focus on whether the response is symmetric, linear, and monotonic, and if not, what mechanisms are responsible. To address these questions, I examine the effective climate sensitivity (EffCS), feedbacks, radiative forcing, sea ice, precipitation, the width of the tropics, Hadley Cell strength, and storm tracks.

In Chapter 2, I examined the symmetry of the climate system's response across a wide range of positive (warm) and negative (cold) CO₂ forcings. While previous studies have established that EffCS exhibits CO₂ dependence (Chalmers et al. 2022; Colman and McAvaney 2009; Hansen et al. 2005; Russell et al. 2013), here I extended the analysis by considering a broader CO₂ range, using two different fully coupled climate models (CESM1-LE and GISS-E2.1-G) and, most importantly, I performed the experiments with both abrupt and transient CO₂ runs spanning the range $1/8\times$ to $8\times$ CO₂. The investigation revealed an asymmetric response between colder and warmer experiments in terms of global mean surface air temperature (ΔT_s) and EffCS. Notably, the ΔT_s response at $8\times$ CO₂ was more than a third greater than the corresponding cooling observed at $1/8\times$ CO₂, which I demonstrate is due to an asymmetry in the non-logarithmic CO₂ forcing, not to changes in radiative feedbacks.

In Chapter 3, I investigated whether the effective climate sensitivity EffCS monotonically increases with warming. It has been shown that EffCS increases at higher CO₂ levels (Bloch-Johnson et al. 2021a), but most studies focus on CO₂ doublings and overlook intermediate CO₂ values. Using two climate models, I examined a series of simulations with abrupt increases in CO₂ from $2\times$ to $8\times$ CO₂. I found that EffCS is a non-monotonic function of CO₂, with a minimum at $4\times$ CO₂ in the CESM-LE and $3\times$ CO₂ in the GISS-E2.1-G model. The minimum in EffCS is associated with anomalously negative radiative feedback,

which is caused by a cooling pattern in the sea-surface temperatures (SSTs) of the North Atlantic. This cooling is associated with the collapse of the Atlantic Meridional Overturning Circulation (AMOC), which has also been observed in other CMIP6 models as a response to increasing CO₂. I also found that this non-monotonic behavior with increasing CO₂ is present in many other aspects of the climate system, including the Arctic sea-ice extent (Liang et al. 2022), precipitation, the width of the dry zones, and the strength of the Hadley cell.

In Chapter 4, I focused on elucidating the mechanisms responsible for the non-monotonic response in EffCS under 4×CO₂ forcing in CESM-LE and 3×CO₂ forcing in the GISS-E2.1-G model, as presented in Chapter 3. The EffCS has a minimum at the CO₂ value when the AMOC collapses within the model. The AMOC is crucial in transporting warm equatorial waters to the North Atlantic region. As a result, the cessation of AMOC in the model triggers a cooling effect in the subtropical and North Atlantic areas. This cooling effect stabilizes the troposphere and enhances the Estimated Inversion Strength in the eastern regions of the subtropical and North Atlantic Ocean. As a result, there is an increase in the formation of low-level clouds in these areas. These low-level clouds act as a negative feedback mechanism within the climate system, contributing to decreased EffCS and overall cooling. It is important to note that the minimum value of EffCS is only observed at the specific CO₂ concentration when the AMOC collapses. At higher CO₂ concentrations, the warming effect caused by CO₂ forcing overwhelms the relative cooling observed in the subtropical and North Atlantic regions. Hence, both the local low-cloud feedback and the cooling effect in the subtropical and North Atlantic areas diminish.

In Chapter 5, I focused on the dependence of Effective Radiative Forcing (ERF) on CO₂ concentrations, ranging from 1/16× to 16×CO₂. The ERF is composed of two components: Instantaneous Radiative Forcing (IRF) and adjustments. While previous studies primarily explored the state dependence of the IRF using idealized models and radiative transfer calculations, in this chapter, I aimed to understand the state dependence of the ERF and

examine the contributions from both IRF and adjustments.

I found a significant increase in ERF as CO₂ concentrations increased, primarily driven by the increase in IRF. I attributed the rise in IRF with CO₂ to the cooling effect on the stratosphere caused by CO₂ forcing. Interestingly, the adjustments displayed an opposite trend, decreasing as CO₂ concentrations increased. The opposite trend in the adjustments comes from the asymmetric response in the stratospheric temperature adjustment between comparable CO₂ warming and cooling scenarios. Specifically, the stratospheric temperature exhibited greater warming in CO₂ decrease scenarios compared to the cooling observed in CO₂ increase scenarios. This asymmetry was mainly within the lower stratospheric region. Future investigations will determine whether this phenomenon arises from dynamic factors or the radiative response within the stratosphere.

In Chapter 6, I examined the behavior of mid-latitude winter storm tracks in the Southern Hemisphere in response to increasing CO₂ concentrations up to 8×CO₂. While climate models project a future intensification of the storm tracks by the end of the 21st century, previous studies employing idealized models have demonstrated a non-monotonic relationship between storm track response and rising temperatures (O’Gorman and Schneider 2008a). Expanding upon these prior studies, I investigate the response of mid-latitude winter storm tracks in the Southern Hemisphere to elevated CO₂ levels. Surprisingly, I find that at high CO₂ concentrations, the storm tracks no longer exhibit a uniform intensification throughout the extratropical regions, as predicted for the end of the 21st century. Instead, the storm tracks shift poleward with reduced storm activity at low-mid latitudes and intensified activity at the high-mid latitudes.

By analyzing the EKE budget, I attribute the non-monotonic storm track response to an increase in CO₂ levels to the scale dependent response of the conversion of mean available potential energy (MAPE) to eddy kinetic energy (EKE). At low CO₂ levels, this energy conversion increases EKE of large scales. However, at high CO₂ levels, this energy conversion increases the EKE of large scales and reduces the EKE of small scales, resulting in a poleward

shift of the storms.

Further analysis of variables that control the MAPE to EKE conversion showed that the weakening of the lower tropospheric meridional temperature gradient (dT/dy) is accountable for the observed poleward shift of the storm tracks. The upper tropospheric dT/dy responds more rapidly at low CO₂ values, contributing to the poleward intensification of storm tracks. The lower tropospheric dT/dy responds more sluggishly (at higher CO₂ concentrations) due to delayed polar amplification, resulting in weakened storm tracks at lower latitudes and a poleward storm track shift at elevated CO₂ values.

The preceding chapters have contributed to the advancement of understanding regarding the linearity of the climate system's response to idealized CO₂ forcing. Despite the climate system's inherent non-linearity, there is a tendency to linearize the response when examining CO₂ perturbations. The findings presented in this study have demonstrated that the response attributed to CO₂ perturbations is not linear. Therefore, caution must be exercised when scaling responses from specific CO₂ perturbation levels, such as 4×CO₂, or other magnitudes. Moreover, when utilizing paleoclimate evidence, it is imperative to carefully consider the state dependence of not only the feedbacks but also the radiative forcing. The study has illustrated that non-linearities may arise due to the CO₂ concentration or the state dependence of feedbacks, radiative forcing, and ocean response. A comprehensive understanding of these non-linearities is crucial for reliable interpretations of paleoclimate data.

Appendix A: “Asymmetric Warming/Cooling Response to CO₂ Increase/Decrease Mainly Due to Non-Logarithmic Forcing, not Feedbacks”

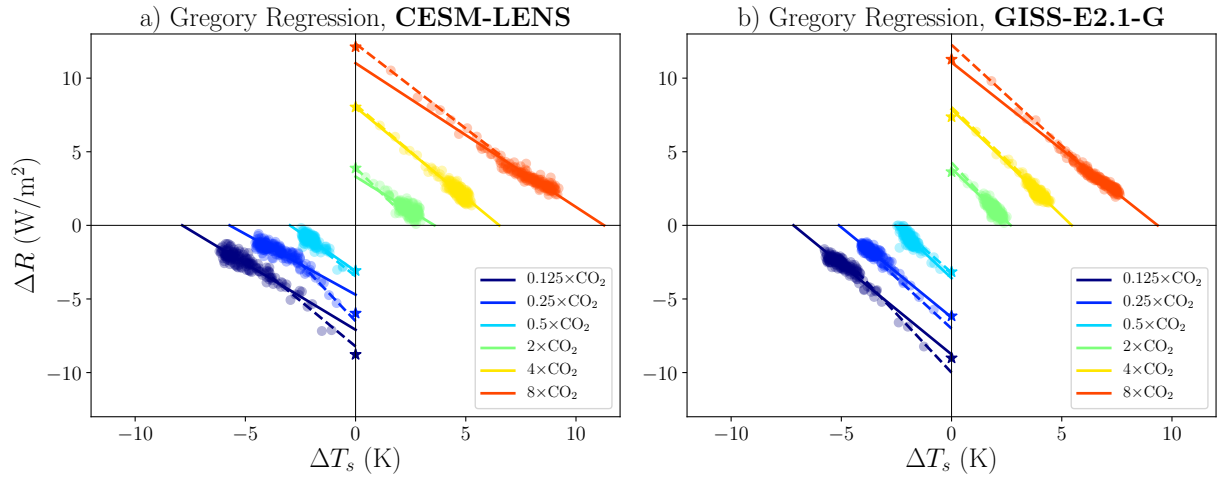


Figure A.1: Gregory regression plots for a) CESM-LENS, and b) GISS-E2.1-G model. The solid lines show regression for years 1-150, and the dashed lines for years 1-20. The stars on the y -axis show the effective radiative forcing (ERF) calculated from the fixed SST and SIC runs.

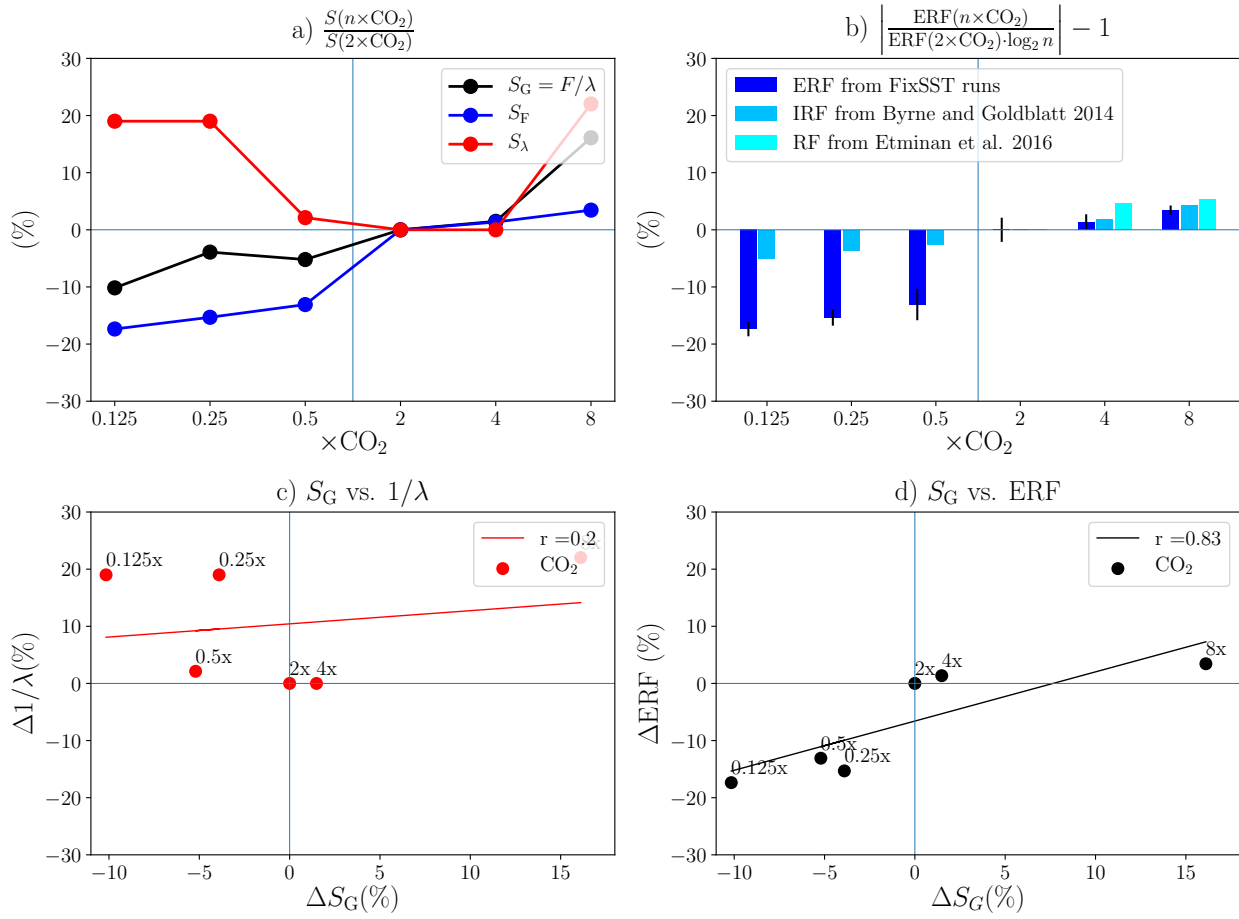


Figure A.2: Same as Figure 2.2 in the main text except using the GISS-E2.1-G model.

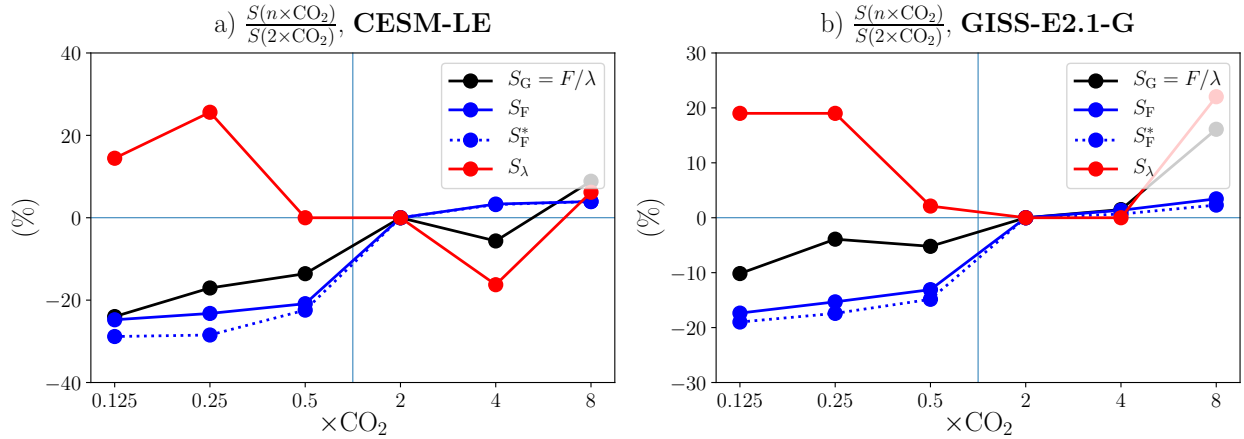


Figure A.3: Same as Figure 2.2a and A.2a in the manuscript, except here we show S_F^* , which contains a correction to the surface temperature change in fixed SST and SIC runs as per Equation 1 in Hansen et al. 2005. Panel a) shows CESM-LE, and panel b) shows GISS-E2.1-G data.

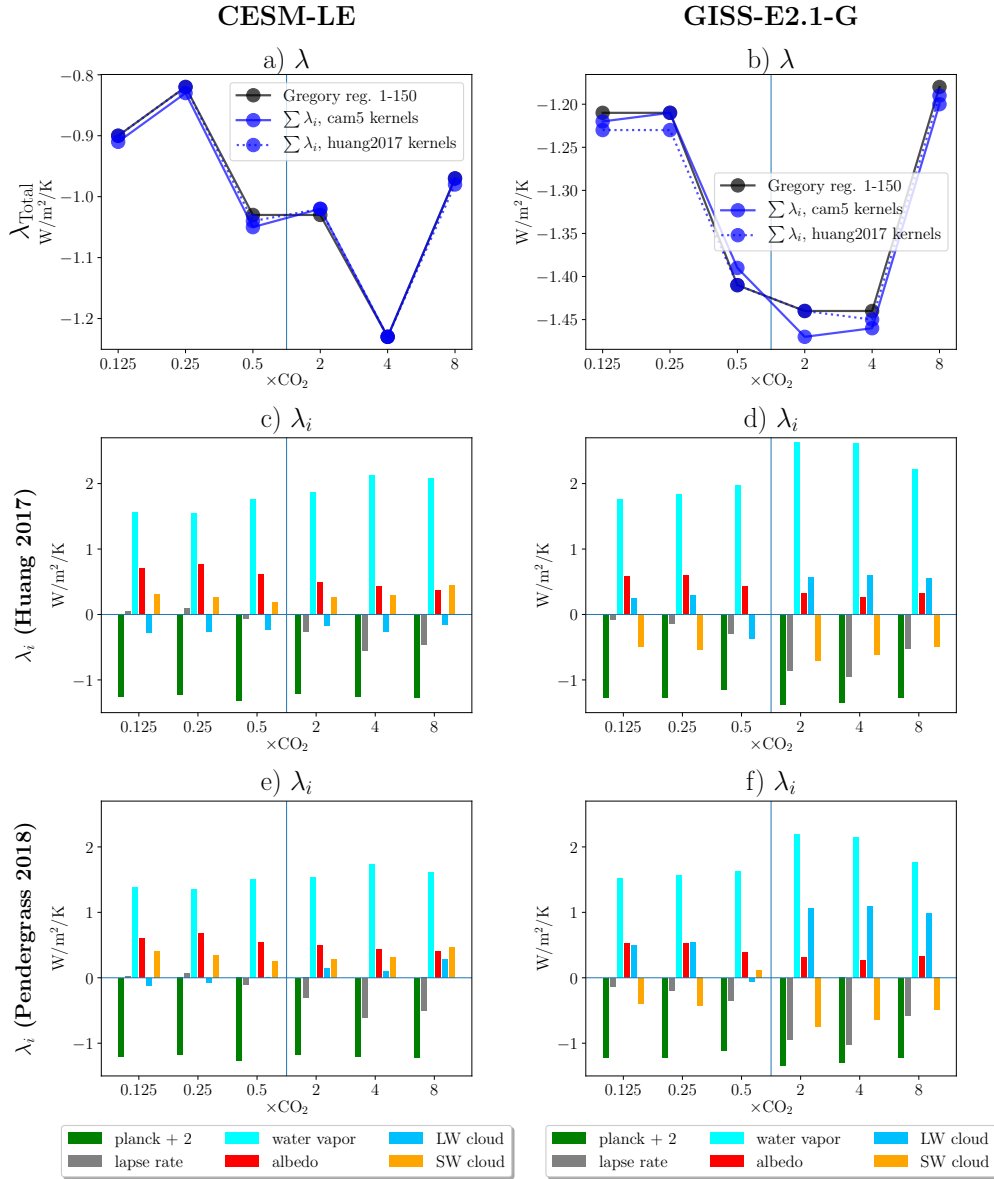


Figure A.4: Feedbacks with CESM-LE (left) and GISS-E2.1-G model (right). (a and b) total feedbacks calculated with Gregory Regression years 1-150 (black), Pendergrass 2018 kernels for CESM1-CAM5 (blue solid), and Huang 2017 kernels (blue dashed). (c and d) individual feedbacks for Pendergrass 2018 kernels. (e and f) individual feedbacks for Huang 2017 kernels.

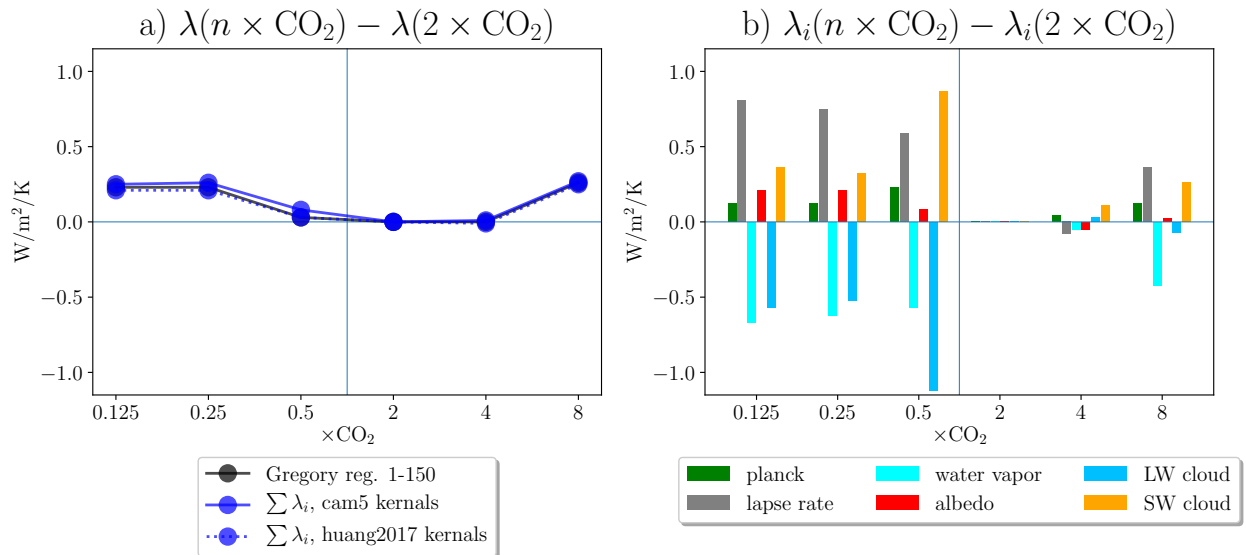


Figure A.5: Same as Figure 2.3 in main text except using the GISS-E2.1-G model.

**Appendix B: “Non-monotonic Response of the Climate System to
Abrupt CO₂ Forcing”**

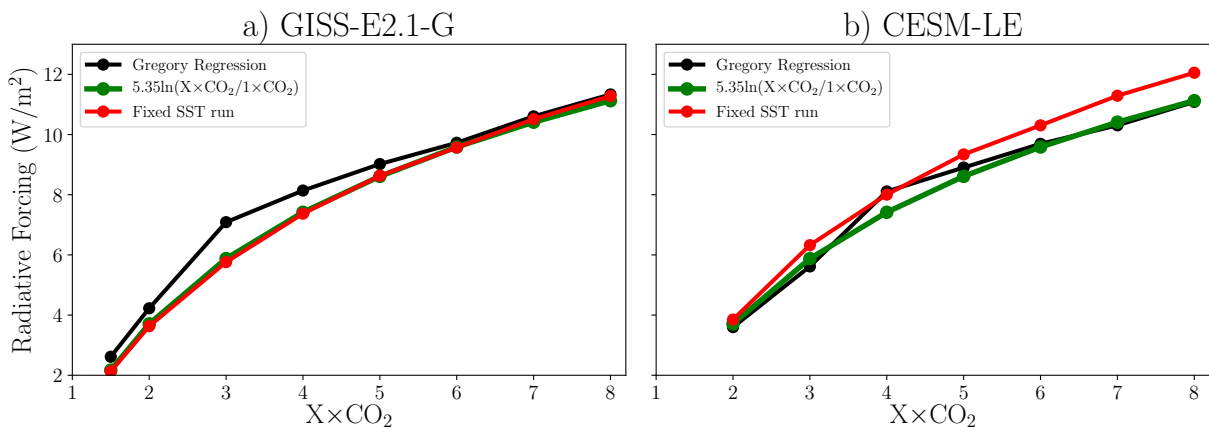


Figure B.1: Radiative forcing calculation comparison of the y-intercept from the Gregory regressions (black), the logarithmic approximation (green), and 30 year fixed SST experiments (red) for a) GISS-E2.1-G and b) CESM-LE.

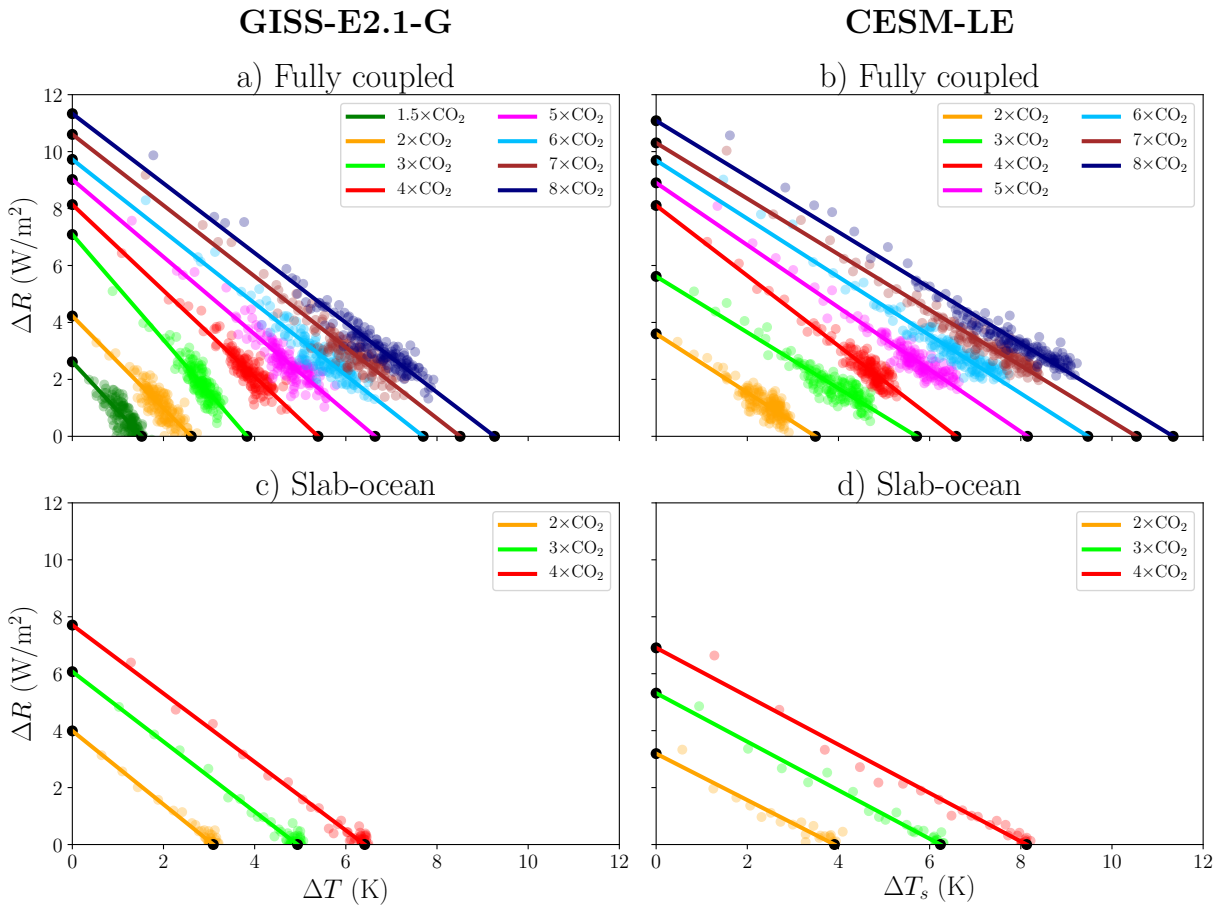


Figure B.2: Gregory regression plots for a,b) fully coupled (FOM) and c,d) slab-ocean (SOM) runs using annual averages for both GISS-E2.1-G (left) and CESM-LE (right). Intercepts are shown with larger black dots.

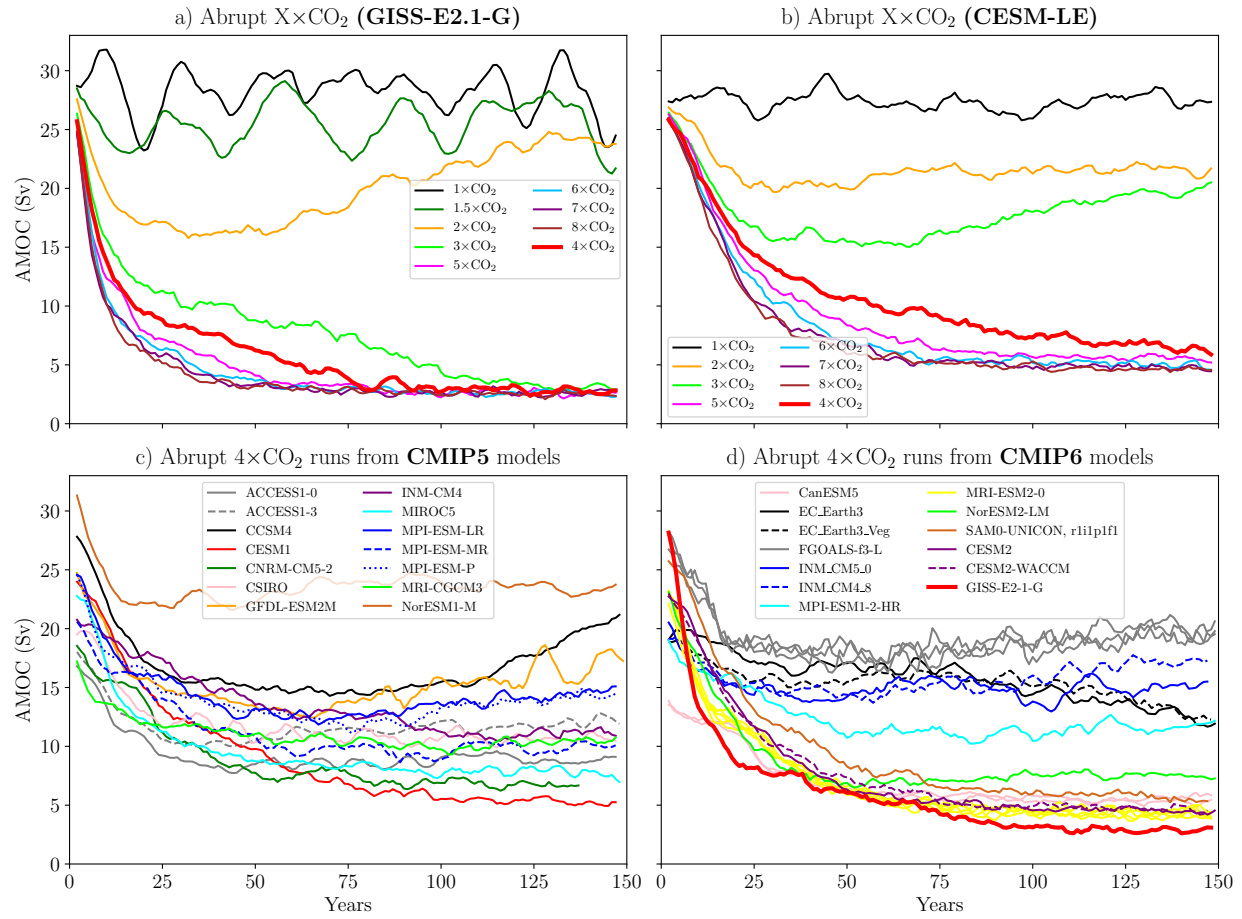


Figure B.3: Time evolution of the Atlantic Meridional Overturning Circulation (AMOC) in a,b) abrupt CO₂ forcings in fully coupled (FOM) GISS-E2.1-G and CESM-LE; c,d) abrupt 4×CO₂ runs in CMIP5 and CMIP6 models. Time series are smoothed with a 5 year running mean.

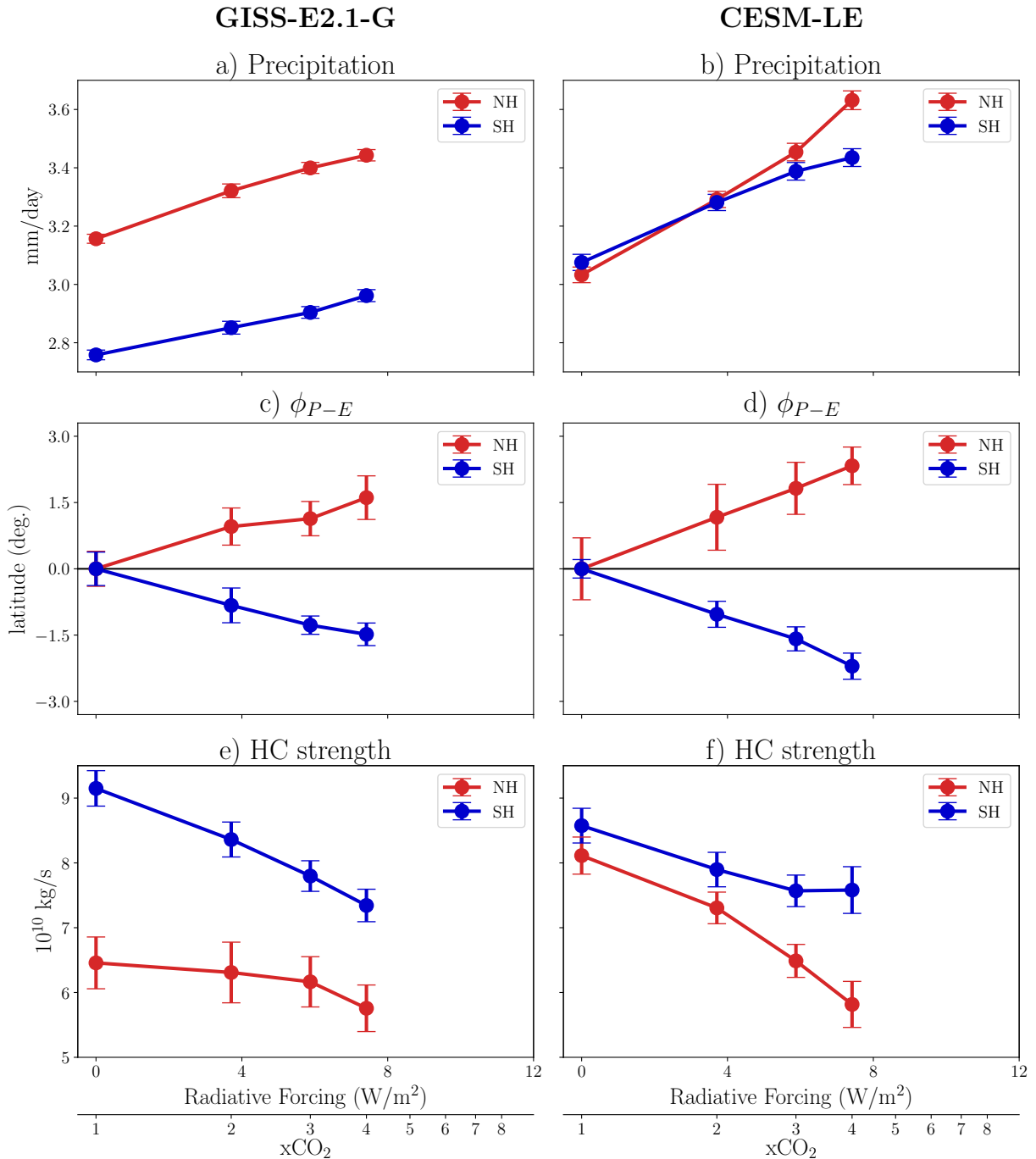


Figure B.4: As in Fig. 3.4 except shown here using output from the slab-ocean runs.

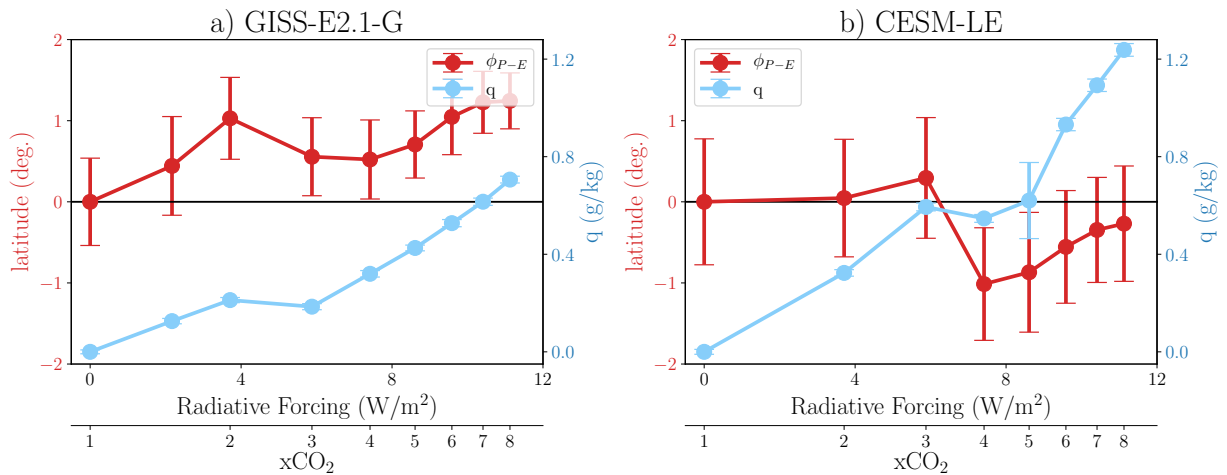


Figure B.5: NH subtropics response to abrupt CO_2 forcing. Edge of dry zones (ϕ_{P-E} , red) and specific humidity (q , light blue) for a) GISS-E2.1-G and b) CESM-LE fully coupled (FOM) models. q is averaged over 30°N to 45°N . Error bars denote 95% confidence intervals calculated using Student's t -distribution.

**Appendix C: “Non-monotonic feedback dependence under abrupt
CO₂ forcing due to a North Atlantic pattern effect”**

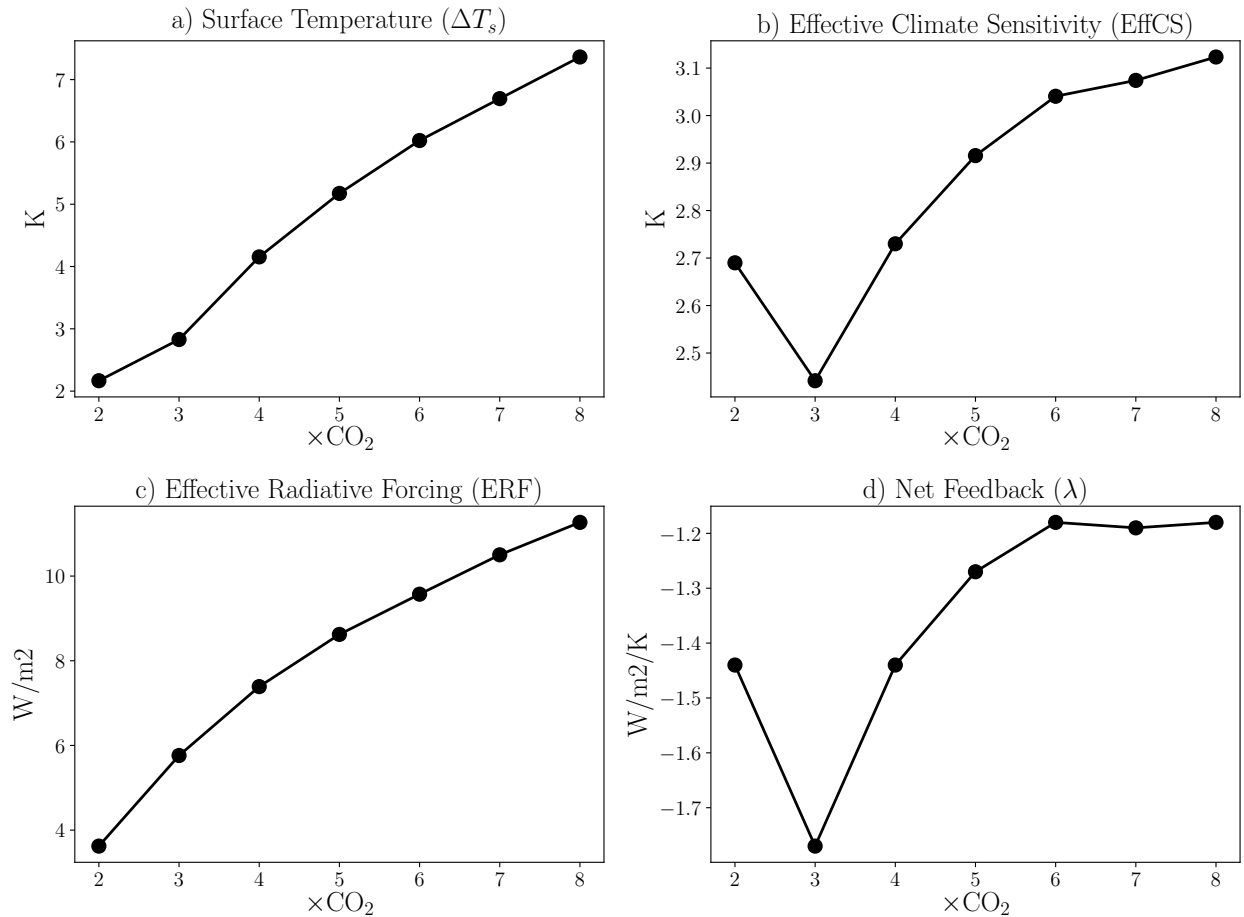


Figure C.1: Same as Figure 4.1 in main text but for the GISS-E2.1-G model.

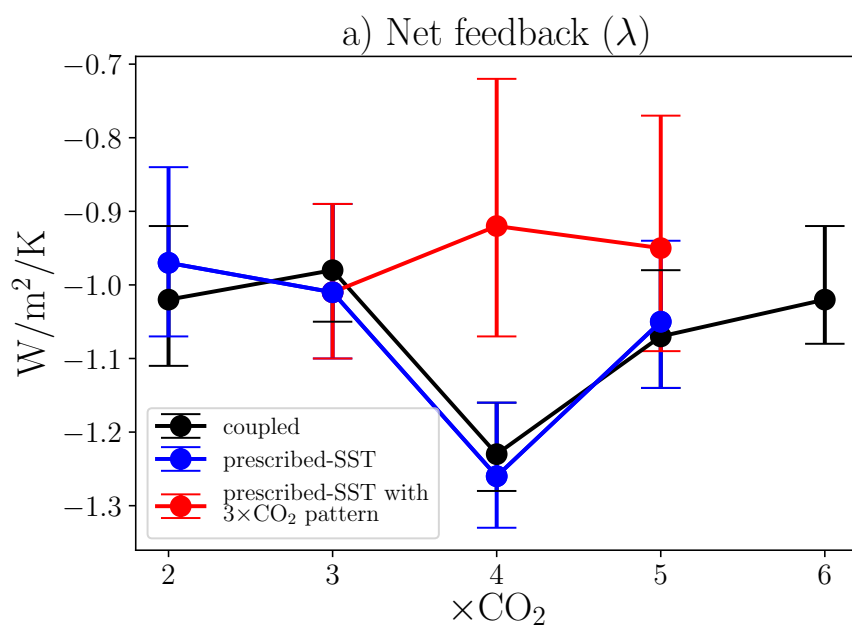


Figure C.2: Same as Figure 4.2a in main text but with 95% confidence intervals. The confidence intervals are 95% obtained by resampling the linear regressions 10,000 times.

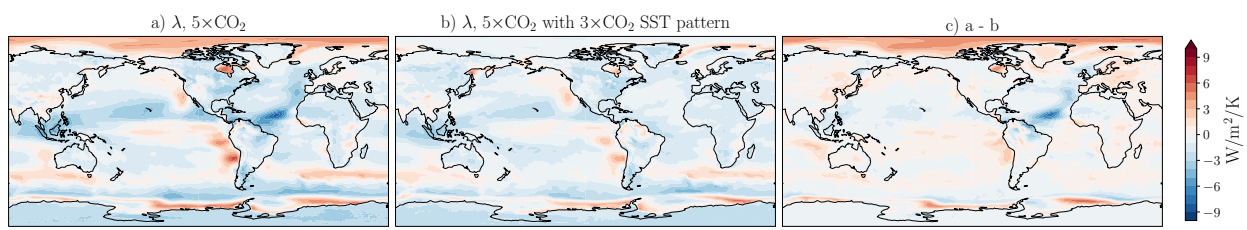


Figure C.3: Same as Figure 4.2b-d in main text but for $5\times\text{CO}_2$.

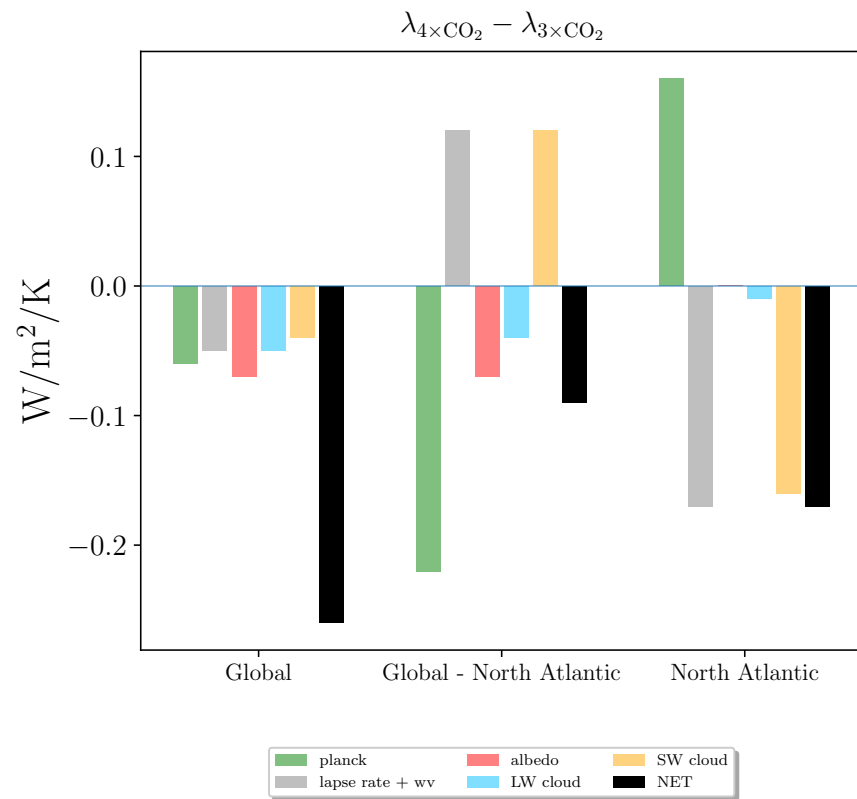


Figure C.4: Individual feedback difference between $4\times\text{CO}_2$ and $3\times\text{CO}_2$ for Global, Global - North Atlantic, and the North Atlantic region. The North Atlantic is defined as a box between 0 to 60N and 80W to 10E.

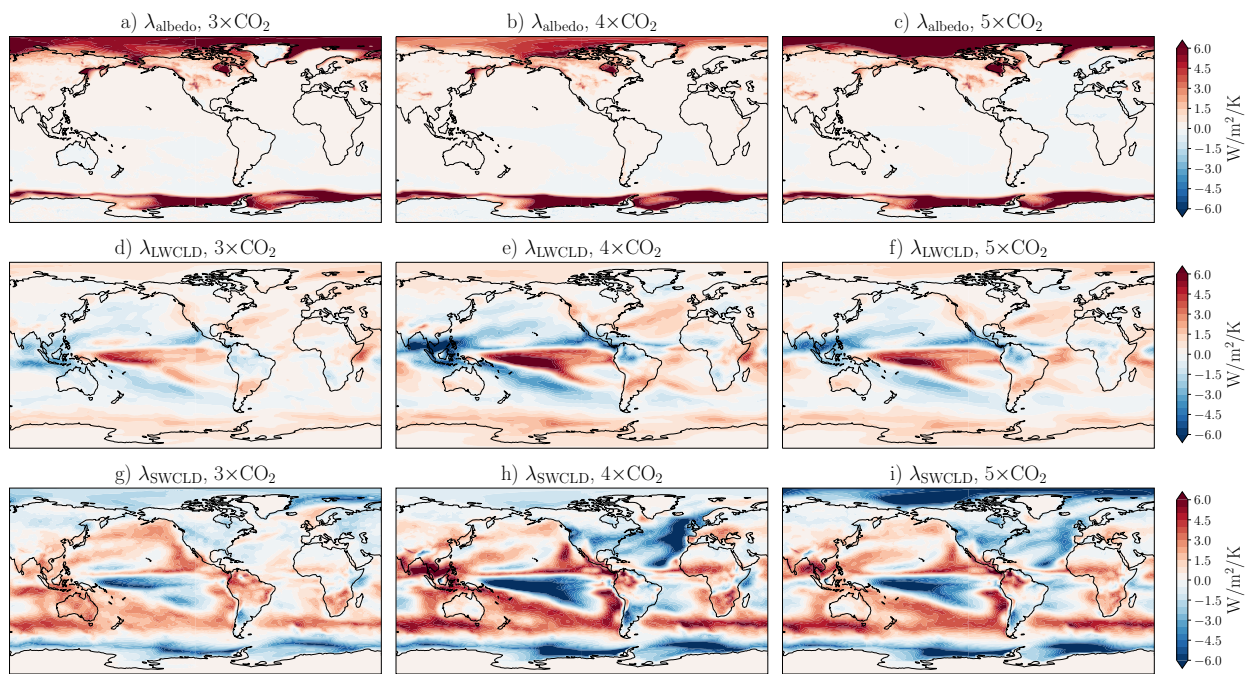


Figure C.5: Maps of individual feedbacks calculated from prescribed-SST runs for: a-c) albedo, d-f) longwave cloud, and g-i) shortwave cloud.

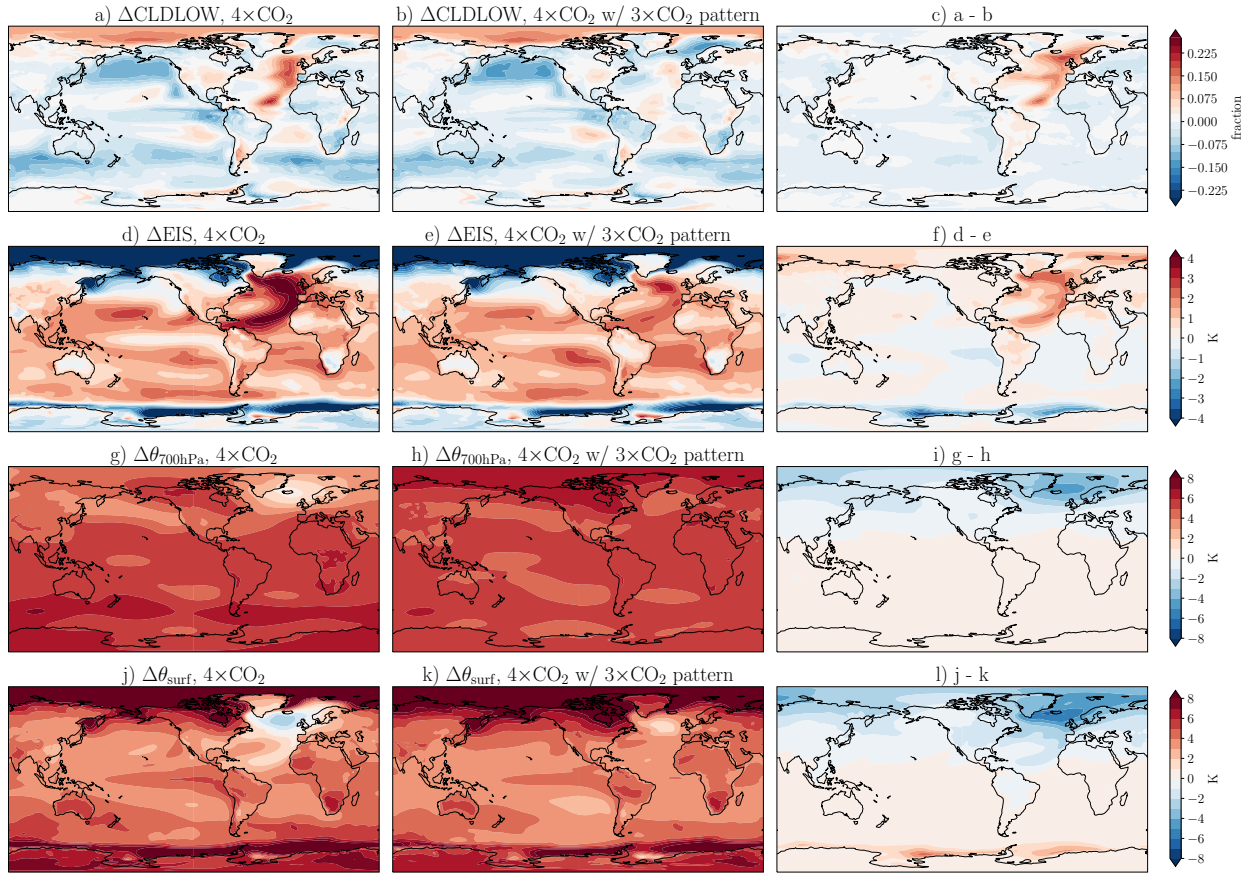


Figure C.6: Maps of a-c) low cloud content, d-f) estimated inversion strength (EIS), and potential temperature g-j) near 700 hPa and j-l) surface. The left panels (a,d,g,j) are $4 \times \text{CO}_2$ runs with prescribed-SSTs, middle panels (b,e,h,k) are $4 \times \text{CO}_2$ runs with $3 \times \text{CO}_2$ pattern, and the left panels (c,f,i,l) are the difference.

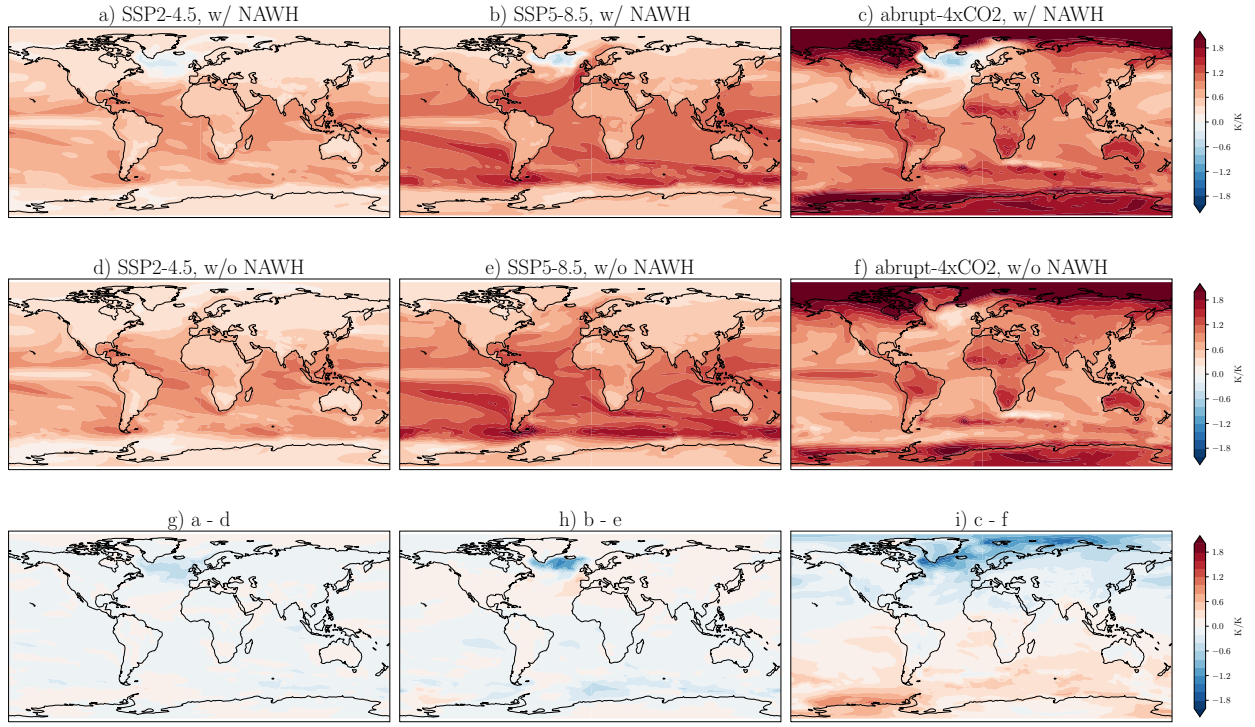


Figure C.7: Maps of surface temperature patterns from two CMIP6 models composites with (a,b,c) and without (d,e,f) North Atlantic Warming Hole (NAWH), defined as cooling in the North Atlantic, and the difference (g,h,i). Composites are shown for SSP2-4.5 (a,d,g), SSP5-8.5 (b,e,h), and abrupt-4xCO₂ scenario (c,f,i). The models without NAWH are ACCESS-CM2, AWI-CM-1-1-MR, CAMS-CSM1-0, CMCC-CM2-SR5, CanESM5, INM-CM4-8, IPSL-CM6A-LR, MIROC6, MPI-ESM1-2-HR, MPI-ESM1-2-LR. Models with NAWH are BCC-CSM2-MR, CESM2-WACCM, FGOALS-g3, GFDL-ESM4, IITM-ESM, KACE-1-0-G, MRI-ESM2-0, NorESM2-MM, TaiESM1. The surface temperature patterns are calculated as local surface temperature changes regressed to global surface temperature response for years 2015 to 2100 for the SSP scenarios and the first 150 years of the abrupt-4xCO₂ runs, and then averaged across models.

Appendix D: “Southern Hemisphere Winter Storm Tracks

Respond Differently to Low and High CO₂ Forcings”

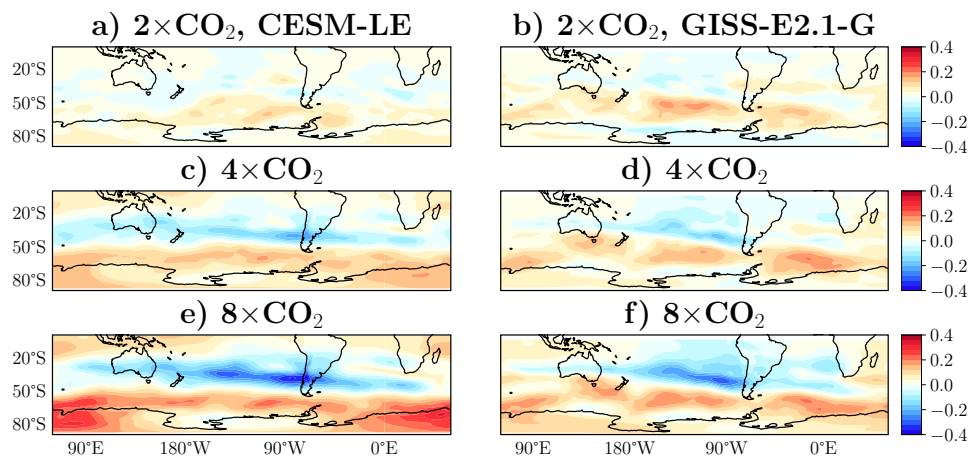


Figure D.1: Maps of wintertime EKE (10^6 Jm^{-2}) for the abrupt (a,b) $2\times\text{CO}_2$, (c,d) $4\times\text{CO}_2$, and (e,f) $8\times\text{CO}_2$ experiments. The left column presents the data from the CESM-LE model, while the right column presents the data from the GISS-E2.1-G model.

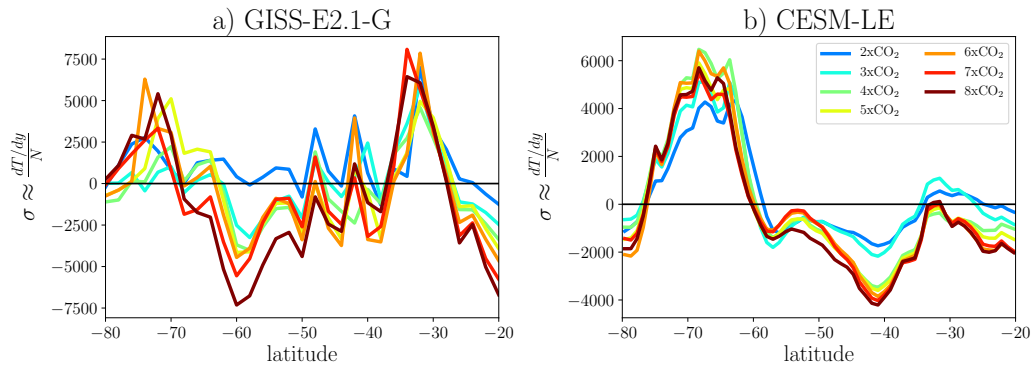


Figure D.2: Eady Growth rate ($\sigma = \frac{dT/dy}{N}$) integrated from 250hPa to the surface for the (a) CESM-LE model and (b) the GISS-E2.1-G model shown for the range of $2\times$ to $8\times\text{CO}_2$ for Southern Hemisphere winter (JJA).

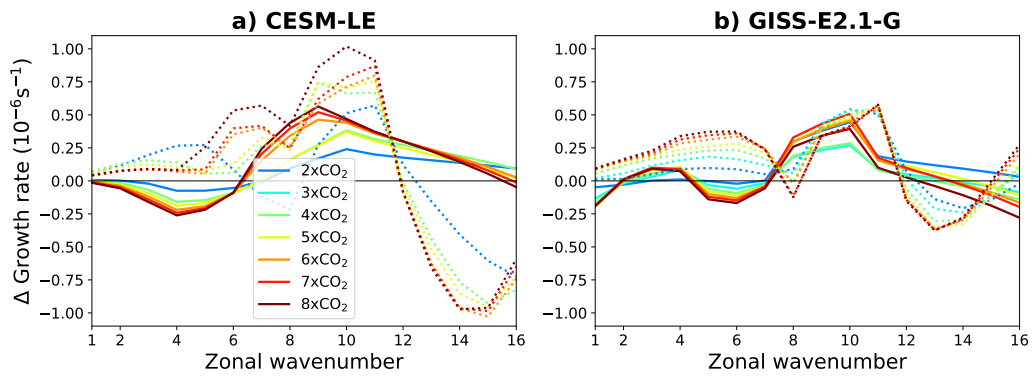


Figure D.3: The growth rate of high (solid) and low (dotted) midlatitude waves based on the linear normal-mode instability analysis in the (a) CESM-LE and the (b) GISS-E2.1-G model shown for the range of $2\times$ to $8\times\text{CO}_2$ for Southern Hemisphere winter (JJA).

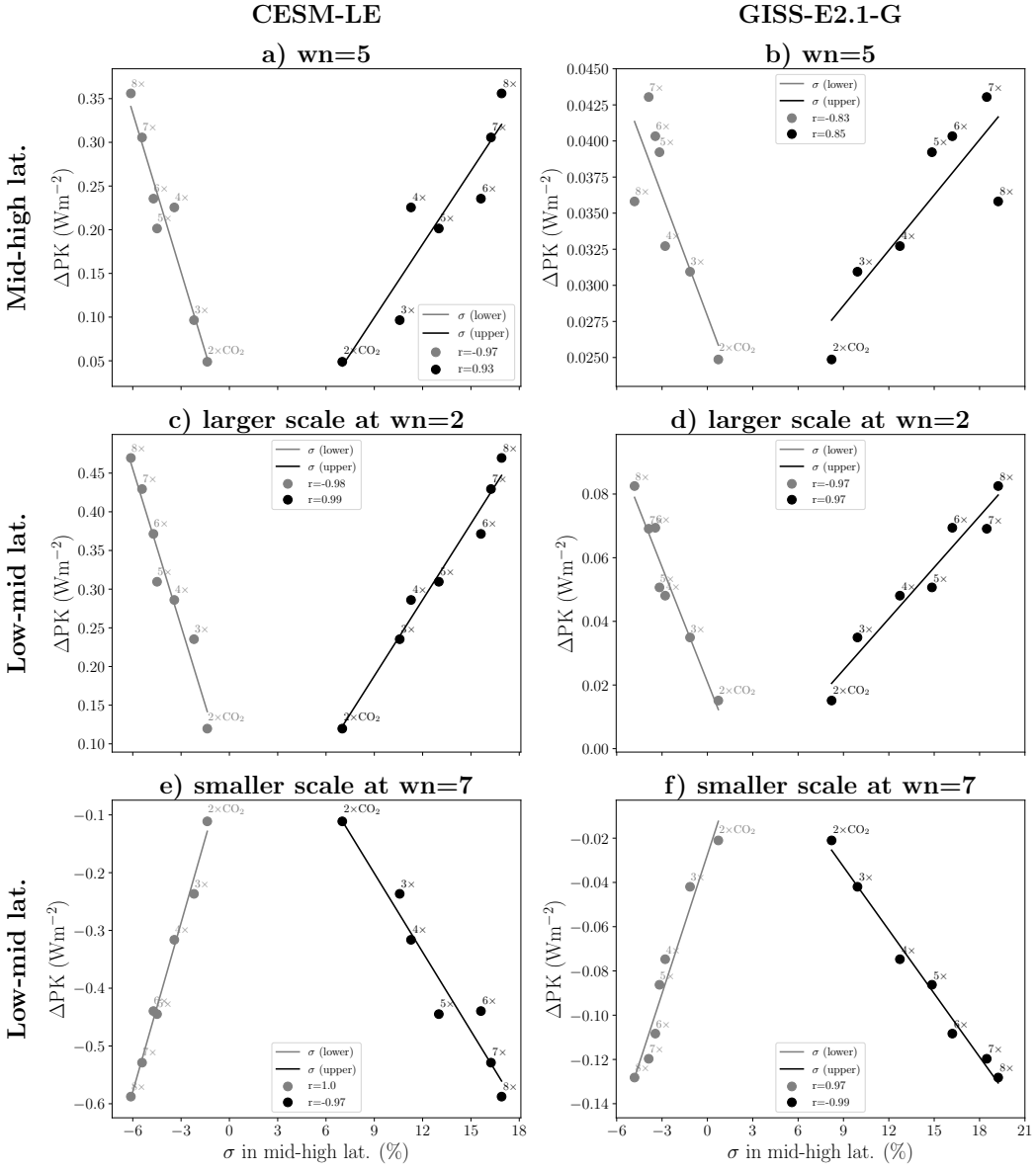


Figure D.4: Correlation between Potential to Kinetic energy conversion (PK) and upper (black) and lower (gray) tropospheric baroclinicity, as measured by the Eady Growth Rate $\sigma = \frac{dT/dy}{N}$. dT/dy are the meridional temperature gradient, and N is the static stability. Panels (a) and (b) represent high latitudes, with large scale waves (wavenumber 2) at low latitudes shown in panels (c) and (d), and small scale waves (wavenumber 7) at low latitudes in panels (e) and (f). The left column presents the data from the CESM-LE model, while the right column presents the data from the GISS-E2.1-G model. The σ values are expressed as a percentage change from the $1\times CO_2$ values, while PK is presented as a difference from the $1\times CO_2$ values. The upper tropospheric σ (black) is integrated from 250 to 500hPa, while the lower tropospheric σ from 500hPa to the surface. The correlation coefficient (r -value) is provided.

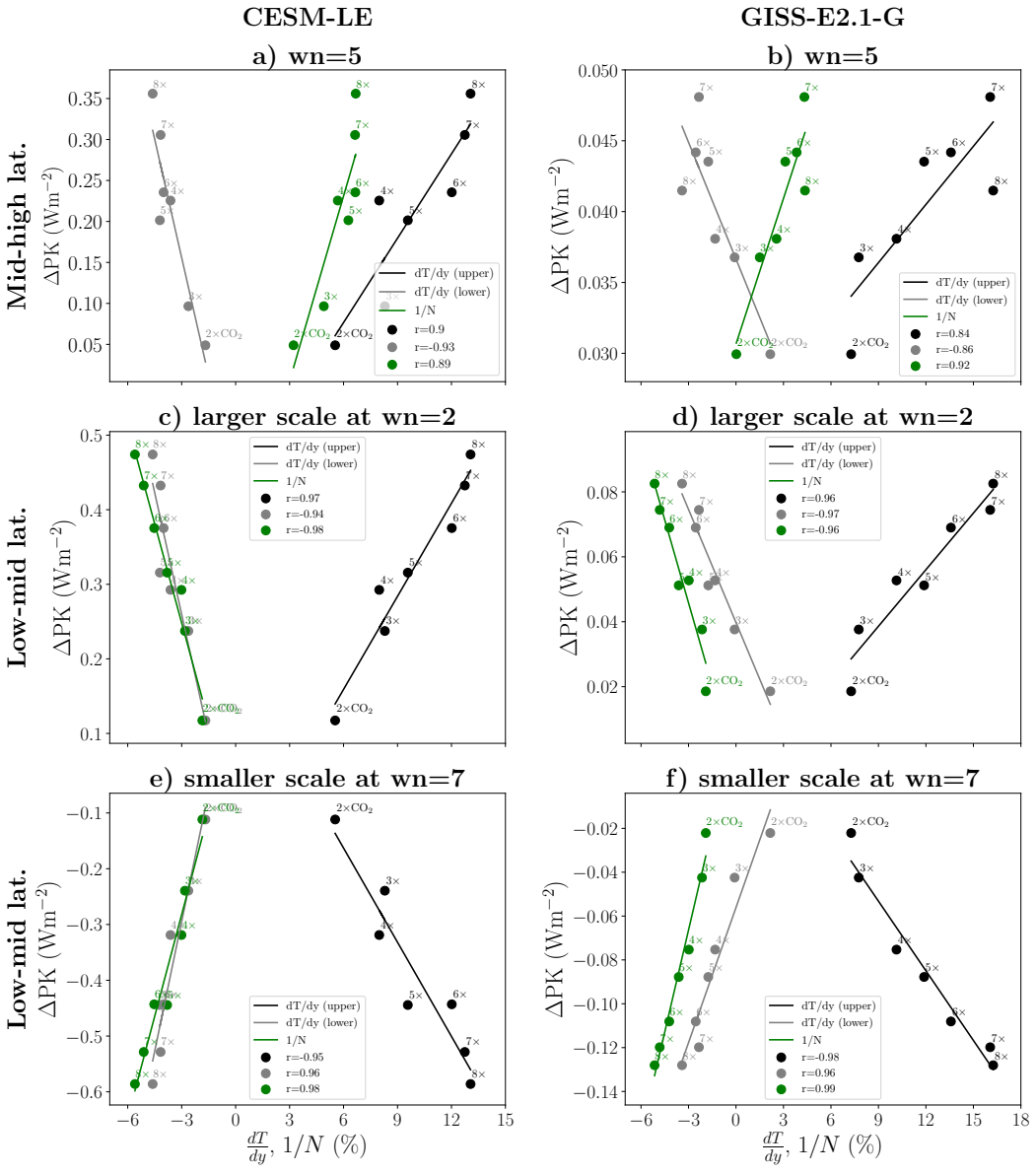


Figure D.5: Correlation between Potential to Kinetic energy conversion (PK) and upper (black) and lower (gray) meridional temperature gradient dT/dy and the inverse of static stability $1/N$. Panels (a) and (b) represent high latitudes, with large scale waves (wavenumber 2) at low latitudes shown in panels (c) and (d), and small scale waves (wavenumber 7) at low latitudes in panels (e) and (f). The left column presents the data from the CESM-LE model, while the right column presents the data from the GISS-E2.1-G model. The dT/dy and $1/N$ values are expressed as a percentage change from the $1\times CO_2$ values, while PK is presented as a difference from the $1\times CO_2$ values. The $1/N$ term is integrated from 250hPa to the surface. The correlation coefficient (r-value) is provided.

References

- Ackerley, D., Chadwick, R., Dommenget, D., & Petrelli, P. (2018). An ensemble of amip simulations with prescribed land surface temperatures. *Geoscientific Model Development*, 11(9), 3865–3881.
- Adam, O., Grise, K. M., Staten, P., Simpson, I. R., Davis, S. M., Davis, N. A., Waugh, D. W., Birner, T., & Ming, A. (2018). The tropd software package (v1): Standardized methods for calculating tropical-width diagnostics. *Geoscientific Model Development*, 11(10), 4339–4357.
- Anagnostou, E., John, E. H., Babila, T. L., Sexton, P. F., Ridgwell, A., Lunt, D. J., Pearson, P. N., Chalk, T. B., Pancost, R. D., & Foster, G. L. (2020). Proxy evidence for state-dependence of climate sensitivity in the eocene greenhouse. *Nature Communications*, 11(1), 4436.
- Anagnostou, E., John, E. H., Edgar, K. M., Foster, G. L., Ridgwell, A., Inglis, G. N., Pancost, R. D., Lunt, D. J., & Pearson, P. N. (2016). Changing atmospheric co₂ concentration was the primary driver of early cenozoic climate. *Nature*, 533(7603), 380–384.
- Andrews, T., Bodas-Salcedo, A., Gregory, J. M., Dong, Y., Armour, K. C., Paynter, D., Lin, P., Modak, A., Mauritzen, T., Cole, J. N. S., Medeiros, B., Benedict, J. J., Douville, H., Roehrig, R., Koshiro, T., Kawai, H., Ogura, T., Dufresne, J.-L., Allan, R. P., & Liu, C. (2022). On the effect of historical sst patterns on radiative feedback. *Journal of Geophysical Research: Atmospheres*, 127(18), e2022JD036675.
- Andrews, T., Gregory, J. M., Paynter, D., Silvers, L. G., Zhou, C., Mauritzen, T., Webb, M. J., Armour, K. C., Forster, P. M., & Titchner, H. (2018). Accounting for changing temperature patterns increases historical estimates of climate sensitivity. *Geophysical Research Letters*, 45(16), 8490–8499.
- Andrews, T., Gregory, J. M., & Webb, M. J. (2015). The dependence of radiative forcing and feedback on evolving patterns of surface temperature change in climate models. *Journal of Climate*, 28(4), 1630–1648.
- Andrews, T., Smith, C. J., Myhre, G., Forster, P. M., Chadwick, R., & Ackerley, D. (2021). Effective radiative forcing in a gcm with fixed surface temperatures. *Journal of Geophysical Research: Atmospheres*, 126(4), e2020JD033880.
- Andrews, T., & Webb, M. J. (2018). The Dependence of Global Cloud and Lapse Rate Feedbacks on the Spatial Structure of Tropical Pacific Warming. *Journal of Climate*, 31(2), 641–654.

- Banerjee, A., Fyfe, J. C., Polvani, L. M., Waugh, D., & Chang, K.-L. (2020). A pause in southern hemisphere circulation trends due to the montreal protocol. *Nature*, 579(7800), 544–548.
- Barnes, E. A., Barnes, N. W., & Polvani, L. M. (2014). Delayed southern hemisphere climate change induced by stratospheric ozone recovery, as projected by the cmip5 models. *Journal of Climate*, 27(2), 852–867.
- Bender, F. A., Ramanathan, V., & Tselioudis, G. (2012). Changes in extratropical storm track cloudiness 1983–2008: Observational support for a poleward shift. *Climate Dynamics*, 38, 2037–2053.
- Bitz, C. M., Shell, K. M., Gent, P. R., Bailey, D. A., Danabasoglu, G., Armour, K. C., Holland, M. M., & Kiehl, J. T. (2012). Climate sensitivity of the community climate system model, version 4. *Journal of Climate*, 25(9), 3053–3070.
- Bloch-Johnson, J., Rugenstein, M., Stolpe, M. B., Rohrschneider, T., Zheng, Y., & Gregory, J. M. (2021a). Climate sensitivity increases under higher CO₂ levels due to feedback temperature dependence [e2020GL089074 2020GL089074]. *Geophysical Research Letters*, 48(4), e2020GL089074.
- Bloch-Johnson, J., Rugenstein, M., Stolpe, M. B., Rohrschneider, T., Zheng, Y., & Gregory, J. M. (2021b). Climate sensitivity increases under higher co₂ levels due to feedback temperature dependence. *Geophysical Research Letters*, 48(4), e2020GL089074.
- Bloch-Johnson, J., Rugenstein, M. A., Alessi, M. J., Proistosescu, C., Zhao, M., Zhang, B., Williams, A. I., Gregory, J. M., Cole, J., Dong, Y., et al. (2023). The green's function model intercomparison project (GFMIP) protocol. *Authorea Preprints*.
- Block, K., & Mauritsen, T. (2013). Forcing and feedback in the mpi-esm-lr coupled model under abruptly quadrupled co₂. *Journal of Advances in Modeling Earth Systems*, 5(4), 676–691.
- Bonan, D. B., Thompson, A. F., Newsom, E. R., Sun, S., & Rugenstein, M. (2022). Transient and equilibrium responses of the atlantic overturning circulation to warming in coupled climate models: The role of temperature and salinity. *Journal of Climate*, 35(15), 5173–5193.
- Byrne, B., & Goldblatt, C. (2014). Radiative forcing at high concentrations of well-mixed greenhouse gases. *Geophysical Research Letters*, 41(1), 152–160.
- Caballero, R., & Huber, M. (2013). State-dependent climate sensitivity in past warm climates and its implications for future climate projections. *Proceedings of the National Academy of Sciences*, 110(35), 14162–14167.

- Caesar, L., Rahmstorf, S., & Feulner, G. (2020). On the relationship between Atlantic meridional overturning circulation slowdown and global surface warming. *Environmental Research Letters*, 15(2), 024003.
- Caesar, L., Rahmstorf, S., Robinson, A., Feulner, G., & Saba, V. (2018). Observed fingerprint of a weakening atlantic ocean overturning circulation. *Nature*, 556(7700), 191–196.
- Chalmers, J., Kay, J. E., Middlemas, E. A., Maroon, E. A., & DiNezio, P. (2022). Does disabling cloud radiative feedbacks change spatial patterns of surface greenhouse warming and cooling? *Journal of Climate*, 35(6), 1787–1807.
- Chang, E. K. M., Guo, Y., & Xia, X. (2012). Cmip5 multimodel ensemble projection of storm track change under global warming. *Journal of Geophysical Research: Atmospheres*, 117(D23).
- Chang, E. K.-M., Yau, A. M.-W., & Zhang, R. (2022). Finding storm track activity metrics that are highly correlated with weather impacts. part ii: Estimating precipitation change associated with projected storm track change over europe. *Journal of Climate*, 35(8), 2423–2440.
- Chang, E. K., Ma, C.-G., Zheng, C., & Yau, A. M. (2016). Observed and projected decrease in northern hemisphere extratropical cyclone activity in summer and its impacts on maximum temperature. *Geophysical Research Letters*, 43(5), 2200–2208.
- Charney, J. G. (1947). The dynamics of long waves in a baroclinic westerly current. *Journal of the Atmospheric Sciences*, 4(5), 136–162.
- Charney, J. G., Arakawa, A., Baker, D. J., Bolin, B., Dickinson, R. E., Goody, R. M., Leith, C. E., Stommel, H. M., & Wunsch, C. I. (1979). *Carbon dioxide and climate: A scientific assessment*. National Academy of Sciences, Washington, DC.
- Chemke, R. (2017). Atmospheric energy transfer response to global warming. *Quarterly Journal of the Royal Meteorological Society*, 143(706), 2296–2308.
- Chemke, R., & Ming, Y. (2020). Large atmospheric waves will get stronger, while small waves will get weaker by the end of the 21st century [e2020GL090441 10.1029/2020GL090441]. *Geophysical Research Letters*, 47(22), e2020GL090441.
- Chemke, R., & Kaspi, Y. (2015). The latitudinal dependence of atmospheric jet scales and macroturbulent energy cascades. *Journal of the Atmospheric Sciences*, 72(10), 3891–3907.
- Chemke, R., Ming, Y., & Yuval, J. (2022a). The intensification of winter mid-latitude storm tracks in the southern hemisphere. *Nature climate change*, 12(6), 553–557.

- Chemke, R., & Polvani, L. M. (2019). Exploiting the abrupt 4xCO₂ scenario to elucidate tropical expansion mechanisms. *Journal of Climate*, 32(3), 859–875.
- Chemke, R., Zanna, L., Orbe, C., Sentman, L. T., & Polvani, L. M. (2022b). The future intensification of the north atlantic winter storm track: The key role of dynamic ocean coupling. *Journal of Climate*.
- Chemke, R., Zanna, L., & Polvani, L. M. (2020). Identifying a human signal in the north atlantic warming hole. *Nature Communications*, 11(1), 1540.
- Chung, E.-S., & Soden, B. J. (2015). An assessment of direct radiative forcing, radiative adjustments, and radiative feedbacks in coupled ocean–atmosphere models. *Journal of Climate*, 28(10), 4152–4170.
- Colman, R., & McAvaney, B. (2009). Climate feedbacks under a very broad range of forcing. *Geophysical Research Letters*, 36(1).
- Conley, A. J., Lamarque, J.-F., Vitt, F., Collins, W., & Kiehl, J. (2013). Port, a cesm tool for the diagnosis of radiative forcing. *Geoscientific Model Development*, 6(2), 469–476.
- Coumou, D., Lehmann, J., & Beckmann, J. (2015). The weakening summer circulation in the northern hemisphere mid-latitudes. *Science*, 348(6232), 324–327.
- Dietmüller, S., Ponater, M., & Sausen, R. (2014). Interactive ozone induces a negative feedback in co2-driven climate change simulations. *Journal of Geophysical Research: Atmospheres*, 119(4), 1796–1805.
- Dong, Y., Proistescu, C., Armour, K. C., & Battisti, D. S. (2019). Attributing historical and future evolution of radiative feedbacks to regional warming patterns using a green's function approach: The preeminence of the western pacific. *Journal of Climate*, 32(17), 5471–5491.
- Eady, E. T. (1949). Long waves and cyclone waves. *Tellus*, 1(3), 33–52.
- Edwards, J., & Slingo, A. (1996). Studies with a flexible new radiation code. i: Choosing a configuration for a large-scale model. *Quarterly Journal of the Royal Meteorological Society*, 122(531), 689–719.
- Etminan, M., Myhre, G., Highwood, E. J., & Shine, K. P. (2016). Radiative forcing of carbon dioxide, methane, and nitrous oxide: A significant revision of the methane radiative forcing. *Geophysical Research Letters*, 43(24), 12, 614–12, 623.
- Farnsworth, A., Lunt, D. J., O'Brien, C. L., Foster, G. L., Inglis, G. N., Markwick, P., Pancost, R. D., & Robinson, S. A. (2019). Climate sensitivity on geological timescales

controlled by nonlinear feedbacks and ocean circulation. *Geophysical Research Letters*, 46(16), 9880–9889.

Forster, P., Storelvmo, T., Armour, K., Collins, W., Dufresne, J.-L., Frame, D., Lunt, D., Mauritsen, T., Palmer, M., Watanabe, M., Wild, M., & Zhang, H. (2021). The earth's energy budget, climate feedbacks, and climate sensitivity. In *Climate change 2021: The physical science basis. contribution of working group i to the sixth assessment report of the intergovernmental panel on climate change*. Cambridge University Press.

Forster, P. M., Richardson, T., Maycock, A. C., Smith, C. J., Samset, B. H., Myhre, G., Andrews, T., Pincus, R., & Schulz, M. (2016). Recommendations for diagnosing effective radiative forcing from climate models for cmip6. *Journal of Geophysical Research: Atmospheres*, 121(20), 12, 460–12, 475.

Friedrich, T., Timmermann, A., Tigchelaar, M., Elison Timm, O., & Ganopolski, A. (2016). Nonlinear climate sensitivity and its implications for future greenhouse warming. *Science Advances*, 2(11).

Fyfe, J. C. (2003). Extratropical southern hemisphere cyclones: Harbingers of climate change? *Journal of Climate*, 16(17), 2802–2805.

Gervais, M., Shaman, J., & Kushnir, Y. (2018). Mechanisms governing the development of the north atlantic warming hole in the CESM-LE future climate simulations. *Journal of Climate*, 31(15), 5927–5946.

Goessling, H. F., & Bathiany, S. (2016). Why co 2 cools the middle atmosphere—a consolidating model perspective. *Earth System Dynamics*, 7(3), 697–715.

Good, P., Andrews, T., Chadwick, R., Dufresne, J.-L., Gregory, J. M., Lowe, J. A., Schaller, N., & Shiogama, H. (2016). Nonlinmp contribution to cmip6: Model intercomparison project for non-linear mechanisms: Physical basis, experimental design and analysis principles (v1.0). *Geoscientific Model Development*, 9(11), 4019–4028.

Gregory, J. M., Andrews, T., & Good, P. (2015). The inconstancy of the transient climate response parameter under increasing CO₂. *Philosophical Transactions of the Royal Society A: Mathematical, Physical and Engineering Sciences*, 373(2054).

Gregory, J., Andrews, T., Ceppi, P., Mauritsen, T., & Webb, M. (2020). How accurately can the climate sensitivity to CO₂ be estimated from historical climate change? *Climate Dynamics*, 54(1), 129–157.

Gregory, J., Ingram, W. J., Palmer, M., Jones, G. S., Stott, P., Thorpe, R., Lowe, J. A., Johns, T., & Williams, K. (2004). A new method for diagnosing radiative forcing and climate sensitivity. *Geophysical research letters*, 31(3).

- Grise, K. M., Davis, S. M., Simpson, I. R., Waugh, D. W., Fu, Q., Allen, R. J., Rosenlof, K. H., Ummenhofer, C. C., Karnauskas, K. B., Maycock, A. C., Quan, X.-W., Birner, T., & Staten, P. W. (2019). Recent tropical expansion: Natural variability or forced response? *Journal of Climate*, 32(5), 1551–1571.
- Grise, K. M., & Polvani, L. M. (2016). Is climate sensitivity related to dynamical sensitivity? *Journal of Geophysical Research: Atmospheres*, 121(10), 5159–5176.
- Grise, K. M., Son, S.-W., Correa, G. J., & Polvani, L. M. (2014). The response of extratropical cyclones in the southern hemisphere to stratospheric ozone depletion in the 20th century. *Atmospheric Science Letters*, 15(1), 29–36.
- Hansen, J., Sato, M., Ruedy, R., Nazarenko, L., Lacis, A., Schmidt, G. A., Russell, G., Aleinov, I., Bauer, M., Bauer, S., Bell, N., Cairns, B., Canuto, V., Chandler, M., Cheng, Y., Del Genio, A., Faluvegi, G., Fleming, E., Friend, A., ... Zhang, S. (2005). Efficacy of climate forcings. *Journal of Geophysical Research: Atmospheres*, 110(D18).
- Harvey, B. J., Cook, P., Shaffrey, L. C., & Schiemann, R. (2020). The response of the northern hemisphere storm tracks and jet streams to climate change in the cmip3, cmip5, and cmip6 climate models. *Journal of Geophysical Research: Atmospheres*, 125(23), e2020JD032701.
- Harvey, B. J., Shaffrey, L. C., & Woollings, T. J. (2014). Equator-to-pole temperature differences and the extra-tropical storm track responses of the cmip5 climate models. *Climate Dynamics*, 43(5), 1171–1182.
- Haugstad, A. D., Armour, K. C., Battisti, D. S., & Rose, B. E. J. (2017). Relative roles of surface temperature and climate forcing patterns in the inconstancy of radiative feedbacks. *Geophysical Research Letters*, 44(14), 7455–7463.
- He, H., Kramer, R. J., Soden, B. J., & Jeevanjee, N. (2022). State-dependence of co2 forcing and its implications for climate sensitivity.
- Held, I. M., & O'Brien, E. (1992). Quasigeostrophic turbulence in a three-layer model: Effects of vertical structure in the mean shear. *Journal of Atmospheric Sciences*, 49(19), 1861–1870.
- Huang, Y., Xia, Y., & Tan, X. (2017). On the pattern of co2 radiative forcing and poleward energy transport. *Journal of Geophysical Research: Atmospheres*, 122(20), 10, 578–10, 593.
- IPCC. (2021). Changing state of the climate system. In S. Gulev, P. Thorne, J. Ahn, F. Dentener, C. Domingues, S. Gerland, D. Gong, D. Kaufman, H. Nnamchi, J. Quaas, J. Rivera, S. Sathyendranath, S. Smith, B. Trewin, K. von Schuckmann, & R. Vose (Eds.), *In climate change 2021: The physical science basis. contribution of work-*

ing group i to the sixth assessment report of the intergovernmental panel on climate change. Cambridge University Press.

Jeevanjee, N., Seeley, J. T., Paynter, D., & Fueglistaler, S. (2021). An analytical model for spatially varying clear-sky co₂ forcing. *Journal of Climate*, 34(23), 9463–9480.

Jonko, A. K., Shell, K. M., Sanderson, B. M., & Danabasoglu, G. (2012). Climate feedbacks in CCSM3 under changing CO₂ forcing. part i: Adapting the linear radiative kernel technique to feedback calculations for a broad range of forcings. *Journal of Climate*, 25(15), 5260–5272.

Jonko, A. K., Shell, K. M., Sanderson, B. M., & Danabasoglu, G. (2013). Climate feedbacks in CCSM3 under changing CO₂ forcing. part ii: Variation of climate feedbacks and sensitivity with forcing. *Journal of Climate*, 26(9), 2784–2795.

Kay, J. E., Deser, C., Phillips, A., Mai, A., Hannay, C., Strand, G., Arblaster, J. M., Bates, S. C., Danabasoglu, G., Edwards, J., Holland, M., Kushner, P., Lamarque, J.-F., Lawrence, D., Lindsay, K., Middleton, A., Munoz, E., Neale, R., Oleson, K., ... Vertenstein, M. (2015). The Community Earth System Model (CESM) Large Ensemble Project: A Community Resource for Studying Climate Change in the Presence of Internal Climate Variability. *Bulletin of the American Meteorological Society*, 96(8), 1333–1349.

Keil, P., Mauritzen, T., Jungclaus, J., Hedemann, C., Olonscheck, D., & Ghosh, R. (2020). Multiple drivers of the north atlantic warming hole. *Nature Climate Change*, 10(7), 667–671.

Kelley, M., Schmidt, G. A., Nazarenko, L. S., Bauer, S. E., Ruedy, R., Russell, G. L., Ackerman, A. S., Aleinov, I., Bauer, M., Bleck, R., Canuto, V., Cesana, G., Cheng, Y., Clune, T. L., Cook, B. I., Cruz, C. A., Del Genio, A. D., Elsaesser, G. S., Faluvegi, G., ... Yao, M.-S. (2020). GISS-E2.1: Configurations and climatology. *Journal of Advances in Modeling Earth Systems*, 12(8).

Knutti, R., & Hegerl, G. C. (2008). The equilibrium sensitivity of the earth's temperature to radiation changes. *Nature Geoscience*, 1(11), 735–743.

Knutti, R., Rugenstein, M. A. A., & Hegerl, G. C. (2017). Beyond equilibrium climate sensitivity. *Nature Geoscience*, 10(10), 727–736.

Latif, M., Sun, J., Visbeck, M., & Hadi Bordbar, M. (2022). Natural variability has dominated atlantic meridional overturning circulation since 1900. *Nature Climate Change*, 12(5), 455–460.

- Lehmann, J., Coumou, D., Frieler, K., Eliseev, A. V., & Levermann, A. (2014). Future changes in extratropical storm tracks and baroclinicity under climate change. *Environmental Research Letters*, 9(8), 084002.
- Levine, X. J., & Schneider, T. (2011). Response of the hadley circulation to climate change in an aquaplanet gcm coupled to a simple representation of ocean heat transport. *Journal of the Atmospheric Sciences*, 68(4), 769–783.
- Liang, Y.-C., Polvani, L. M., & Mitevski, I. (2022). Arctic amplification, and its seasonal migration, over a wide range of abrupt co2 forcing. *npj Climate and Atmospheric Science*, 5(1), 14.
- Lim, E.-P., & Simmonds, I. (2009). Effect of tropospheric temperature change on the zonal mean circulation and sh winter extratropical cyclones. *Climate Dynamics*, 33(1), 19–32.
- Lin, Y.-J., Hwang, Y.-T., Ceppi, P., & Gregory, J. M. (2019). Uncertainty in the evolution of climate feedback traced to the strength of the atlantic meridional overturning circulation. *Geophysical Research Letters*, 46(21), 12331–12339.
- Liu, W., Fedorov, A., & Sévellec, F. (2019). The mechanisms of the Atlantic Meridional Overturning Circulation slowdown induced by Arctic sea ice decline. *Journal of Climate*, 32(4), 977–996.
- Liu, W., Fedorov, A. V., Xie, S.-P., & Hu, S. (2020). Climate impacts of a weakened atlantic meridional overturning circulation in a warming climate. *Science Advances*, 6(26), eaaz4876.
- Lorenz, E. N. (1955). Available potential energy and the maintenance of the general circulation. *Tellus*, 7(2), 157–167.
- Maher, N., Milinski, S., Suarez-Gutierrez, L., Botzet, M., Dobrynin, M., Kornblueh, L., Kröger, J., Takano, Y., Ghosh, R., Hedemann, C., Li, C., Li, H., Manzini, E., Notz, D., Putrasahan, D., Boysen, L., Claussen, M., Ilyina, T., Olonscheck, D., ... Marotzke, J. (2019). The max planck institute grand ensemble: Enabling the exploration of climate system variability. *Journal of Advances in Modeling Earth Systems*, 11(7), 2050–2069.
- Manners, J. (2015). Socrates technical guide suite of community radiative transfer codes based on edwards and slingo. *Exeter, UK*.
- Marsh, D. R., Lamarque, J.-F., Conley, A. J., & Polvani, L. M. (2016). Stratospheric ozone chemistry feedbacks are not critical for the determination of climate sensitivity in cesm1 (waccm). *Geophysical Research Letters*, 43(8), 3928–3934.

- Martínez-Botí, M. A., Foster, G. L., Chalk, T. B., Rohling, E. J., Sexton, P. F., Lunt, D. J., Pancost, R. D., Badger, M. P. S., & Schmidt, D. N. (2015a). Plio-pleistocene climate sensitivity evaluated using high-resolution CO₂ records. *Nature*, 518(7537), 49–54.
- Martínez-Botí, M. A., Foster, G. L., Chalk, T. B., Rohling, E. J., Sexton, P. F., Lunt, D. J., Pancost, R. D., Badger, M. P. S., & Schmidt, D. N. (2015b). Plio-pleistocene climate sensitivity evaluated using high-resolution CO₂ records. *Nature*, 518(7537), 49–54.
- Marvel, K., Pincus, R., Schmidt, G. A., & Miller, R. L. (2018). Internal variability and dis-equilibrium confound estimates of climate sensitivity from observations. *Geophysical Research Letters*, 45(3), 1595–1601.
- Mauritsen, T., Bader, J., Becker, T., Behrens, J., Bittner, M., Brokopf, R., Brovkin, V., Claussen, M., Crueger, T., Esch, M., Fast, I., Fiedler, S., Fläschner, D., Gayler, V., Giorgetta, M., Goll, D. S., Haak, H., Hagemann, S., Hedemann, C., ... Roeckner, E. (2019). Developments in the mpi-m earth system model version 1.2 (mpi-esm1.2) and its response to increasing co₂. *Journal of Advances in Modeling Earth Systems*, 11(4), 998–1038.
- Meinshausen, M., Nicholls, Z. R. J., Lewis, J., Gidden, M. J., Vogel, E., Freund, M., Beyerle, U., Gessner, C., Nauels, A., Bauer, N., Canadell, J. G., Daniel, J. S., John, A., Krummel, P. B., Luderer, G., Meinshausen, N., Montzka, S. A., Rayner, P. J., Reimann, S., ... Wang, R. H. J. (2020). The shared socio-economic pathway (ssp) greenhouse gas concentrations and their extensions to 2500. *Geoscientific Model Development*, 13(8), 3571–3605.
- Menary, M. B., & Wood, R. A. (2018). An anatomy of the projected north atlantic warming hole in CMIP5 models. *Climate Dynamics*, 50(7), 3063–3080.
- Meraner, K., Mauritsen, T., & Voigt, A. (2013). Robust increase in equilibrium climate sensitivity under global warming. *geophysical research letters*, 40(22), 5944–5948.
- Mitevski, I., Dong, Y., Polvani, L. M., Rugenstein, M., & Orbe, C. (2023). Non-monotonic feedback dependence under abrupt co₂ forcing due to a north atlantic pattern effect. *Geophysical Research Letters*, 50(14), e2023GL103617.
- Mitevski, I., Orbe, C., Chemke, R., Nazarenko, L., & Polvani, L. M. (2021). Non-monotonic response of the climate system to abrupt co₂ forcing. *Geophysical Research Letters*, 48(6), e2020GL090861.
- Mitevski, I., Polvani, L. M., & Orbe, C. (2022). Asymmetric warming/cooling response to co₂ increase/ decrease mainly due to non-logarithmic forcing, not feedbacks. *Geophysical Research Letters*, 49, e2021GL097133.

- Mlynczak, M. G., Daniels, T. S., Kratz, D. P., Feldman, D. R., Collins, W. D., Mlawer, E. J., Alvarado, M. J., Lawler, J. E., Anderson, L. W., Fahey, D. W., Hunt, L. A., & Mast, J. C. (2016). The spectroscopic foundation of radiative forcing of climate by carbon dioxide. *Geophysical Research Letters*, 43(10), 5318–5325.
- Muthers, S., Anet, J. G., Stenke, A., Raible, C. C., Rozanov, E., Brönnimann, S., Peter, T., Arfeuille, F. X., Shapiro, A. I., Beer, J., Steinhilber, F., Brugnara, Y., & Schmutz, W. (2014). The coupled atmosphere–chemistry–ocean model socol-mpiom. *Geoscientific Model Development*, 7(5), 2157–2179.
- Noda, S., Kodera, K., Adachi, Y., Deushi, M., Kitoh, A., Mizuta, R., Murakami, S., Yoshida, K., & Yoden, S. (2018). Mitigation of global cooling by stratospheric chemistry feedbacks in a simulation of the last glacial maximum. *Journal of Geophysical Research: Atmospheres*, 123(17), 9378–9390.
- Nowack, P. J., Luke Abraham, N., Maycock, A. C., Braesicke, P., Gregory, J. M., Joshi, M. M., Osprey, A., & Pyle, J. A. (2015). A large ozone–circulation feedback and its implications for global warming assessments. *Nature climate change*, 5(1), 41–45.
- O’Gorman, P. A. (2010). Understanding the varied response of the extratropical storm tracks to climate change. *Proceedings of the National Academy of Sciences*, 107(45), 19176–19180.
- O’Gorman, P. A., & Schneider, T. (2008a). Energy of midlatitude transient eddies in idealized simulations of changed climates. *Journal of Climate*, 21(22), 5797–5806.
- O’Gorman, P. A., & Schneider, T. (2008b). The hydrological cycle over a wide range of climates simulated with an idealized GCM. *Journal of Climate*, 21(15), 3815–3832.
- Orbe, C., Rind, D., Miller, R. L., Nazarenko, L. S., Romanou, A., Jonas, J., Russell, G. L., Kelley, M., & Schmidt, G. A. (2023). Atmospheric response to a collapse of the north atlantic circulation under a mid-range future climate scenario: A regime shift in northern hemisphere dynamics. *Journal of Climate*, 1–52.
- Oudar, T., Sanchez-Gomez, E., Chauvin, F., Cattiaux, J., Terray, L., & Cassou, C. (2017). Respective roles of direct GHG radiative forcing and induced Arctic sea ice loss on the northern hemisphere atmospheric circulation. *Climate Dynamics*, 49(11), 3693–3713.
- Palter, J. B. (2015). The Role of the Gulf Stream in European Climate. *Annual Review of Marine Science*, 7(1), 113–137.
- Pavan, V. (1996). Sensitivity of a multi-layer quasi-geostrophic β -channel to the vertical structure of the equilibrium meridional temperature gradient. *Quarterly Journal of the Royal Meteorological Society*, 122(529), 55–72.

- Peixóto, J. P., & Oort, A. H. (1974). The annual distribution of atmospheric energy on a planetary scale. *Journal of Geophysical Research*, 79(15), 2149–2159.
- Pendergrass, A. G., Conley, A., & Vitt, F. M. (2018). Surface and top-of-atmosphere radiative feedback kernels for CESM-CAM5. *Earth System Science Data*, 10(1), 317–324.
- Pfahl, S., & Wernli, H. (2012). Quantifying the relevance of cyclones for precipitation extremes. *Journal of Climate*, 25(19), 6770–6780.
- Pincus, R., Buehler, S. A., Brath, M., Crevoisier, C., Jamil, O., Franklin Evans, K., Manners, J., Menzel, R. L., Mlawer, E. J., Paynter, D., et al. (2020). Benchmark calculations of radiative forcing by greenhouse gases. *Journal of Geophysical Research: Atmospheres*, 125(23), e2020JD033483.
- Previdi, M. (2010). Radiative feedbacks on global precipitation. *Environmental Research Letters*, 5(2), 025211.
- Rahmstorf, S., Box, J. E., Feulner, G., Mann, M. E., Robinson, A., Rutherford, S., & Schaffernicht, E. J. (2015). Exceptional twentieth-century slowdown in atlantic ocean overturning circulation. *Nature climate change*, 5(5), 475–480.
- Ramaswamy, V., Collins, W., Haywood, J., Lean, J., Mahowald, N., Myhre, G., Naik, V., Shine, K. P., Soden, B., Stenchikov, G., & Storelvmo, T. (2018). Radiative forcing of climate: The historical evolution of the radiative forcing concept, the forcing agents and their quantification, and applications. *Meteorological Monographs*, 59, 14.1–14.101.
- Randel, W. J., & Wu, F. (1999). Cooling of the arctic and antarctic polar stratospheres due to ozone depletion. *Journal of Climate*, 12(5), 1467–1479.
- Ren, X., & Liu, W. (2021). The role of a weakened atlantic meridional overturning circulation in modulating marine heatwaves in a warming climate [e2021GL095941 2021GL095941]. *Geophysical Research Letters*, 48(23), e2021GL095941.
- Richardson, T. B., Forster, P. M., Smith, C. J., Maycock, A. C., Wood, T., Andrews, T., Boucher, O., Faluvegi, G., Fläschner, D., Hodnebrog, Ø., Kasoar, M., Kirkevåg, A., Lamarque, J.-F., Mülmenstädt, J., Myhre, G., Olivié, D., Portmann, R. W., Samset, B. H., Shawki, D., . . . Watson-Parris, D. (2019). Efficacy of climate forcings in pdrmip models. *Journal of Geophysical Research: Atmospheres*, 124(23), 12824–12844.
- Rind, D., Schmidt, G. A., Jonas, J., Miller, R., Nazarenko, L., Kelley, M., & Romanski, J. (2018). Multicentury instability of the Atlantic meridional circulation in rapid warming simulations with GISS ModelE2. *Journal of Geophysical Research: Atmospheres*, 123(12), 6331–6355.

- Rivière, G. (2011). A dynamical interpretation of the poleward shift of the jet streams in global warming scenarios. *Journal of the Atmospheric Sciences*, 68(6), 1253–1272.
- Rugenstein, M., & Armour, K. C. (2021). Three flavors of radiative feedbacks and their implications for estimating equilibrium climate sensitivity. *Geophysical Research Letters*, 48(15), e2021GL092983.
- Rugenstein, M., Bloch-Johnson, J., Abe-Ouchi, A., Andrews, T., Beyerle, U., Cao, L., Chadha, T., Danabasoglu, G., Dufresne, J.-L., Duan, L., et al. (2019). Longrunmip: Motivation and design for a large collection of millennial-length aogcm simulations. *Bulletin of the American Meteorological Society*, 100(12), 2551–2570.
- Rugenstein, M. A., Bloch-Johnson, J., Gregory, J., Andrews, T., Mauritzen, T., Li, C., Frölicher, T. L., Paynter, D., Danabasoglu, G., Yang, S., Dufresne, J.-L., Cao, L., Schmidt, G. A., Abe-Ouchi, A., Geoffroy, O., & Knutti, R. (2020). Equilibrium climate sensitivity estimated by equilibrating climate models. *Geophysical Research Letters*, 47(4), e2019GL083898.
- Rugenstein, M. A., Caldeira, K., & Knutti, R. (2016). Dependence of global radiative feedbacks on evolving patterns of surface heat fluxes. *Geophysical Research Letters*, 43(18), 9877–9885.
- Rugenstein, M. A. A., Winton, M., Stouffer, R. J., Griffies, S. M., & Hallberg, R. (2013). Northern High-Latitude Heat Budget Decomposition and Transient Warming. *Journal of Climate*, 26(2), 609–621.
- Russell, G. L., Lacis, A. A., Rind, D. H., Colose, C., & Opstbaum, R. F. (2013). Fast atmosphere-ocean model runs with large changes in co2. *Geophysical Research Letters*, 40(21), 5787–5792.
- Saltzman, B. (1957). Equations governing the energetics of the larger scales of atmospheric turbulence in the domain of wave number. *Journal of Atmospheric Sciences*, 14(6), 513–523.
- Schmidt, G. A., Ruedy, R., Hansen, J. E., Aleinov, I., Bell, N., Bauer, M., Bauer, S., Cairns, B., Canuto, V., Cheng, Y., Del Genio, A., Faluvegi, G., Friend, A. D., Hall, T. M., Hu, Y., Kelley, M., Kiang, N. Y., Koch, D., Lacis, A. A., ... Yao, M.-S. (2006). Present-day atmospheric simulations using GISS ModelE: Comparison to in situ, satellite, and reanalysis data. *Journal of Climate*, 19(2), 153–192.
- Schwierz, C., Köllner-Heck, P., Zenklusen Mutter, E., Bresch, D. N., Vidale, P.-L., Wild, M., & Schär, C. (2010). Modelling european winter wind storm losses in current and future climate. *Climatic change*, 101, 485–514.

- Scinocca, J. F., Reader, M. C., Plummer, D. A., Sigmond, M., Kushner, P. J., Shepherd, T. G., & Ravishankara, A. R. (2009). Impact of sudden Arctic sea-ice loss on stratospheric polar ozone recovery. *Geophysical Research Letters*, 36(24).
- Seeley, J. T., & Jeevanjee, N. (2021). H₂O windows and CO₂ radiator fins: A clear-sky explanation for the peak in equilibrium climate sensitivity [e2020GL089609 2020GL089609]. *Geophysical Research Letters*, 48(4), e2020GL089609.
- Seidel, D. J., Fu, Q., Randel, W. J., & Reichler, T. J. (2008). Widening of the tropical belt in a changing climate. *Nature geoscience*, 1(1), 21.
- Sévellec, F., Fedorov, A. V., & Liu, W. (2017). Arctic sea-ice decline weakens the Atlantic Meridional Overturning Circulation. *Nature Climate Change*, 7(8), 604–610.
- Shaffer, G., Huber, M., Rondanelli, R., & Pepke Pedersen, J. O. (2016). Deep time evidence for climate sensitivity increase with warming. *Geophysical Research Letters*, 43(12), 6538–6545.
- Shell, K. M., Kiehl, J. T., & Shields, C. A. (2008). Using the radiative kernel technique to calculate climate feedbacks in ncar's community atmospheric model. *Journal of Climate*, 21(10), 2269–2282.
- Sherwood, S. C., Bony, S., Boucher, O., Bretherton, C., Forster, P. M., Gregory, J. M., & Stevens, B. (2015). Adjustments in the forcing-feedback framework for understanding climate change. *Bulletin of the American Meteorological Society*, 96(2), 217–228.
- Sherwood, S. C., Webb, M. J., Annan, J. D., Armour, K. C., Forster, P. M., Hargreaves, J. C., Hegerl, G., Klein, S. A., Marvel, K. D., Rohling, E. J., Watanabe, M., Andrews, T., Braconnot, P., Bretherton, C. S., Foster, G. L., Hausfather, Z., Heydt, A. S. v. d., Knutti, R., Mauritsen, T., ... Zelinka, M. D. (2020). An assessment of earth's climate sensitivity using multiple lines of evidence. *Reviews of Geophysics*.
- Shine, K. P., Byrom, R. E., & Checa-Garcia, R. (2022). Separating the shortwave and long-wave components of greenhouse gas radiative forcing. *Atmospheric Science Letters*, 23(10), e1116.
- Smith, C. J., Kramer, R. J., & Sima, A. (2020a). The hadgem3-ga7.1 radiative kernel: The importance of a well-resolved stratosphere. *Earth System Science Data*, 12(3), 2157–2168.
- Smith, C. J., Kramer, R. J., Myhre, G., Alterskjær, K., Collins, W., Sima, A., Boucher, O., Dufresne, J.-L., Nabat, P., Michou, M., et al. (2020b). Effective radiative forcing and adjustments in cmip6 models. *Atmospheric Chemistry and Physics*, 20(16), 9591–9618.

- Smith, C., Kramer, R., Myhre, G., Forster, P., Soden, B., Andrews, T., Boucher, O., Faluvegi, G., Fläschner, D., Hodnebrog, Ø., et al. (2018). Understanding rapid adjustments to diverse forcing agents. *Geophysical Research Letters*, 45(21), 12–023.
- Soden, B. J., & Held, I. M. (2006). An assessment of climate feedbacks in coupled ocean–atmosphere models. *Journal of Climate*, 19(14), 3354–3360.
- Soden, B. J., Held, I. M., Colman, R., Shell, K. M., Kiehl, J. T., & Shields, C. A. (2008). Quantifying climate feedbacks using radiative kernels. *Journal of Climate*, 21(14), 3504–3520.
- Stap, L. B., Köhler, P., & Lohmann, G. (2019). Including the efficacy of land ice changes in deriving climate sensitivity from paleodata. *Earth System Dynamics*, 10(2), 333–345.
- Sun, L., Alexander, M., & Deser, C. (2018). Evolution of the global coupled climate response to Arctic sea ice loss during 1990–2090 and its contribution to climate change. *Journal of Climate*, 31(19), 7823–7843.
- Tian, B. (2015). Spread of model climate sensitivity linked to double-intertropical convergence zone bias. *Geophysical Research Letters*, 42(10), 4133–4141.
- Tierney, J. E., Zhu, J., King, J., Malevich, S. B., Hakim, G. J., & Poulsen, C. J. (2020). Glacial cooling and climate sensitivity revisited. *Nature*, 584(7822), 569–573.
- Trossman, D. S., Palter, J. B., Merlis, T. M., Huang, Y., & Xia, Y. (2016). Large-scale ocean circulation-cloud interactions reduce the pace of transient climate change. *Geophysical Research Letters*, 43(8), 3935–3943.
- Vallis, G. K. (2017). *Atmospheric and oceanic fluid dynamics*. Cambridge University Press.
- Williams, A. I., Jeevanjee, N., & Bloch-Johnson, J. (2023). Circus tents, convective thresholds, and the non-linear climate response to tropical SSTs. *Geophysical Research Letters*, 50(6), e2022GL101499.
- Winton, M., Griffies, S. M., Samuels, B. L., Sarmiento, J. L., & Frölicher, T. L. (2013). Connecting Changing Ocean Circulation with Changing Climate. *Journal of Climate*, 26(7), 2268–2278.
- Yau, A. M.-W., & Chang, E. K.-M. (2020). Finding storm track activity metrics that are highly correlated with weather impacts. part i: Frameworks for evaluation and accumulated track activity. *Journal of Climate*, 33(23), 10169–10186.
- Yin, J. H. (2005). A consistent poleward shift of the storm tracks in simulations of 21st century climate. *Geophysical Research Letters*, 32(18).

- Yuval, J., & Kaspi, Y. (2020). Eddy activity response to global warming-like temperature changes. *Journal of Climate*, 33(4), 1381–1404.
- Zappa, G., Shaffrey, L. C., Hodges, K. I., Sansom, P. G., & Stephenson, D. B. (2013). A multimodel assessment of future projections of north atlantic and european extratropical cyclones in the cmip5 climate models. *Journal of Climate*, 26(16), 5846–5862.
- Zelinka, M. D., Myers, T. A., McCoy, D. T., Po-Chedley, S., Caldwell, P. M., Ceppi, P., Klein, S. A., & Taylor, K. E. (2020). Causes of higher climate sensitivity in CMIP6 models. *Geophysical Research Letters*, 47(1).
- Zhang, B., Zhao, M., & Tan, Z. (2023). Using a green's function approach to diagnose the pattern effect in GFDL AM4 and CM4. *Journal of Climate*, 36(4), 1105–1124.
- Zhou, C., Wang, M., Zelinka, M., Liu, Y., Dong, Y., & Armour, K. (2023). Explaining forcing efficacy with pattern effect and state dependence. *Geophysical Research Letters*, 50(3), e2022GL101700.
- Zhou, C., Zelinka, M. D., & Klein, S. A. (2016). Impact of decadal cloud variations on the earth's energy budget. *Nature Geoscience*, 9(12), 871–874.
- Zhou, C., Zelinka, M. D., & Klein, S. A. (2017). Analyzing the dependence of global cloud feedback on the spatial pattern of sea surface temperature change with a green's function approach. *Journal of Advances in Modeling Earth Systems*, 9(5), 2174–2189.
- Zhu, J., & Poulsen, C. J. (2021). Last glacial maximum (lgm) climate forcing and ocean dynamical feedback and their implications for estimating climate sensitivity. *Climate of the Past*, 17(1), 253–267.
- Zhu, J., Otto-Bliesner, B. L., Garcia, R., Brady, E. C., Mills, M., Kinnison, D., & Lamarque, J.-F. (2022). Small impact of stratospheric dynamics and chemistry on the surface temperature of the last glacial maximum in cesm2 (waccm6ma). *Geophysical Research Letters*, 49(20), e2022GL099875.
- Zhu, J., & Poulsen, C. J. (2020). On the increase of climate sensitivity and cloud feedback with warming in the community atmosphere models. *Geophysical Research Letters*, 47(18), e2020GL089143.
- Zhu, J., Poulsen, C. J., & Tierney, J. E. (2019). Simulation of eocene extreme warmth and high climate sensitivity through cloud feedbacks. *Science Advances*, 5(9).